

HEAVY IONS

1. INTRODUCTION[†]

Heavy-ion physics is concerned with the reactions induced by nuclear projectiles whose mass number A is greater than or equal to 4. Nuclei ranging in mass number from the α -particle to the uranium nucleus have been accelerated to energies varying from a few MeV per nucleon (MeV/ A) to many GeV/ A . As this is being written, an accelerator at CERN is producing beams of ^{16}O nuclei with an energy[†] of 200 GeV/ A ; at Brookhaven, beams of nuclei up to ^{32}S with energies of approximately 15 GeV/ A have become available. Experiments at the Bevelac at Berkeley have been performed with beams of mass number extending up to uranium and with energies extending up to 2.1 GeV/ A . The capability of lower-energy machines is shown in Fig. 1.1. Of course, to make the story complete one would need to specify, as well, the currents that are available for each ion species and energy. It is not appropriate here to describe the various stratagems employed to obtain these beams. Usually, they involve the use of several accelerators (two or three) operating in tandem. The plan in each case involves stripping the heavy-ion projectile of some or all of its atomic electrons by passing the heavy-ion beam through a stripper, generally a foil. The process increases in effectiveness with increasing beam energy. The resulting heavy ion will then have a large net charge, which permits its acceleration to very high energies using electromagnetic fields. The extraordinarily rich set of phenomena produced when a heavy ion collides with a nucleus has three fundamental

[†]Bromley (84).

[†]The energy of a 200 GeV/ A ion equals 0.32 ergs/ A !

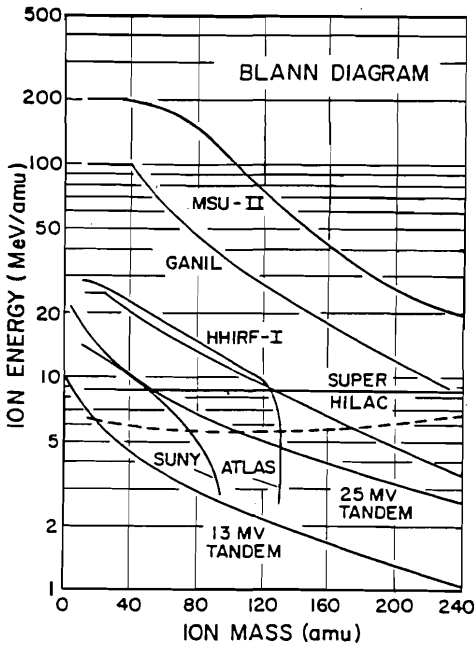


FIG. 1.1. Ion energy in MeV/nucleon as a function of the ion mass for a variety of facilities as of 1984. [From Bromley (84).]

sources: the strong electric field of the heavy ion, its large mass, and its compositeness.

The magnitude of the electric field at the surface of a nuclei is given by

$$|E| = \frac{Ze}{R^2} \approx \frac{Z}{A^{2/3}} \frac{MV}{\text{fm}} = \frac{Z}{A^{2/3}} 10^{19} \text{ V/cm} \quad (1.1)$$

a very strong field that decreases like $1/r^2$ with increasing distance R from the nuclear surface. The energy stored in the field outside of the nuclear surface is

$$E = \frac{Z^2 e^2}{R} = 1.2 \frac{Z^2}{A^{1/3}} \text{ MeV} \quad (1.2)$$

which yields an energy of 67.6 MeV for ^{27}Al and 1362 MeV for ^{208}Pb .

As a consequence of the strong, long-range electric field, it becomes possible for the incident heavy ion to excite the target nucleus electromagnetically. This phenomenon, referred to as *Coulomb excitation*, has been most important in the determination of the energy spectrum of deformed nuclei, permitting excitations to very high spin values. An example is given in Fig. 1.2, obtained by 1165-MeV ^{232}Th projectile incident upon Pb nuclei.

The strong electric field can, in fact, disintegrate the target nucleus. At the high energies available at the Bevelac, one can approximately replace the incident projectile by a beam of photons (Weizsäcker-Williams method) with the spectrum

$$N(\omega) d\omega \simeq \frac{2 Z^2 e^2}{\pi \hbar c} \left(\frac{c}{v}\right)^2 \frac{d\omega}{\omega} \quad (1.3)$$

where the photon energy is $\hbar\omega$. The photon can be absorbed by the target ejecting one or in some cases two nucleons. The cross section for the process is given by

$$\sigma = \frac{2 Z^2 e^2}{\pi \hbar c} \left(\frac{c}{v}\right)^2 \int \sigma_\gamma(\omega) \frac{d\omega}{\omega} \quad (1.4)$$

where σ_γ is the photoelectric cross section. Note that σ is proportional to Z^2 . The experimental evidence for this process is illustrated in Fig. 1.3. Here the ratio of the cross section to that of ${}^9\text{Be}$ is plotted for ${}^{18}\text{O}$ beams with 1.7 GeV/A energy incident on a variety of nuclei up to uranium. Disintegration of the ${}^{18}\text{O}$ beams is observed. The solid line gives the cross section generated by nonelectromagnetic interaction. [For this separation, see Friedlander and Heckman (85).] The deviation from the solid line increases approximately as

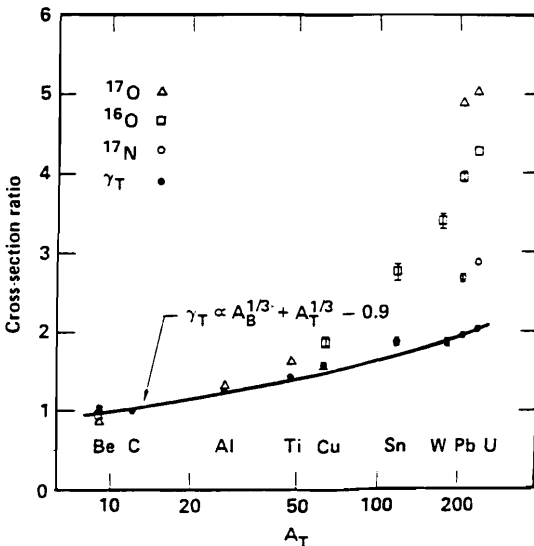


FIG. 1.3. Beam-rapidity fragment production cross-section ratios (normalized to the ${}^9\text{Be}$ cross section for ${}^{18}\text{O}$ at 1.7 GeV plotted versus mass number of the target. [From Friedlander and Heckman (84).]

Z^2 , in agreement with (1.4). There is some dependence on Z in σ_γ . Detailed calculations using an improved Weizsäcker–Williams photon spectrum yield quite good agreement with experiment.

Because of the intense electric fields, it is possible for pair production to occur in the collision of heavy ions. The observed position energy spectrum is shown in Fig. 1.4 for several pairs of heavy ions for the indicated projectile energies. The narrow peak at 300 keV has continued to escaped explanation.

Because of its large mass, the angular momentum of a heavy ion with respect to the center of mass of the target nucleus can be very large. The angular momentum in units of \hbar is classically given by

$$kR = 0.22 \sqrt{\frac{A_p A_t}{A_p + A_t} E_{\text{MeV}}} R_{\text{fm}} \quad (1.5)$$

where A_p and A_t are the projectile and target mass number, E the projectile energy in the center-of-mass system in MeV [$= (A_t/A_t + A_p)E_{\text{lab}}$], and R the sum of the target and projectile radii in fermis. If, for example, $A_p \sim {}^{48}\text{Ca}$, the target is ${}^{108}\text{Pd}$, and $E_{\text{lab}} = 205$ MeV, then $kR = 153$. Thus if these nuclei were to fuse, the resulting compound system could have a very large angular momentum. A proton at the same energy per nucleon would have a kR value of 2.6.

When a compound system of high spin is produced, the spin is, from the discussion above, approximately perpendicular to the scattering plane. Neutrons will generally be evaporated, but being isotropic, these will not carry off angular momentum. The isotopes formed in this way may also decay by γ emission. For example, in the reaction ${}^{48}\text{Ca} ({}^{108}\text{Pd}, 4n) {}^{152}\text{Dy}$, an isotope of Dysprosium is formed. Its γ -decay has been measured. Figure 1.5 shows the gamma spectrum of the highest spin band. The number marking each line is the spin of the level in ${}^{152}\text{Dy}$ emitting the γ -ray. This band is based on a prolate “superdeformation” described by Bohr and Mottelson (62). [See also the calculations of Dudek and Nazarewicz (85).] These authors showed that nucleons moving in an axially symmetric deformed oscillator well would have a *closed shell* for nucleon number 86 when the ratio of ω_x , the harmonic frequency transverse to the symmetry axis, is twice ω_z , the harmonic frequency along that axis. The corresponding deformation δ [see (VI.10.14) in deShalit and Feshbach (74)] is $\frac{1}{2}$.

Because of the large mass, the projectile has a very short wavelength. Using

$$\lambda_{\text{fm}} = \frac{1}{k} = 4.55 \sqrt{\frac{A_p + A_t}{A_p A_t} \frac{1}{E_{\text{MeV}}}} \quad (1.6)$$

the λ for ${}^{48}\text{Ca}$ is 0.067 fm with $E_{\text{lab}} = 205$ MeV. As a consequence, one can use the methods of physical optics, that is, one can use the trajectories, obtained by solving Newton’s equations of motion, as describing the path taken by the wavefront rays. By calculating the change in phase of each ray, one can construct

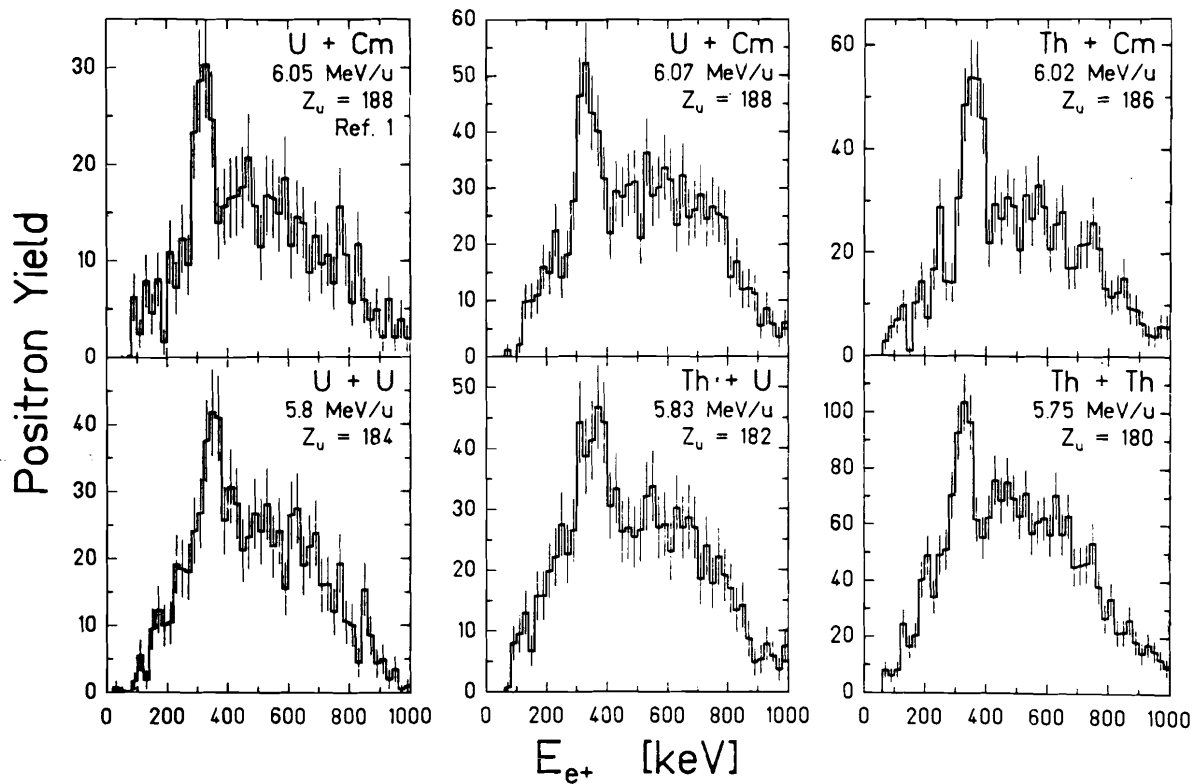


FIG. 1.4. Positron energy spectra for the five collision systems and bombarding energies indicated. [From Cowan et al. (85).]

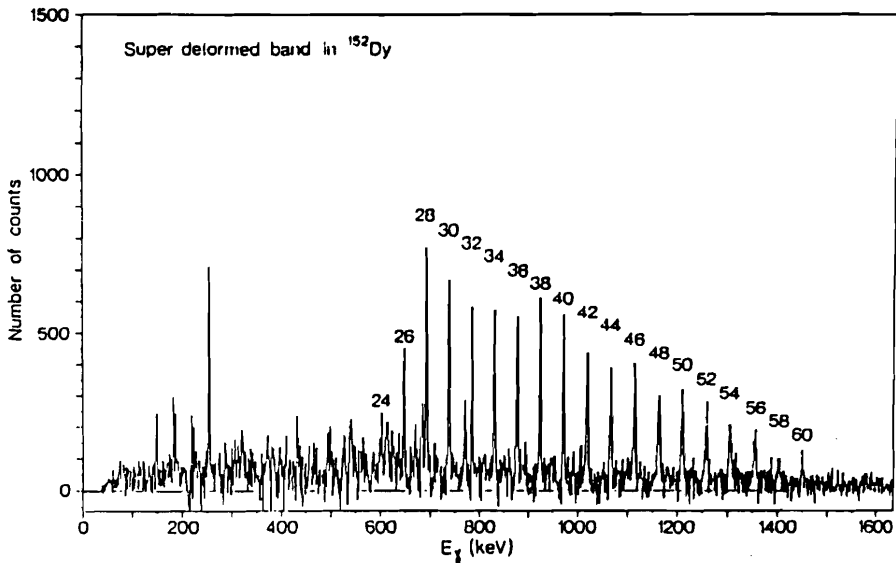


FIG. 1.5. Gamma-ray spectrum in the superdeformed band in ^{152}Dy following the $^{108}\text{Pd}(^{48}\text{Ca}, 4n)^{152}\text{Dy}$ reaction at 205 MeV. [From Twin et al. (86).]

the new equiphase wavefront, thus taking the effect of the interaction into account (see p. 103).

The Newtonian trajectory of the projectile in the Coulomb field of force exerted by the target nucleus is of obvious importance below and in the neighborhood of the Coulomb barrier energy. That trajectory is a hyperbola in the scattering plane given by

$$\frac{1}{r} = -\frac{k}{\eta} \tan^2 \frac{\vartheta}{2} \left[1 - \csc \frac{\vartheta}{2} \sin \left(\theta - \frac{\vartheta}{2} \right) \right] \quad (1.7)$$

where r is the distance from the center of charge of the target nucleus and θ measures the angle made by the vector from the scatterer to a point on the trajectory with respect to the incident direction, as illustrated in Fig. 1.6. The

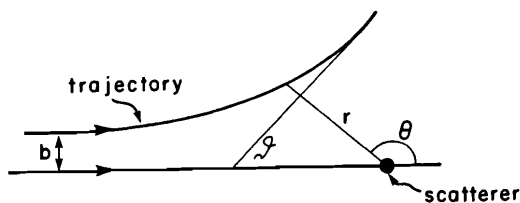


FIG. 1.6. Coulomb trajectory.

angle ϑ is the scattering angle and η is the Sommerfeld parameter:

$$\eta = \frac{Z_t Z_p e^2}{\hbar v} \quad (1.8)$$

Note that $r \rightarrow \infty$ when $\theta = \vartheta$ and also at $\theta = \pi$. The distance of closest approach, d , is obtained by placing $dr/d\theta = 0$. This yields $\theta = \pi/2 + \vartheta/2$. Therefore,

$$d = \frac{\eta}{k} \left(1 + \csc \frac{\vartheta}{2} \right) \quad (1.9)$$

while the impact parameter, b , is given by

$$b = \frac{\eta}{k} \cot \frac{\vartheta}{2} \quad (1.10)$$

Note that $\eta/k = Z_t Z_p e^2 / \hbar v k = Z_t Z_p (e^2 / \hbar c) (\hbar c / 2E)$. Numerically, $\eta/k = Z_t Z_p / 1.37E$, where E is in MeV and η/k is in fermis. The straight-line asymptote to the hyperbolic trajectory is given by

$$y \cos \vartheta = x \sin \vartheta + b \quad (1.11)$$

where x is the incident direction and y is perpendicular to x . Finally, the classical differential cross section is

$$\frac{d\sigma}{d\Omega} = \frac{b}{\sin \vartheta} \left| \frac{db}{d\vartheta} \right| \quad (1.12)$$

Using (1.10), one obtains the Rutherford cross section:

$$\frac{d\sigma}{d\Omega} = \left(\frac{\eta}{2k} \right)^2 \frac{1}{\sin^4(\vartheta/2)} = \left(\frac{Z_t Z_p}{2\mu v^2} \right)^2 \frac{1}{\sin^4(\vartheta/2)} \quad (1.13)$$

where μ is the reduced mass. The cross section drops rapidly with angle and can be quite large. For example, for 205-MeV ^{48}Ca incident on ^{208}Pb , $d\sigma/d\Omega$ equals $56 \csc^4 \frac{1}{2}\vartheta$ (fm) 2 , which at $\vartheta = 30^\circ$ becomes 0.896 barn. The grazing angle ϑ_{gr} , which will play an important role in many of the discussions in this chapter, is given according to (1.9) by

$$R = \frac{\eta}{k} (1 + \csc \frac{1}{2}\vartheta_{\text{gr}}) \quad (1.14)$$

where R is the sum of the radius of the projectile R_p and the radius of the target R_t . The trajectory corresponding to the scattering angle ϑ_{gr} just touches the surface of the target nucleus.

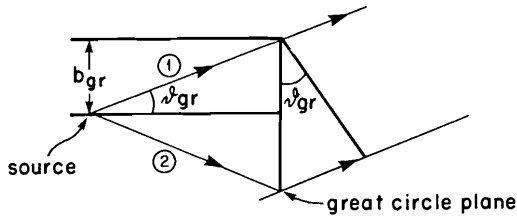


FIG. 1.7. Properties of the grazing trajectory.

As is clear from Fig. 1.6, the Coulomb field has an effect similar to that of a diverging lens [Frahn (66)]. The effective source for a point Coulomb field is a line source. However, when the nucleus is black, completely absorbing, which as we shall discuss later, is the case for most of the energy range of interest and for a wide variety of target and projectile nuclei, the grazing trajectory and the corresponding source point ($x = -b_{gr} \csc \vartheta_{gr}$) are of special importance. This is because (see discussion on p. 414) the intensity beyond the target nucleus in the forward direction can be calculated as if the perimeter of the great circle perpendicular to the incident direction acts as a source. If the path difference between the grazing trajectory labeled (1) in Fig. 1.7 and the trajectory passing through the opposite side labeled (2) equals the wavelength λ , the intensity pattern will be of the Fresnel type. If it is much less than λ the intensity pattern is of the Fraunhofer type. We obtain the conditions

$$p \gg 1 \quad \text{Fresnel}, \quad p < 1 \quad \text{Fraunhofer} \quad (1.15)$$

where

$$p = kb_{gr} \sin \vartheta_{gr} = 2\eta \cos^2 \frac{\vartheta_{gr}}{2} \quad (1.16)$$

Thus when the Sommerfeld parameter η is large, the angular distribution will be of the Fresnel type. This will be the case if the nuclei involved are reasonably heavy. [Note: Frahn's p is $\frac{1}{2}$ that given in (1.16).] The angular distribution in the geometric optics limit is illustrated in Fig. 1.8. In the physical optics limit, diffraction oscillations will be present for $\vartheta \lesssim \vartheta_{gr}$, while for larger angles, the shadow region, $\vartheta > \vartheta_{gr}$, the cross section will decrease rapidly.

An example of Fresnel scattering is shown in Fig. 1.9. The value of p for this case is 28. The angular region with the smooth and sharp decrease corresponds

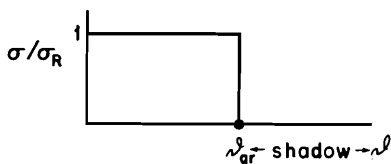


FIG. 1.8. Angular distribution in the geometric optics limit.

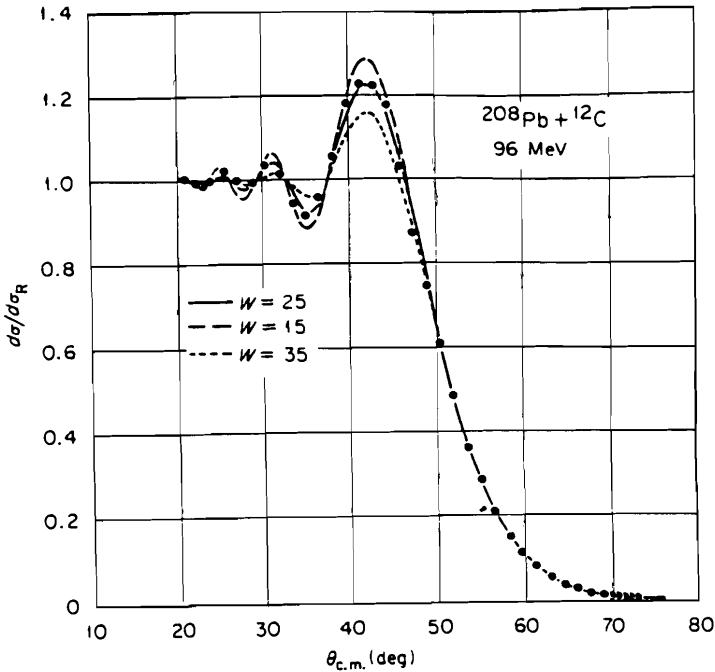


FIG. 1.9. Showing the sensitivity of the structure in the illuminated region of Fresnel scattering to the ratio of the strengths of the real (V) and imaginary (W) parts of the optical potential. In each case $V = 40$ MeV. [From Satchler (75).]

to the shadow cast by the target. Large-angle scattering corresponds to small values of the impact parameter. For these values the incident trajectory would strike the target and be absorbed. An example of Fraunhofer scattering is shown in Fig. 1.10. The value of p for this case is 3.

When the nuclear interaction is taken into account, another interference phenomena becomes important. In Fig. 1.11 we show the trajectories in the presence of a real Woods-Saxon nuclear potential acting between the heavy ions in addition to the Coulomb interaction [Glendenning (75)]. Trajectory g is the grazing trajectory. Trajectory 1 is a Coulomb trajectory, and trajectory 3 shows the effect of the nuclear interaction. The scattering angle for trajectories 1 and 3 are identical. If the interaction surface is free of absorption, one can expect fluctuations in the angular distribution. Figure 1.12, which gives the angular distribution for the reaction $^{60}\text{Ni}(^{18}\text{O}, ^{16}\text{O})^{62}\text{Ni}(\text{g.s.})$, shows very large oscillations. Because this reaction involves the transfer of two neutrons, one can be certain that the nuclear interaction is involved. Baltz, Bond, Garrett, and Kahana (75) conclude that the absorption component of the optical potential consists of two parts. One is the interior volume potential, which drops off very sharply at the nuclear surface. The second is a surface derivative of a

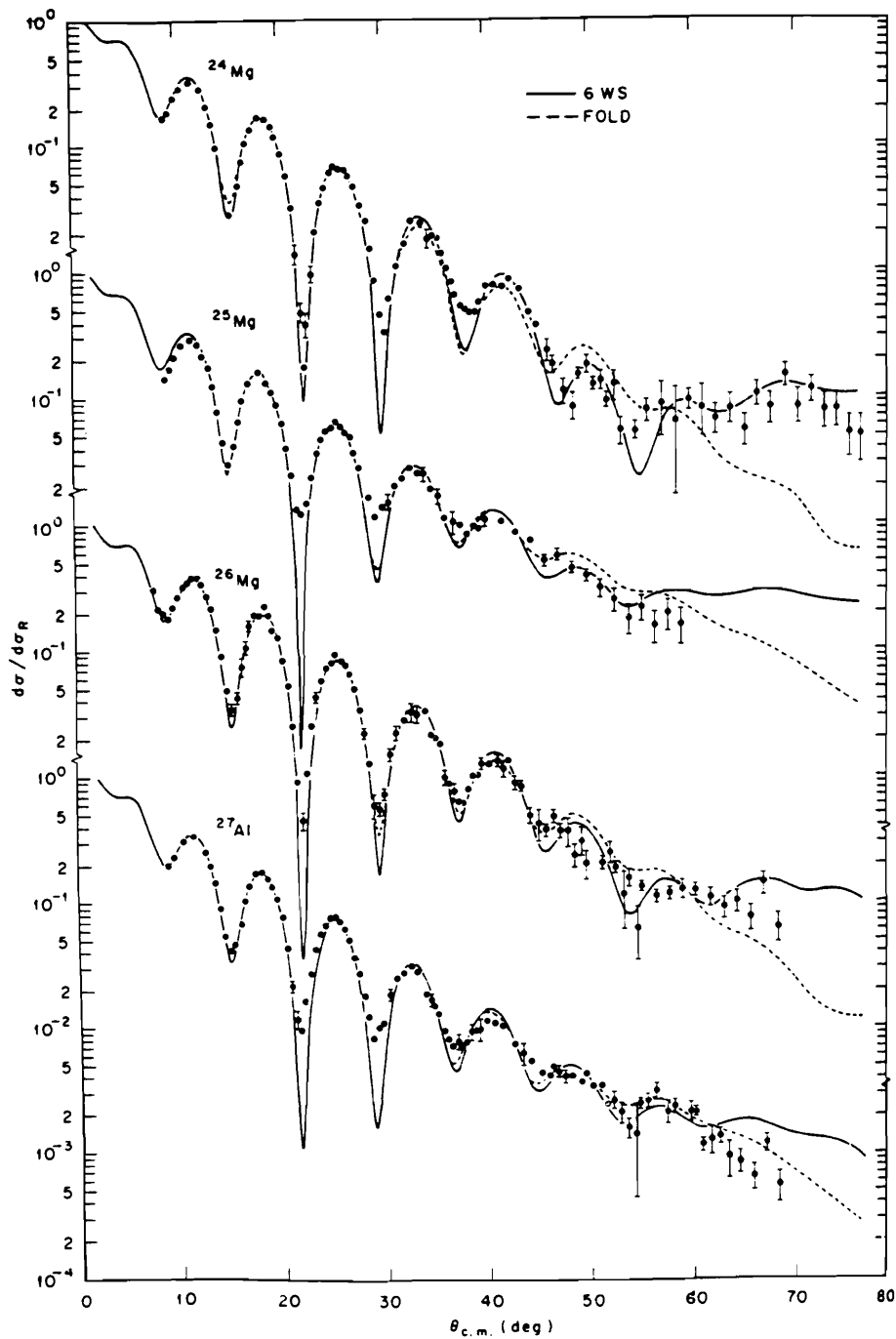


FIG. 1.10. Appearance of Fraunhofer-type patterns in the elastic scattering of ${}^6\text{Li}$ at 88 MeV. Optical-model fits using both Woods-Saxon and folded real potentials are shown. [From Fulmer, Satchler, et al. (81).]

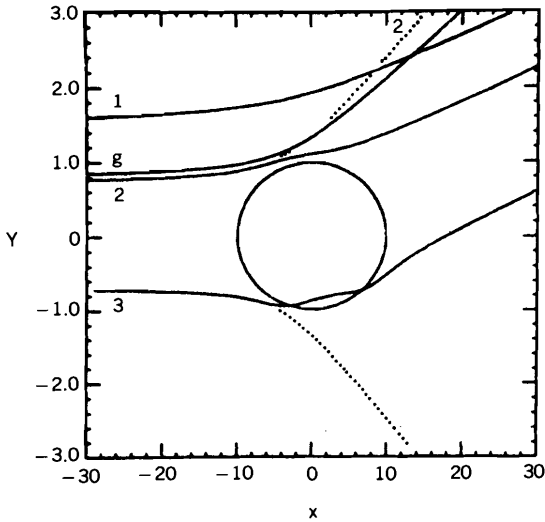


FIG. 1.11. Four classical orbits described in the text [Glendenning (75).]

Woods–Saxon potential, which is much weaker in the nuclear surface region but stronger in the nuclear interior. The stronger absorption in the nuclear interior attenuates its contribution to the reaction, which therefore originates in the surface. The interference phenomena described above occurs because of the near transparency of the surface region.

The classical deflection angle Θ plays an important role in qualitative discussions. Its relation to the potential acting between the two nuclei can be obtained from the WKB expression for the phase shift δ_λ [see Morse and Feshbach (53, p. 1102)].

$$\delta_\lambda = \int_{r_0}^{\infty} \sqrt{k^2 - U - \frac{\lambda^2}{r^2}} dr - \int_{r_1}^{\infty} \sqrt{k^2 - \frac{\lambda^2}{r^2}} dr \quad (1.17)$$

where $k^2 = 2\mu/\hbar^2 E$, $U = 2\mu/\hbar^2 V$, and $\lambda = l + \frac{1}{2}$. The turning points r_0 and r_1 are zeros of the respective integrands. Differentiating with respect to λ yields

$$\frac{\partial \delta_\lambda}{\partial \lambda} = -\lambda \int_{r_0}^{\infty} \frac{dr}{r^2 \sqrt{k^2 - U - \lambda^2/r^2}} + \lambda \int_{r_1}^{\infty} \frac{dr}{r^2 \sqrt{k^2 - \lambda^2/r^2}} \quad (1.18)$$

Since

$$k^2 - U - \frac{\lambda^2}{r^2} = \frac{\mu^2}{\hbar^2} \dot{r}^2 \quad \left(\dot{r} = \frac{dr}{dt} \right)$$

the first term in (1.18) is

$$-\frac{\lambda\hbar}{\mu} \int_{r_0}^{\infty} dr \left(\frac{1}{r^2 \dot{r}} \right)$$

But the angular momentum $\lambda\hbar$ can be related to the deflection angle Θ :

$$\lambda\hbar = \mu r^2 \dot{\Theta}$$

so the integral becomes $\int_{r_0}^{\infty} d\Theta$. A similar result is obtained for the second term in (1.18). The net result is then $\frac{1}{2}\Theta_t$, where Θ_t is the *total* deflection angle, including the incoming and outgoing trajectories. Equation (1.18) becomes (the second integral yields just $\pi/2$)

$$\frac{\partial \delta_\lambda}{\partial \lambda} = \frac{1}{2}\Theta_t = \frac{\pi}{2} - \lambda \int_{r_0}^{\infty} \frac{dr}{r^2 \sqrt{k^2 - U - \lambda^2/r^2}} \quad (1.19)$$

The scattering angles ϑ and Θ are not identical, as is illustrated by the three trajectories in Fig. 1.12, with identical values of ϑ . Bearing in mind that the sense of rotation is defined with respect to $(\mathbf{r} \times \mathbf{k})$, the value of Θ equals ϑ for case (a) equals $-\vartheta$ for case (b), and equals $(\vartheta - 2\pi)$ for case (c). Case (a) corresponds to a repulsive potential; case (b) and case (c), increasingly stronger attractive potentials acting along the trajectories.

Finally, we consider collisions in which the complex structure of the projectile and target enter in an essential fashion. The extraordinarily rich phenomena that are a consequence have been only partially explored and understood. In peripheral collisions ($d \gtrsim R$), elastic scattering, Coulomb excitation, inelastic scattering, and transfer reactions are the dominant phenomena. There are sometimes referred to as *elastic* and *quasi-elastic scattering*. As the impact parameter decreases ($d < R$), *deep inelastic scattering*, in which much of the kinetic energy of the incident projectile is converted into internal energy occurs

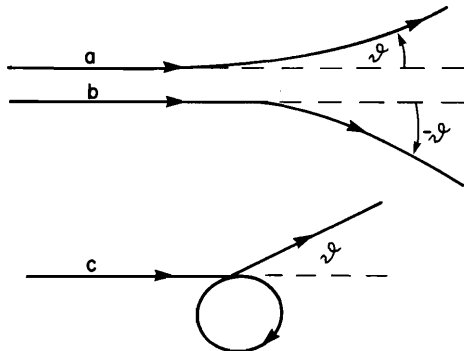


FIG. 1.12. Scattering angle ϑ for different trajectories.

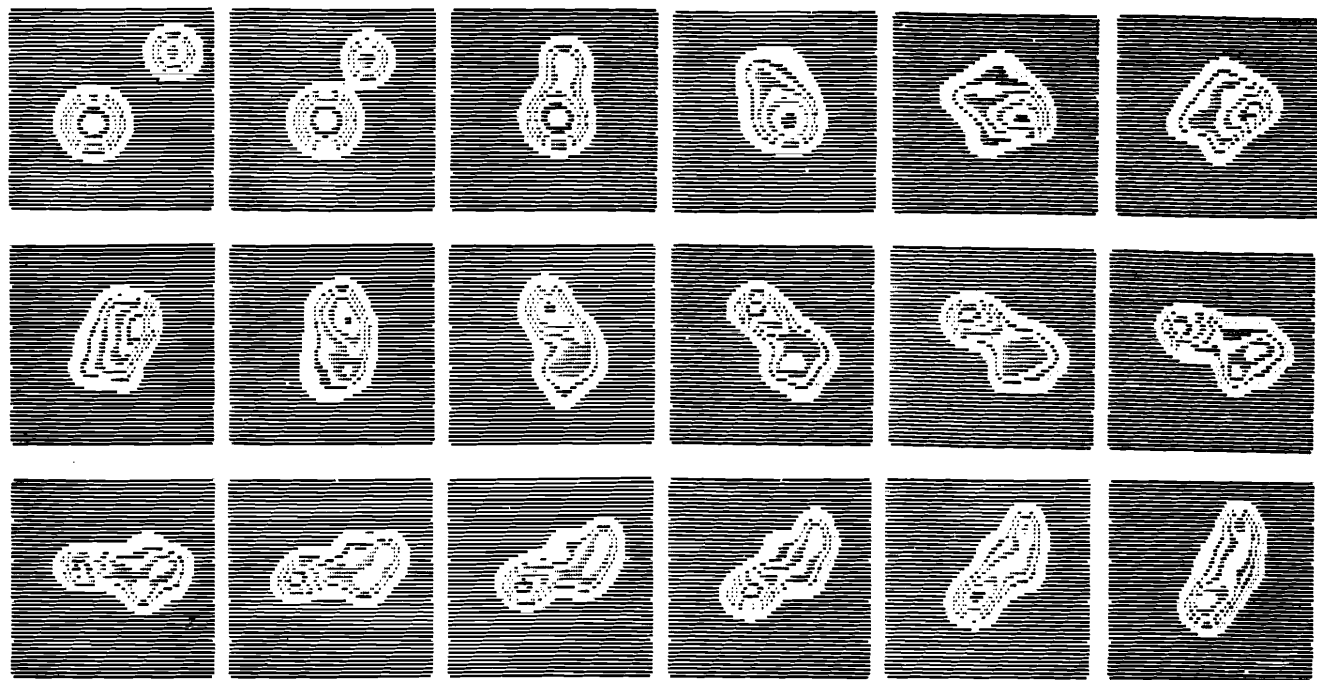


FIG. 1.13. Contour plots at sequential times of the density in the center of mass integrated over the normal to the reaction plane for $^{16}\text{O} + ^{40}\text{Ca}$ collision at the laboratory energy of 315 MeV. The initial angular momentum is $60 \hbar$. [From Negele (82).]

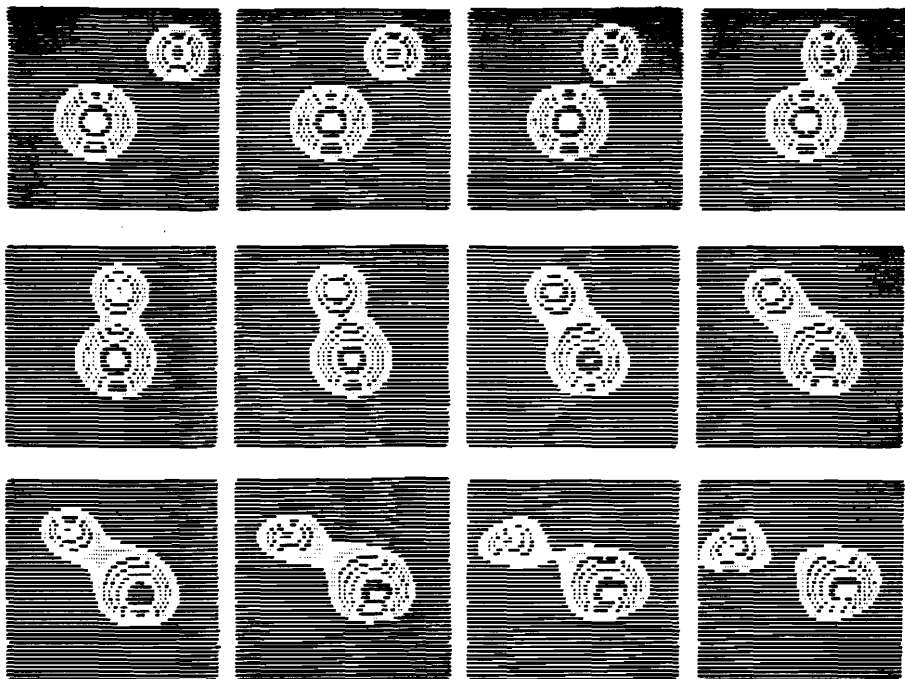


FIG. 1.14. Contour plots at sequential times of the density in the center of mass integrated over the normal to the reaction plane for $^{16}\text{O} + ^{40}\text{Ca}$ Collision at the laboratory energy of 315 MeV. The initial angular momentum is $80 \hbar$. [From Negele (82).]

so that the kinetic energy of the final nuclei derives mostly from the Coulomb repulsion. In this class of phenomena, which occurs for the most part with the heavier nuclei, the nuclei may undergo small changes in A and Z as several nucleons are interchanged while the angular distribution is strongly anisotropic. Finally, under suitable conditions the projectile can penetrate and a compound system is formed. This reaction is referred to as *fusion* reaction. If the compound system lives long enough to randomize completely, a compound nucleus in an excited state is the result. These two classes of reactions, deep inelastic and fusion, are illustrated in Figs 1.13 and 1.14, obtained by using the time-dependent Hartree–Fock method (to be discussed later). The first illustrates fusion. We see that the two nuclei join forming a very elongated nucleus, which then proceeds in three complete rotations being reduced in size as it does so. The second illustrates deep inelastic scattering. Again the elongated nucleus is formed. But after rotating through roughly 90° , it breaks apart. An intermediate situation in which complete rotations occur but the system does not fuse is referred to as *fast fission*.

These qualitative considerations are summarized in Fig. 1.15, in which the range in angular momentum l (or impact parameter b) for which the various

FIG. 1.15. Various reaction types as a function of the angular momentum, l .

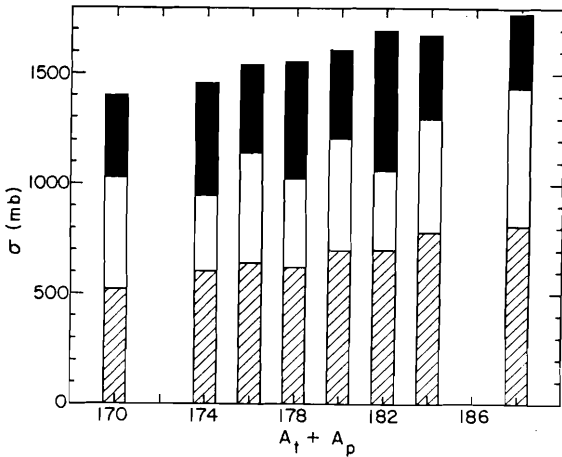
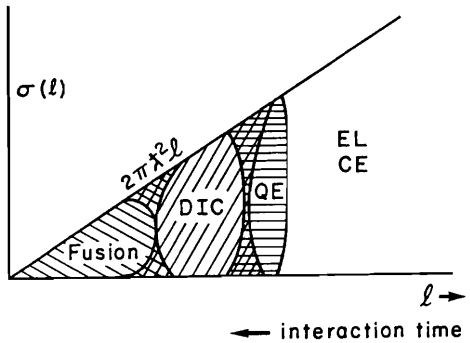


FIG. 1.16. Decomposition of the reaction cross sections as a function of the total mass number $A_t + A_p$ for the Ni-induced reactions on the even- A Sn isotopes around $E_{\text{cm}} = 220$ MeV. Shaded bars indicate values for the total fusion cross sections; fully shaded bars give the values for the total quasi-elastic transfer cross sections. [From van den Berg, Henning, et al. (88).]

processes discussed above are dominant is indicated. The crosshatched areas involve a mix of the two neighboring types. The possible value of the partial cross section $\sigma(l)$ is bounded by the geometrical cross section $2\pi r^2 l$. For the low angular momenta, compound nucleus formation and more generally fusion dominate, to be succeeded at higher angular momenta by deep inelastic scattering. This is followed by quasi-elastic scattering, that is, peripheral (one-step) reactions, and finally, for impact parameters greater than the interaction radius by elastic scattering and Coulomb excitation. Of course, these divisions are not sharp. Indeed, according to Rehm, Van denBerg, et al. (85), their experimental results indicate that the quasi-elastic processes gradually make

the transition to deep inelastic as single-particle transfers are replaced by multistep processes.

It is possible to establish a connection with the concepts employed in the discussion of the statistical multistep reactions discussed in Chapter VII (see Section 5 and Fig. 1.1). Note that the interaction time increases, as indicated, from large to small l values, the formation of the compound nucleus involving the longest interaction time. The quasi-elastic processes are identical with the single-step direct reaction, the deep inelastic has all the properties expected of the statistical multistep direct reaction, while fusion generally is an example of the statistical multistep compound reaction.

Of course, all values of l will contribute in a given reaction. In Fig. 1.16 we give an example of the relative magnitudes of each contribution for the reactions induced by $^{58,64}\text{Ni}$ incident on the various Sn isotones. The energy of the ^{58}Ni beam is 330 MeV, while the ^{64}Ni beam has energies 341 and 380 MeV. These energies correspond to center-of-mass energies roughly 30 MeV greater than the barrier energy. The proportions of each contribution will vary with the experimental situation.

2. FUSION

Let us now consider each of these regions in more detail. We begin with fusion. The discussion will be made in terms of macroscopic variables. The microscopic description is the subject of Sections 6 to 8. The macroscopic variables describe the relatively slow motions of the system. The microscopic description is concerned with the motion of the individual nucleons, which is relatively rapid. One obvious macroscopic variable is the distance R between the centers of mass of the colliding nuclei. Another variable that measures the deformation will be defined later. Models using only the R variable are referred to as one-dimensional models. The potential energy of the colliding nuclei illustrated in Fig. 2.1 is taken as a linear combination of a central Woods-Saxon potential, the Coulomb potential, and the centrifugal potential. Note the minimum or "pocket," which decreases in depth as the orbital angular momentum l (and therefore the impact parameter) increases, until finally at $l = l_b$ the minimum disappears. The depth of the pocket as well as l_b decreases as the product $Z_1 Z_2$ for the interacting nuclei increases. For an impact parameter below l_b/k and a given energy, there will be a finite probability that the system will be trapped in the minimum for a time sufficiently long for the two nuclei to fuse completely and form a compound nucleus. That probability increases with the depth and width of minimum. In detail this is accomplished through mutual excitation, particle and cluster transfer, and by interpenetration.[‡] These processes occur not only in the pocket but more generally as the nuclei approach each other, with the result that some of the kinetic energy of the system is converted into

[‡]Interpretation and transfer of large clusters are not distinguishable.

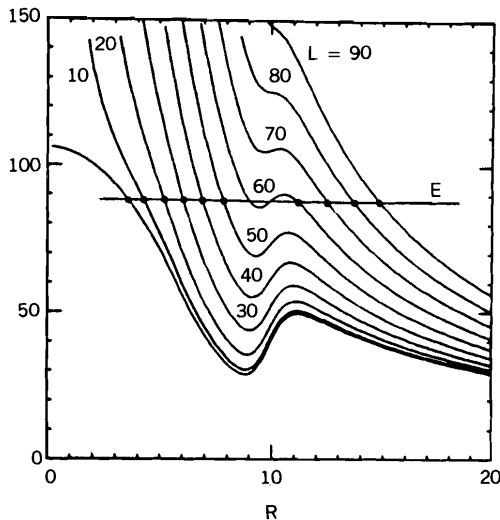


FIG. 2.1. For the system $^{18}\text{O} + ^{120}\text{Sn}$, the sum of the nuclear, Coulomb, and centrifugal potentials are shown for the indicated values of the angular momentum l . The horizontal line marks $E_{\text{cm}} = 87$ MeV. The turning points for various l 's are indicated by dots. [From Glendenning (75).]

internal energy. Thus by the time the barrier region is reached, the kinetic energy may already be reduced, facilitating the formation of the compound nucleus even when the initial orbital angular momentum exceeds l_b . The conversion of kinetic into internal energy with the consequent slowing of the nuclei can be described classically and macroscopically in terms of the action of a frictional force. Friction is invoked in classical models of the nucleus–nucleus collision.

Instead of the transfer of clusters from one nucleus to the other occurring in the potential minimum, it is clearly possible for them to be emitted before the compound nucleus is formed. The mass number of the final compound nucleus will then be less than the sum of mass numbers of the two colliding nuclei. Moreover, its momentum will be less than the momentum of the incident projectile, since some momentum is carried off by the emitted cluster, which can, for example, be an α -particle or heavier nuclear system. This process is referred to as *incomplete fusion*. This process is an example of a precompound or the multistep compound reaction discussed in Chapter VII, in which the road to complete fusion is interrupted by the emission of a cluster. It differs from the discussion in Chapter VII in that the remaining fragment can still go on to fuse.

The clusters carry off angular momentum. This is important because the compound nucleus may not be able to support the large angular momentum acquired in its formation. One such bound is provided by the Yrast line [see

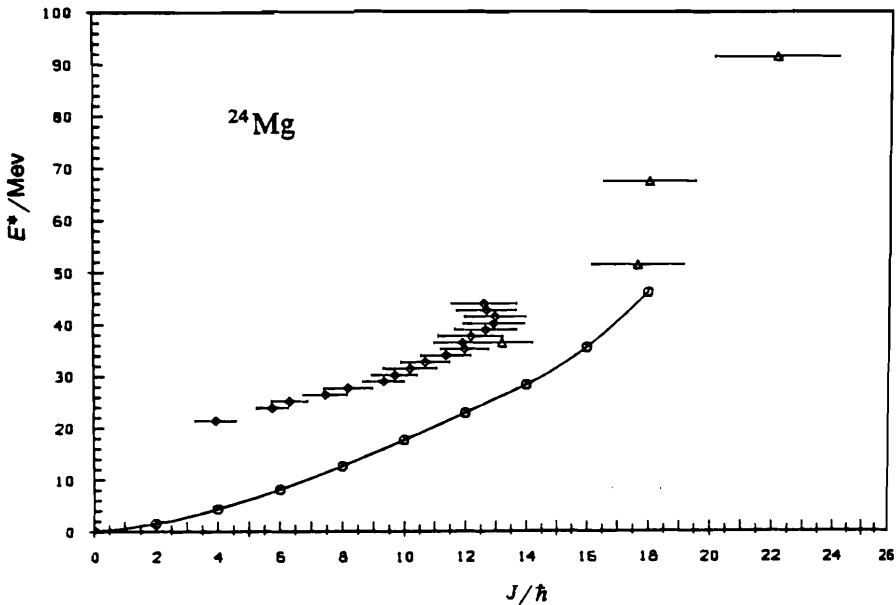


FIG. 2.2. Fusion data from $^{12}\text{C} + ^{12}\text{C} \rightarrow ^{24}\text{Mg}$ as obtained by Kovar, Gessamen, et al. (79) (diamonds) and Namboodiri, Chulick, and Natowitz (76) (triangles). The solid line and circles are a result of an Yrast line calculation for ^{24}Mg by Mülhans, Müller, Neegård, and Mosel (81) [From Mosel (84).]

Fig. 2.2 and Vandenbosch and Lazzarini (81)]. If the excitation energy and angular momentum fall to the right of the Yrast line, a compound nucleus will not be formed. If the angular momentum and energy carried by the emitted cluster or clusters are sufficient to move the original values of E and J to the left of the Yrast line, a compound nucleus can be formed. A second limitation has been discussed by Cohen, Plasil, and Swiatecki (74). The issue is the stability of a charged rotating nonviscous liquid drop. A rigid moment of inertia is assumed and the energy calculated for a variety of shapes. Their results are shown in Fig. 2.3. According to these calculations, the limiting angular momentum is about $100\hbar$ for a nucleus with $A \approx 130$. However, for both lighter and heavier nuclei, the limiting values are considerably less. Again we see that the precompound emission of clusters may be required if a compound nucleus is to be formed.

A particular example of a precompound process is referred to as *fast fission*. Of course, the compound nucleus formed by fusion may fission. Fast fission occurs *before* that compound nucleus is formed. In terms of the behavior shown in Figs 1.13 and 1.14 in fast fission, complete rotations do occur, but instead of fusing, the system breaks apart. According to Gregoire, Ngô, et al. (82), during the rotation and as a consequence of the exchange of energy, momentum and

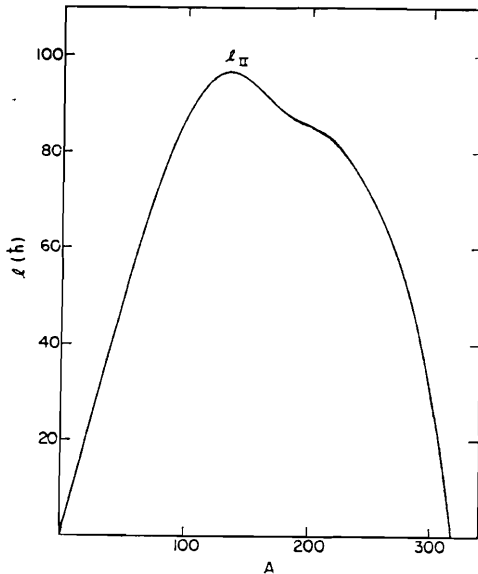


FIG. 2.3. The curve l_{II} is the angular momentum at which the fission barrier of a beta-stable nucleus with mass number A is predicted to vanish. [From Cohen, Plasil, and Swiatecki (74).]

mass, the system equilibrates and a different radial dependence of the potential $V(R)$ develops. If this potential does not have a sufficiently deep minimum, fusion will not occur; fission will. The various possible situations according to Gregoire, Ngô et al. (82) are illustrated in Fig. 2.4.

This last discussion brings the importance of time scales to our attention. The relaxation time τ_n for the motion of the nucleons to be randomized and equilibrium established is generally much smaller (except at small excitation energies) than the relaxation time for collective motion to disappear. The third time, τ_{app} , of significance is the time it takes the system to penetrate to the potential minimum. If τ_{app} is shorter than τ_n , the system will arrive in the potential minimum before equilibrium is established. The compound nucleus will then be formed as described earlier. However, if $\tau_{app} > \tau_n$, equilibrium will develop before the potential minimum is attained. As a consequence, a new interaction $V(R)$ will operate. Fast fission or deep inelastic scattering may then occur.

The simple one-dimensional interaction, $V(R)$, does not take into account the role of deformation. From the point of view of the compound nucleus, the two nuclei, at their point of contact, for example, form a highly deformed system. The passage from that situation to the deformation characteristic of the compound nucleus follows from the nature of the dependence of the potential energy upon the deformation as well as upon R . This is shown in Fig. 2.5. Nix and Sierk (77) [see also Möller and Nix (76) and Krappe, Nix, and Sierk (79)]

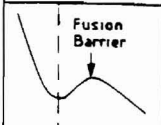
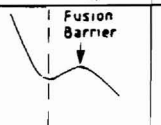
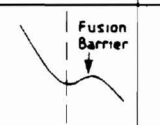
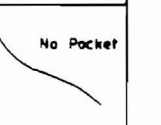
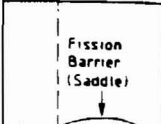
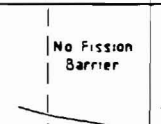
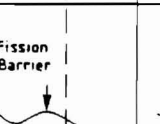
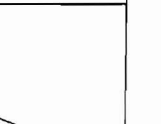
	$l < l_{Bf}$	$l > l_{Bf}$	$Z_1 Z_2 \sim 2000 - 2500$	$Z_1 Z_2 \geq 2500 - 3000$
SUDDEN POTENTIAL				
ADIABATIC POTENTIAL				
	COMPOUND NUCLEUS FORMATION	FAST FISSION	FAST FISSION	NO COMPOUND NUCLEUS FORMATION NOR FAST FISSION

FIG. 2.4. Conditions for fast fission and compound nucleus formation. The quantity l_{Bf} is the value of the angular momentum at which the fission barrier vanishes. [From Gregoire, Ngô, et al. (82).]

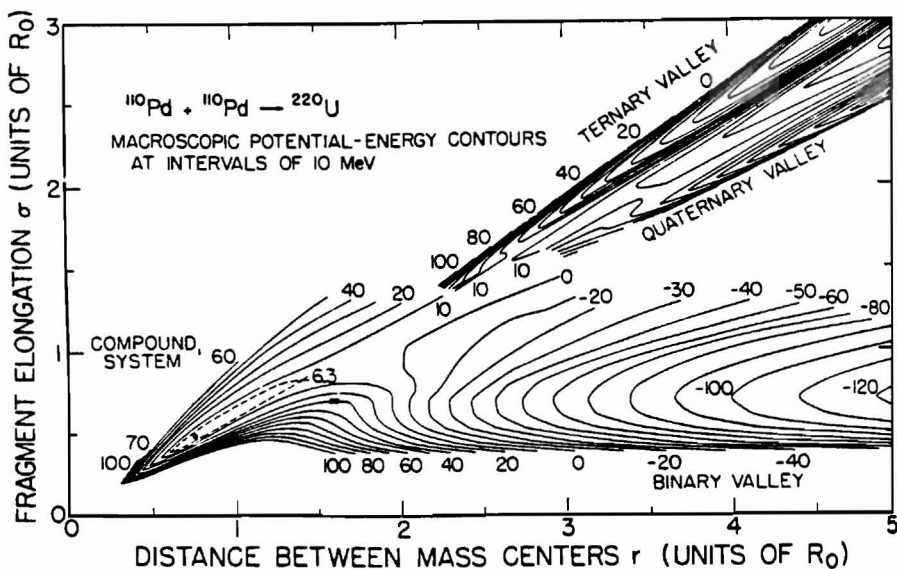


FIG. 2.5. Potential energy surface for ^{220}U as a function of two shape parameters, r and σ . Whereas r directly describe the distances between the centers of mass of the two interacting nuclei, σ is a measure for the deformation of the two. The ground state of ^{220}U is normalized to zero energy; the numbers at the contours give the energies relative to it in MeV. The contact point of two spherical touching ^{110}Pd nuclei lies at $r \approx 1.6$, $\sigma \approx 0.71$. [From Nix and Sierk (77).]

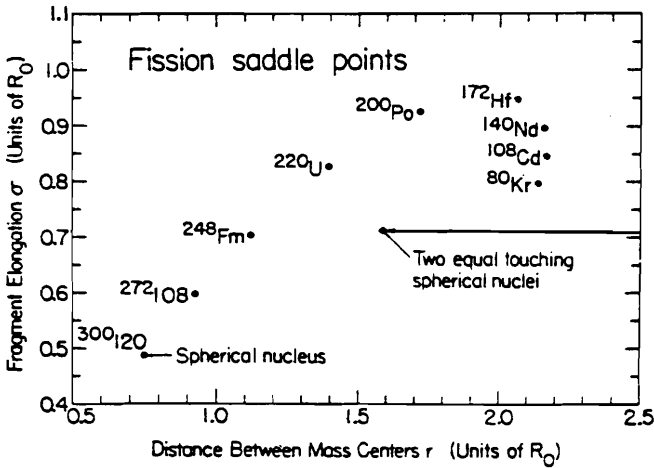


FIG. 2.6. Locations of the binary macroscopic zero angular-momentum fission saddle points in the r - σ plane for selected nuclear systems. These systems can be formed in symmetric collisions of two neutron-rich β -stable nuclei. [From Nix and Sierk (77).]

calculate the Coulomb and nuclear energy for a variety of shapes of the interacting nuclei. The diffusivity of the nuclear surface, as well as the finite range of the nuclear force (central only), is taken into account. No single-particle effects are included. Dissipation is neglected. The collision is head on, that is, $l=0$. The colliding nuclei are identical. The deformation is measured by the elongation, σ , defined as $2[\langle Z^2 \rangle - \langle Z'^2 \rangle]$, where Z is along the symmetry axis. The factor of 2 takes the elongation of both nuclei into account. Two points in Fig. 2.5 are important. One is the value of σ and R at which the two nuclei are in contact. The other is the fission saddle point. As one deforms the spherical compound nucleus, the potential energy increases arriving eventually at a maximum, the fission saddle point. If the nucleus has enough energy to pass over or penetrate the barrier, fission will occur. If the contact point occurs to the left of the fission saddle point, compound nucleus formation will occur. This is generally the case for light nuclei. If, on the other hand, it occurs to the right, it must have enough energy to pass over the barrier to form a compound nucleus, as will be required for the heavier nuclei. The extra amount of energy beyond the barrier is known as *extra push* [see also Swiatecki (82)]. The $l=0$ situation for a variety of identical colliding nuclei is shown in Fig. 2.6. Clearly, systems whose total mass number beyond about $A=220$ will have a low probability of forming a spherical compound nucleus since the fission saddle point for heavier compound nuclei lies far to the left of the contact point. The effect of angular momentum (collisions with a finite value of the impact parameter) and of the energy of the colliding systems is shown in Fig. 2.7, where again the interacting nuclei are both ^{110}Pd but the energy is now 20 MeV above the barrier energy for $l=0$. The fission saddle points for each value of l are

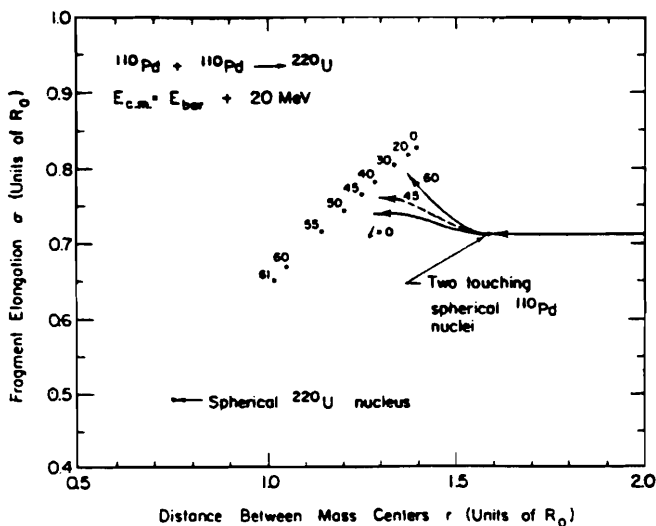


FIG. 2.7. Dynamical trajectories in the r - σ plane for the reaction $^{110}\text{Pd} + ^{110}\text{Pd} \rightarrow ^{220}\text{U}$ at a bombarding energy in the center-of-mass system that is 20 MeV above the maximum in the one-dimensional zero-angular-momentum interaction barrier. The dashed curve gives the trajectory for the critical angular momentum $l_{\text{crit}} = 45$. [From Nix and Sierk (77).]

indicated by the solid dots. The various lines leading from the contact point indicate the paths of the system on the R - σ plane. For all $l \leq 45$, the fission saddle points lie to the right of the trajectory, so that it becomes possible to form the compound nucleus. On the other hand, for $l > 45$, an *extra push* beyond 20 MeV will be necessary.

Swiatecki (82) has derived a simple algebraic expression for the extra push energy E_x . The final expression, including adjustment of constants through comparison with experiment, is given by Bjornholm (82) as

$$E_x = 200(x_e - 0.7)^2 \text{ MeV}$$

where

$$x_e \equiv \left(\frac{Z^2}{A} \right)_{\text{eff}} \left(\frac{Z^2}{A} \right)_{\text{crit}}$$

where

$$\left(\frac{Z^2}{A} \right)_{\text{eff}} = \frac{4Z_1 Z_2}{(A_1 A_2)^{1/3} (A_1^{1/3} + A_2^{1/3})} + \left(\frac{fl}{l_{\text{ch}}} \right)^2$$

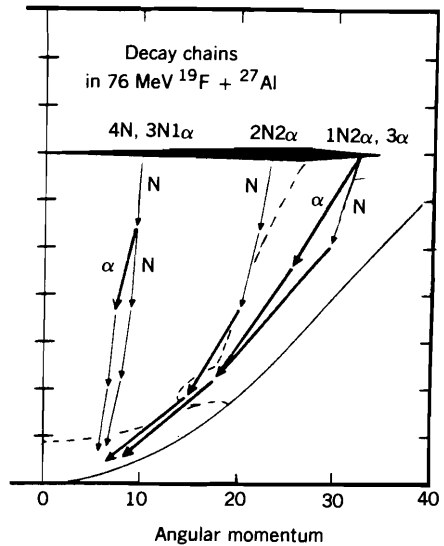


FIG. 2.8. The most likely chains in the reaction 76 MeV $^{19}\text{F} + ^{27}\text{Al}$ are shown for differing angular momenta of the compound nucleus ^{46}Ti . Heavy arrows are for α -particle emission, thin ones are for nucleon emission. [From Stokstad (85).]

$$\left(\frac{Z^2}{A}\right)_{\text{crit}} = 50.9 \left[1 - 1.78 \left(\frac{N_1 + N_2 - Z_1 - Z_2}{A_1 + A_2} \right) \right]^2$$

$$l_{\text{ch}}^2 = 0.0105 \frac{(A_1 A_2)^{4/3} (A_1^{1/3} + A_2^{1/3})^2}{A_1 + A_2} \quad (2.1)$$

and

$$f = 0.75 \pm 0.05$$

Fusion cross sections are determined by observing the products of the decay of the compound nucleus formed by the reaction. Usually, the compound nucleus will be highly excited and generally will therefore decay before they are detected. For light nuclei, nucleon and α -particle emission is compete. For high angular momentum states, α -particle emission is favored (see Fig. 2.8). γ -Ray emission becomes important near and below the threshold for particle emission. Fission is not significant for the light nuclei. For medium-weight nuclei, fission will compete with neutron emission, especially for high-angular-momentum states, while charged particle decay will be less important because of the Coulomb barrier. For heavy nuclei only fission and neutron emission compete. A statistical model calculation showing the competition between neutron and γ -ray deexcitation for ^{164}Er formed by a beam of ^{40}Ar incident on ^{124}Sn is illustrated in Fig. 2.9. We see that the emission of four neutrons followed by γ -ray emission is the most probable decay chain. By observing the residues, one can verify the assumption behind the calculation leading to Fig. 2.9.

A considerable help in this endeavor is obtained by observing the multiplicity $\langle M_\gamma \rangle$ of the emitted γ -rays. These are related to the average nuclear angular

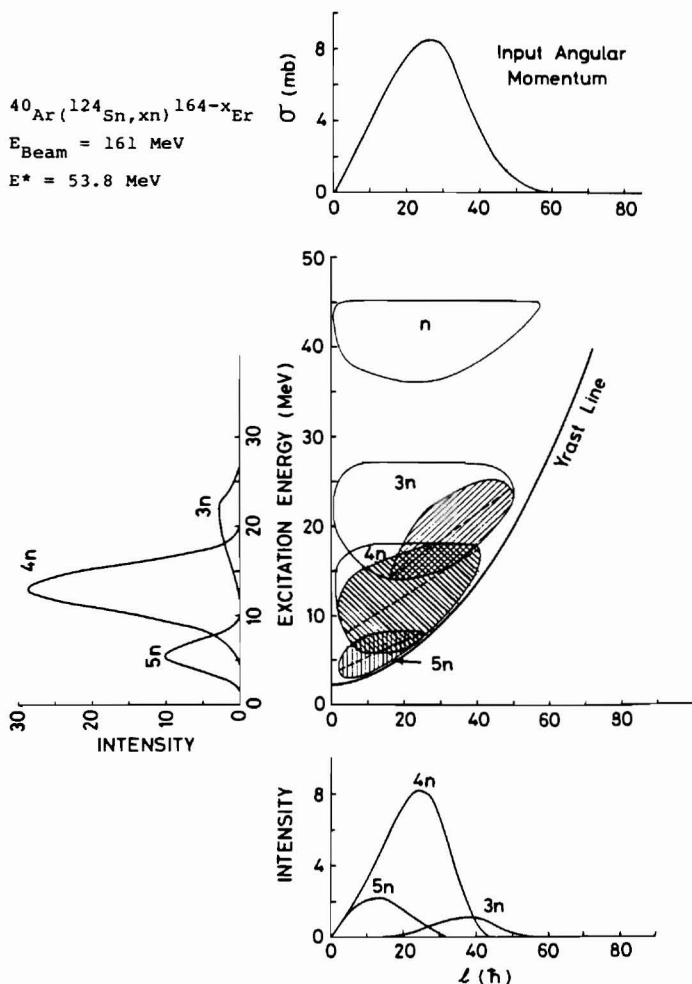


FIG. 2.9. Statistical model predictions for the decay of the ^{164}Er compound system formed at an excitation energy of 54 MeV with 147-MeV ^{40}Ar ions incident on ^{124}Sn . The assumed population of the ^{164}Er compound system is given as a function of angular momentum in the top portion of the figure. The calculated populations $\sigma(l, E^*)$ are indicated as a function of the excitation energy and angular momentum for the system after the emission of 1–5 neutrons. The shaded region of 3n–5n population shows the portion in which gamma-ray emission competes. The entry populations for the 3n–5n evaporation residues are indicated as a function of angular momentum and excitation energy at the bottom and to the left side of the figure. The predicted entry line is shown for each γ -ray emitting region [Tjøn, Espe, et al. (79)]. [From Stokstad (85).]

momentum l by the *empirical* formula

$$l = 2(M_y - 4) \quad (2.2)$$

As is evident from this last discussion, the statistical theory of nuclear reactions (Section IV.7) plays an important role in the analysis of heavy ion reactions. This is especially the case when one measures the number of nuclei of a given type produced in the reaction. For fusion reactions, since each such nucleus is a consequence of the reaction, one obtains a direct determination of the number of reactions that have occurred. One must add to this cross section, referred to as σ_{ER} (ER \equiv evaporation residues), the cross section that results in fission, σ_{FI} , to obtain the total cross section. However, both the deep inelastic and quasi-elastic can contribute to the observed results, especially for the light, nearly symmetric, colliding nuclei. Statistical theory may be used to separate the fusion and fission contributions. For heavier nuclei and higher energies, incomplete fusion may contribute particularly for the larger angular momenta. One would then find that the statistical theory would underestimate the number of α -particles, for example, produced. In the case of fissioning nuclei it is possible to determine the total momentum carried off by the fission fragments. Compared to the critical momentum, one can determine the missing momentum carried off before the system fissioned. Note that neutron emission from the compound nucleus will generally be spherical and therefore not contribute to the linear momentum balance.

The characteristic symmetry about 90° of reactions involving the formation of the compound nucleus (see Section IV.7) can be used to separate fusion from quasi-elastic and deep inelastic reactions. Applying directly the results of the statistical theory leads to comparisons with experiment that are quite good. Figure 2.10, which gives the experimental and statistical angular distributions in the reaction $^{12}\text{C} (^{14}\text{N}, ^6\text{Li})^{20}\text{Ne}$, is a typical example. A simple classical consideration [Ericson (60a); Ericson and Strutinski (58)] shows that under circumstances to be described below the angular distribution obeys a $1/\sin \vartheta$ law. One assumes that the spin of the residual nucleus and emitted particle are small with the consequence that the orbital angular momentum of the emitted particle that is perpendicular to the final momentum must align itself with the angular momentum of the compound nucleus (Fig. 2.11). Moreover, assume that the spin of the compound nucleus, I , acquired from the collision is also orbital and therefore in a plane perpendicular to the original direction. The angular distribution is then proportional to the Dirac delta function $\delta(\hat{\mathbf{k}}_F \cdot \mathbf{I})$. To obtain the observed angular distribution, we must average over the possible orientations \mathbf{I} :

$$\frac{d\sigma}{d\Omega} \sim \frac{1}{2\pi} \int_0^{2\pi} \delta(\hat{\mathbf{k}}_F \cdot \mathbf{I}) d\phi = \frac{1}{2\pi} \int_0^{2\pi} \delta(I \sin \vartheta \cos \phi) d\phi = \frac{1}{2\pi I \sin \vartheta} \quad (2.3)$$

completing the proof. Of course, this result fails near $\vartheta = 0$ and π . The critical

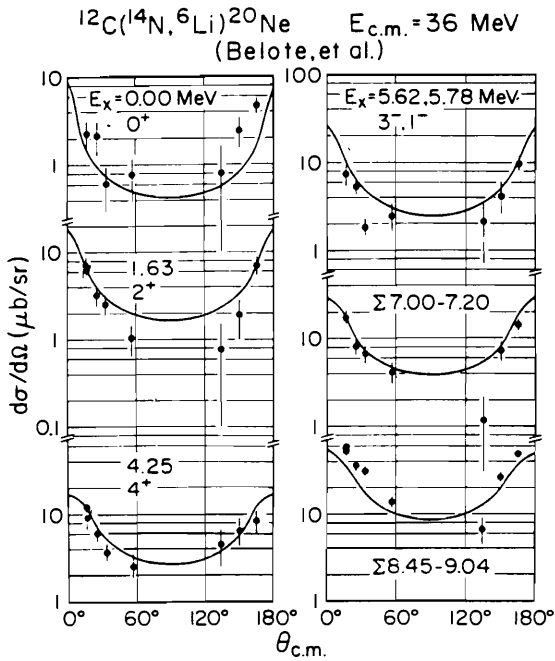


FIG. 2.10. Absolute Hauser-Feshbach statistical model calculations compared with experimental angular distributions for low-lying states in ^{20}Ne populated by the $^{12}\text{C}(^{14}\text{N}, ^6\text{Li})^{20}\text{Ne}$ reaction at $E_{\text{c.m.}} = 36 \text{ MeV}$ (Hanson, Stokstad, et al. (74)). [From Stokstad (85).]

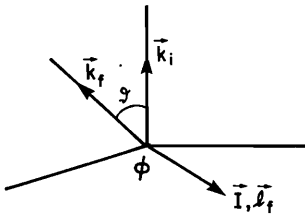


FIG. 2.11. Diagram for classical calculation of the angular distribution.

angle according to Ericson is j_f/J , where j_f is the spin of the emitted particle. Examples of the fit to this distribution are shown in Figs 2.12 and 2.13. Generally, comparison with experiment shows that the $1/\sin \theta$ distribution provides a good fit near 90° , but fails as one approaches the forward and backward directions.

In summary, the statistical theory of nuclear reactions can be used to (1) distinguish fusion from other reaction modes, (2) determine the spin of the compound nucleus formed, and (3) describe the decay of the compound nucleus, giving the yield of the particles emitted and their multiplicities. Fusion yields are also correctly given provided that one takes the density of final states to

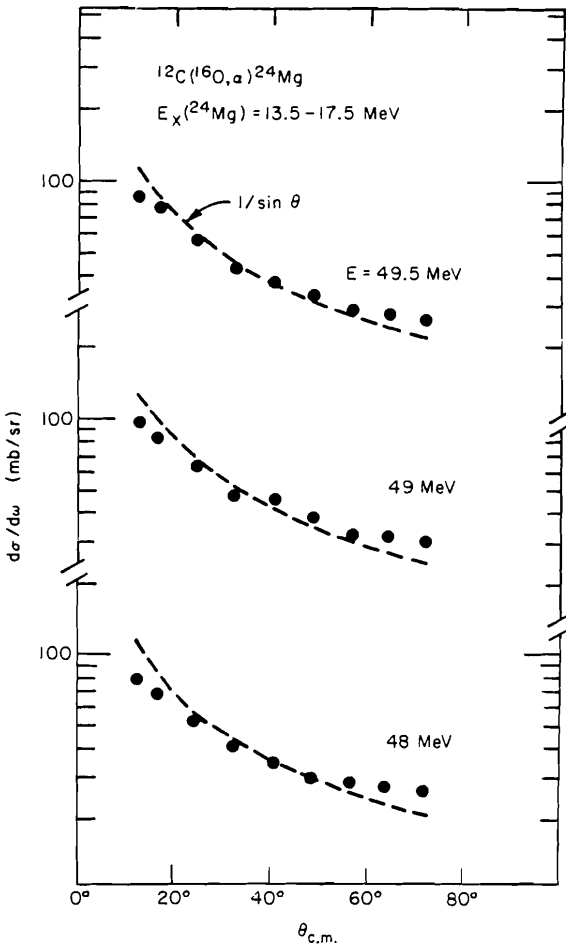


FIG. 2.12. Total α -particle angular distributions for $E_x = 13.5 - 17.5 \text{ MeV}$ in ^{24}Mg for incident energies of 48, 49, and 49.5 MeV. The dashed lines are least-squares fits to the function $1/\sin \theta$ [Greenwood, Katori, et al. (72)]. [From Stokstad (85).]

be the density of states of the compound nucleus at the fission saddle point [see Stokstad (85, pp. 115, 121, et seq.)]. In most cases the number of possible reaction paths is not small and even the statistical theory calculations become quite complex. As a consequence, several statistical model computer codes have been developed. These are listed to Stokstad (85, p. 125). Their use is discussed in the accompanying text. An important simplification has been recently obtained by Friedman and Lynch (83), who consider the time evolution of the evaporating systems. Their procedure should prove to be very useful.

Typical complete fusion cross sections are shown in Fig. 2.14. We note that in each of these cases the cross section falls on two straight lines. For low

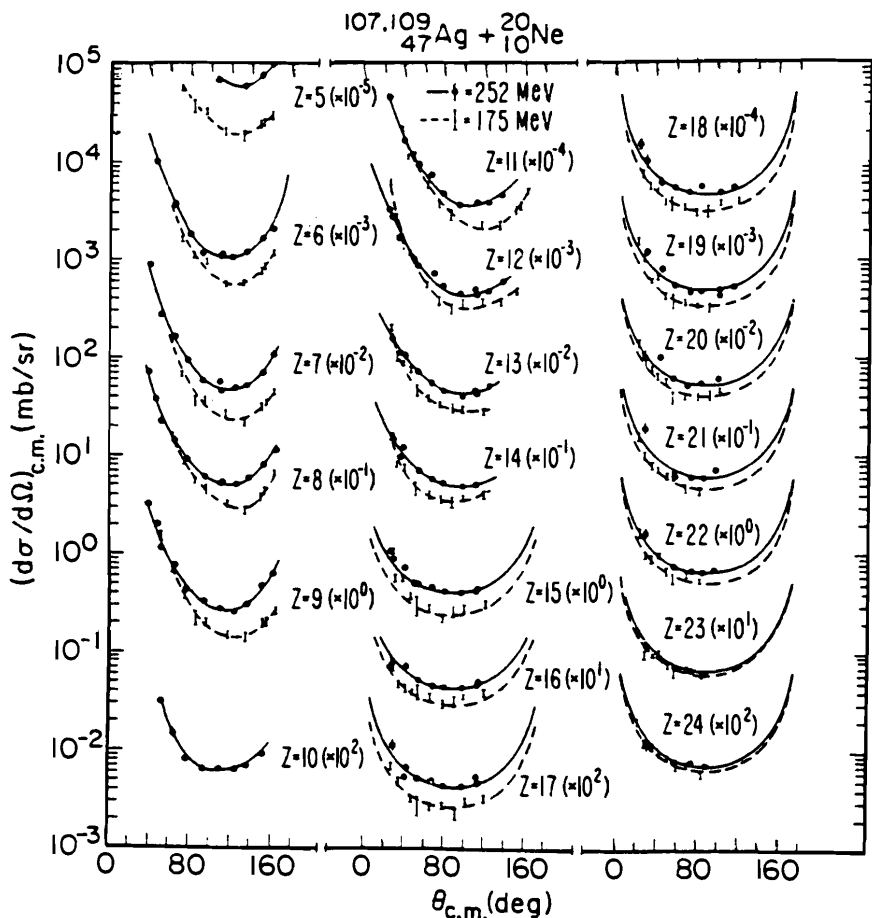


FIG. 2.13. The center-of-mass angular distributions of fragments from the reaction $^{107,109}\text{Ag} + ^{20}\text{Ne}$ at $E_{\text{lab}} = 175$ and 252 MeV. For fragment atomic numbers of $Z > 15$ curves drawn through the data correspond to $d\sigma/d\Omega \sim (\sin\theta_{c.m.})^{-1}$. [From Babinet, Moretto, et al. (76).]

energies, below the intersection of the two lines, referred to as region I, the fusion cross section σ_{CF} equals the reaction cross section σ_{R} , while for larger energies, region II $\sigma_{\text{CF}} \ll \sigma_{\text{R}}$. The one-dimensional radial model provides a simple explanation. In the low-energy region domain, the reaction, and therefore the fusion cross section, is given by

$$\sigma_{\text{R}} = \sigma_{\text{CF}} = \frac{\pi}{k^2} \sum_{l=0}^{\infty} (2l+1) T_l$$

where T_l are the transmission coefficients. One can calculate these from the

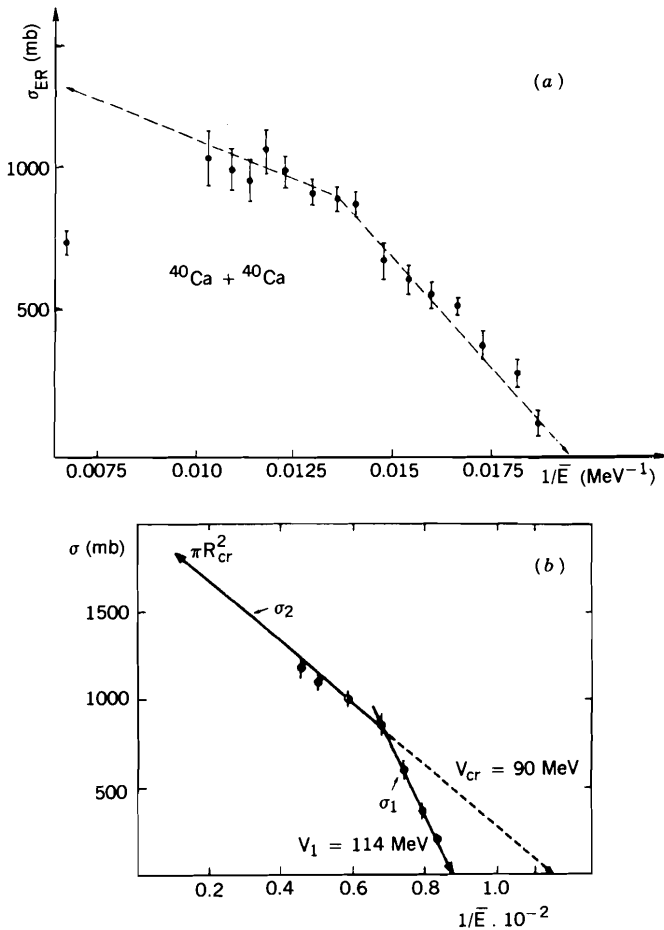


FIG. 2.14. Experimental fusion cross sections as a function of $(1/E)$: (a) medium-mass system $^{40}\text{Ca} + ^{40}\text{Ca}$; (b) heavy system $^{40}\text{Ar} + ^{121}\text{Sb}$. [From Lefort and Ngô (78).] (c) Fusion cross sections for $^{16}\text{O} + ^{27}\text{Al}$ compared with the formula of Glas and Mosel. [From Hodgson (78).]

optical model. A rough analytic approximation is obtained using the *sharp cutoff model*, in which

$$T_l = \begin{cases} 1 & \text{for } l \leq L \\ 0 & \text{for } l > L \end{cases} \quad (2.4)$$

Then

$$\sigma_{\text{CF}} = \frac{\pi}{k^2} \sum_0^L (2l+1) = \frac{\pi}{k^2} (L+1)^2 \simeq \frac{\pi}{k^2} L^2 \quad (2.5)$$

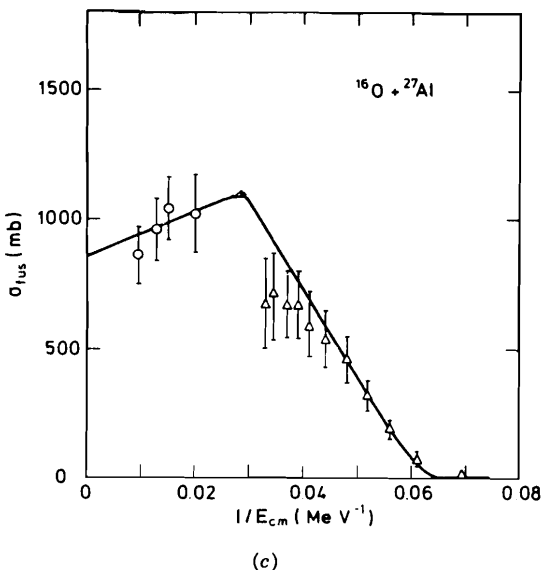


FIG. 2.14. (Continued)

Equation (2.4) corresponds to the assumption that for all l 's less than or equal to L , a minimum in the potential $V(R)$ exists which is of sufficient strength to trap the system for a long enough time for the interacting nuclei to fuse. For $R > L$, this is no longer possible. The value of L is given approximately by the effective wave number k_B at R_B multiplied by R_B , where $V(R)$ has its maximum. This recipe is verified by an optical model calculation. Thus

$$L = k_B R_B = k R_B \left(1 - \frac{V_B}{E}\right)^{1/2} \quad (2.6)$$

so that

$$\sigma_{CF} = \pi R_B^2 \left(1 - \frac{V_B}{E}\right) \quad (2.7)$$

in agreement with experiment. By comparing with experiment, one can determine R_B and V_B .

In region II, that is, at greater energies, the collision does not necessarily lead to fusion. The potential does not have a minimum of sufficient strength to trap the system. However, fusion can occur some fraction of the time if a sufficient interchange of mass and energy between the two nuclei has occurred: macroscopically, if friction has slowed the system down enough. This slowing-down process is more effective as R decreases, and for a sufficiently small R , R_C , will lead to fusion. One can calculate the probability of this occurring by assuming that for $r \geq R_C$, the wave function for the system

consisting of the colliding nuclei in this ground state is zero because of the probability of excitation and mass transfer. Using the WKB method for penetration through a parabolic barrier [Glas and Mosel (74, 75); Wong (72, 73), one obtains

$$\sigma_{\text{CF}} = \frac{\hbar\omega}{2E} R_B^2 \ln \frac{1 + e^{2\pi(E - V_B)/\hbar\omega}}{1 + e^{2\pi[E - V_B - (R_C/R_B)^2(E - V_B)]/\hbar\omega}} \quad (2.8)$$

where $\hbar\omega$ measures the width of the barrier and V_C is the potential at R_C . For high energies,

$$E \left[1 - \left(\frac{R_C}{R_B} \right)^2 \right] \gg V_B - \left(\frac{R_C}{R_B} \right)^2 V_C$$

one obtains

$$\sigma_{\text{CF}} = \pi R_C^2 \left(1 - \frac{V_C}{E} \right) \quad (2.9)$$

in agreement with experiment. At low energies,

$$\sigma_{\text{CF}} = \frac{\hbar\omega}{2E} R_B^2 \ln [1 + e^{2\pi(E - V_B)/\hbar\omega}] \rightarrow \pi R_B^2 \left(1 - \frac{V_B}{E} \right)$$

in agreement with (2.7). The quantity V_C is negative for Fig. 2.14a, while for Fig. 2.14b and c, V_C is positive. Empirically,

$$R_C = r_C (A_1^{1/3} + A_2^{1/3}) \quad r_C = 1 \pm 0.07 \text{ fm} \quad (2.10)$$

where A_1 and A_2 are the mass numbers of the interacting nuclei. Of course, one can compute σ_{CF} directly from the optical model with appropriate boundary conditions at R_C .

There are substantial disagreements of (2.8) with experiment which are exhibited when the cross sections for heavy-ion fusion reactions leading to the same compound nucleus are compared. One would not expect to the fusion cross sections $^{14}\text{N} + ^{12}\text{C}$ and $^{16}\text{O} + ^{10}\text{B}$ to differ greatly, but they do. It is also surprising that the cross section for reaction $^{14}\text{N} + ^{12}\text{C}$ differs substantially from that of reaction $^{15}\text{N} + ^{12}\text{C}$. This has led to the development of an alternative explanation of the cross sections for region II based on Yrast line considerations discussed above [Harar (78); Matsuse, Arima and Lee (82)]. The critical value, L , is now given by the maximum value L , which is permitted by the Yrast line. For larger values of L , states of the compound nucleus do not exist. The value of L is given by the equation

$$E + Q = \hbar^2 \frac{L(L+1)}{2\mathcal{I}} + \Delta Q \quad (2.11)$$

where \mathcal{I} is the Yrast moment of inertia. ΔQ is the band head energy [Harar (78)]. Substituting in (2.5), one obtains

$$\sigma_{\text{CF}} = \frac{\pi \mathcal{I}}{\mu} \left(1 + \frac{Q - \Delta Q}{E} \right) \quad (2.12)$$

where μ is reduced mass. An example of the efficacy of this equation is provided by the comparison of the two reactions $^{14}\text{N} + ^{12}\text{C}$ and $^{16}\text{O} + ^{19}\text{B}$, which lead to the same compound nucleus ^{16}Al . These two reactions give very different cross sections. However, the relation between $E^* = E + Q$ and L determined empirically for these two reactions is identical. One can go further and compare the theoretical and empirical \mathcal{I} . One finds that the empirical values of L are consistently smaller than the values predicted by calculations of the Yrast line. Vandenbosch (79) and Vandenbosch and Lazzarini (81) make the reasonable suggestion that the compound nucleus formation will occur only if there is a sufficient density of levels, which would move the predicted value of L away from the Yrast line to smaller values of L . According to Mosel (84), the question of whether it is the density of compound nuclear levels or the density of doorway states leading to compound nucleus formation has not been resolved.

Investigation of the fusion cross section at higher energies reveal another straight-line dependence on $1/E$, as illustrated in Fig. 2.15. This is referred to as region III. Matsuse, Arima, and Lee (82) propose a description in which the cross section for region I is given by (2.7), region II by the Yrast limit, (2.12), and region III by (2.9), where we recall that r_C is the distance at which the two colliding nuclei lose their identity and become the compound nucleus. This distance can be determined according to Matsuse et al. from the equation giving the mean-square radius of the compound nucleus mass number A in terms of

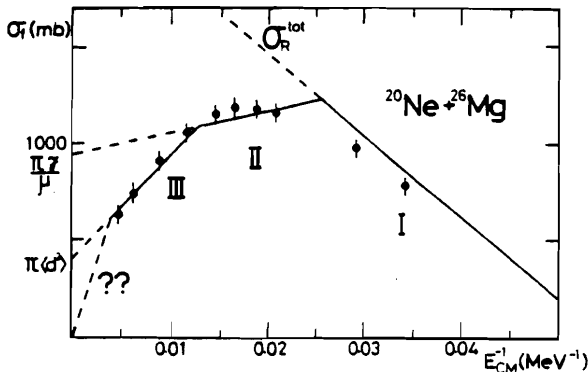


FIG. 2.15. Fusion cross-section excitation function Experiment (ϕ) compared with theory of Matsuse et al. [From Matsuse, Arima, and Lee (82).]

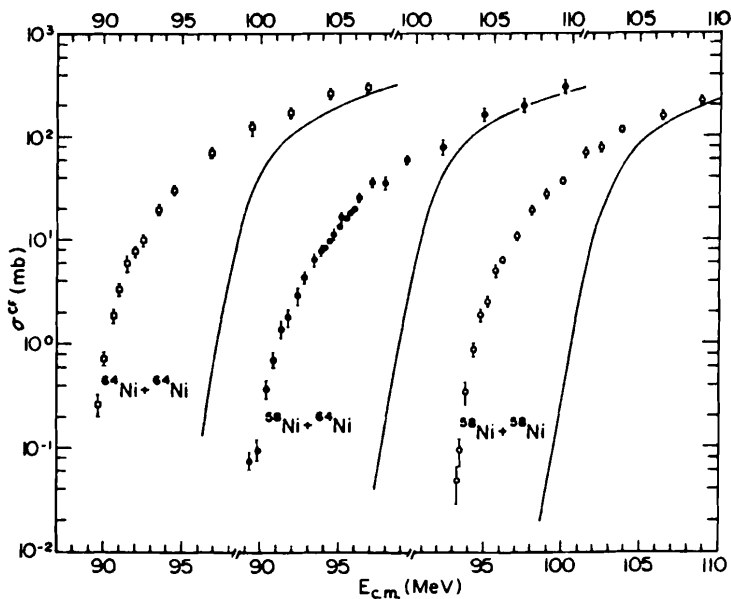


FIG. 2.16. Excitation functions for complete fusion of $^{58}\text{Ni} + ^{58}\text{Ni}$, $^{58}\text{Ni} + ^{64}\text{Ni}$, and $^{64}\text{Ni} + ^{64}\text{Ni}$. Smooth curves give WKB predictions. [From Beckerman (85).]

the mean-square radii of the colliding nuclei, A_1 and A_2 .

$$A \langle r^2 \rangle_A = A_1 \langle r^2 \rangle_{A_1} + A_2 \langle r^2 \rangle_{A_2} + \frac{A_1 A_2}{A} \langle r_c^2 \rangle$$

For further details the reader is referred to their paper.

We conclude this section on fusion with a brief mention of the recently discovered phenomenon of *subbarrier fusion* [Steadman (85)], which is illustrated by Fig. 2.16. The center-of-mass energies are far below the Coulomb barrier energy for two touching spherical nuclei. One would there expect that the Coulomb interaction would dominate this reaction and that therefore one should be able to calculate the cross section with some confidence. However, calculations made with the one-dimensional radial model given approximately by the solid lines fall far below the experimental values. Nearly all the various explanations for these major discrepancies can be understood as examples of coupled-channel calculations, which take into account the vibration of the nuclear surfaces. As one may expect, the coupling to low-lying collective states is of major importance. This is illustrated by Fig. 2.17.

Henning, Wolfs et al. (87) have emphasized the importance of nuclear transfer for the observed fusion enhancement. This is based on experiments using $^{16,18}\text{O}$ and ^{58}Ni beams incident on Sn isotopes in which a strong correlation between the transfer cross section and fusion enhancement is seen. They suggest that

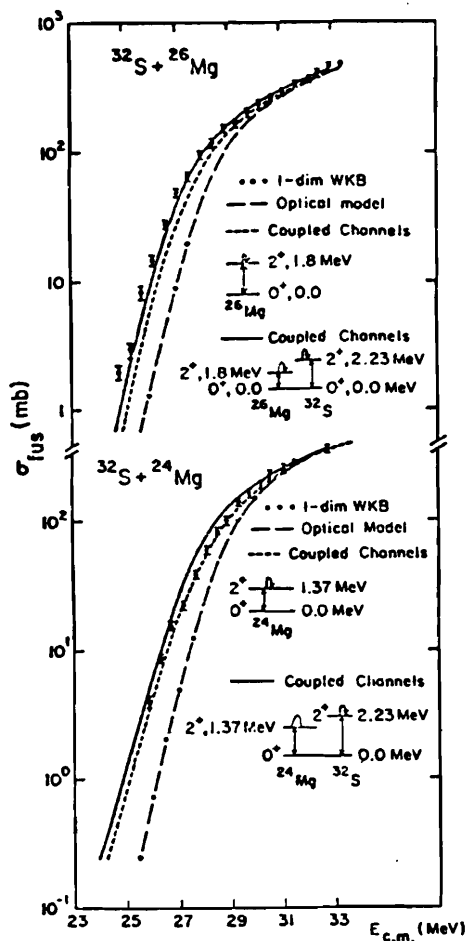


FIG. 2.17. Calculation of fusion cross section for the reactions $^{32}\text{S} + ^{26}\text{Mg}$ and $^{32}\text{S} + ^{24}\text{Mg}$. The dotted and long-dashed line are for the two equivalent one-dimensional calculations. The other curves show the effect of coupling in various low-lying states in ^{32}S and/or $^{24,26}\text{Mg}$. [From Rhoades-Brown, Braun-Munzinger, Prakash, and Sen (85).]

the neutron transfer opens a doorway through which the system can proceed to fusion. These reactions are of great importance in astrophysics, where they play an important role in energy production and element formation [Barnes (85)].

3. DEEP INELASTIC SCATTERING[‡]

As has been illustrated in Fig. 1.15, in deep inelastic collisions, the two interacting nuclei are thought to be in contact for a relatively long time, during which the combined system rotates through a finite fraction of a complete revolution

[‡]Schröder and Huizenga (84); Lefort and Ngô (78).

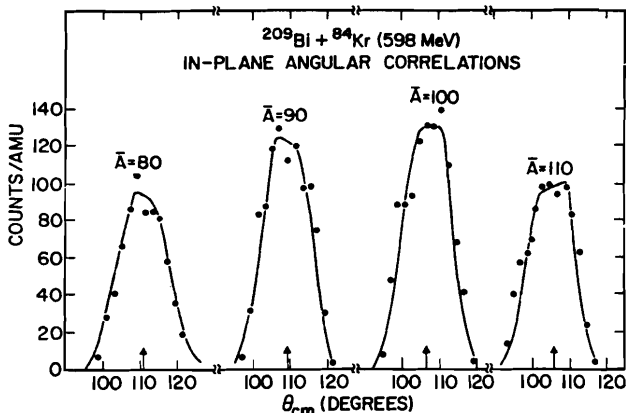


FIG. 3.1. In-plane angular correlation of fragments from the reaction $^{209}\text{Bi} + ^{84}\text{Kr}$ at 600 MeV, where the light fragment of mass A was measured at $\theta_L = 48.5^\circ$. The average emission angles expected from two-body kinematics are indicated by arrows. The curves represent an evaporation calculation [Wolf and Roche (76).] [From Schröder and Huizenga (84).]

before separating into two final fragments. The fact that the reaction is essentially binary is demonstrated by Fig. 3.1, where the angular correlation of the fragments is shown for differing values of the mass number of the lighter fragments. The average emission angles of the heavier fragment, calculated by assuming two-body kinematics, is indicated by arrows. The agreement with the maxima of the correlation distributions is excellent. The distributions are a consequence of evaporation of the fragments, so that the original values of A must be determined from statistical reaction theory. On the average, the evaporated particles are emitted isotropically, so that the average provides a good measure of the direction of the fragment upon separation from the lighter fragment. The binary character of deep inelastic scattering helps to distinguish the deep inelastic collision from a fusion reaction that is followed by fission. The latter is generally symmetric (i.e., the fusion leads to two nearly identical fragments). If the collision under consideration is between two nuclei with significantly differing atomic and mass numbers, the deep inelastic process will lead most probably to two final nuclei with substantially the same value of A and Z and not to two nearly identical nuclei.

In general, fusion is improbable for heavier elements (see Fig. 3.2). For these elements the strength of the Coulomb potential is so great that even with the addition of an attractive nuclear potential, no "pocket" in the total potential is formed. Hence no fusion. For this reason, we shall choose the illustrations of various phenomena associated with deep inelastic scattering to be discussed below, from collision between nuclei the product of whose charges ($Z_1 Z_2$) is greater than roughly 3000.

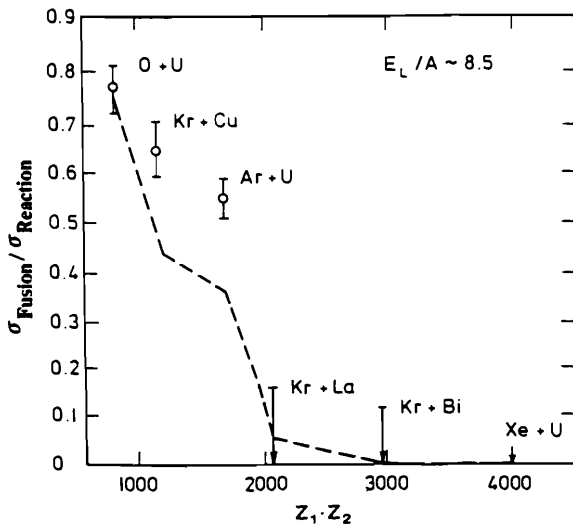


FIG. 3.2. Ratio of reaction to fusion cross section for several reactions involving heavy targets. [Vandenbosch (79); From Mosel (84).]

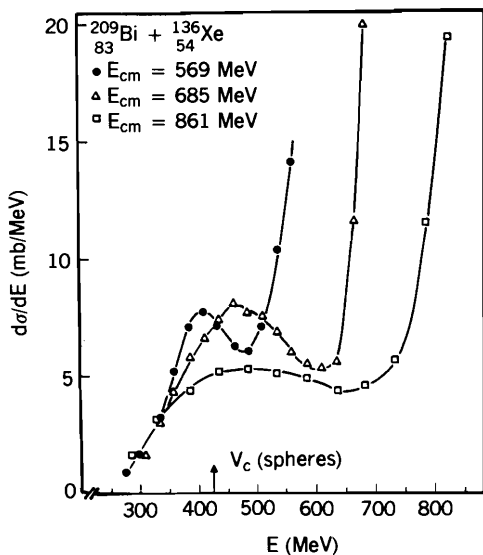


FIG. 3.3. Total kinetic energy distribution $d\sigma/dE$ of final fragments produced in the reaction $^{209}\text{Bi} + ^{136}\text{Xe}$ at three bombarding energies. The energies were calculated from the measured projectile-like fragments assuming two-body kinematics. The energy spectra are integrated over all fragments and reaction angles. The arrow (V_c) indicates the entrance channel Coulomb interaction energy at the strong-absorption radius. [From Huizenga and Birkelund (82).]

Another characteristic of deep inelastic collision is the wide range of energies that can be lost from the kinetic energy of relative motion to internal degrees of freedom. This feature distinguishes it from the quasi-elastic scattering, in which the binary final state is retained but the loss of energy is relatively small. In Fig. 3.3 the cross section for a final kinetic energy E produced by the collision of $^{209}_{83}\text{Pb}$ with $^{136}_{54}\text{Xe}$ is shown for three differing initial kinetic energies. These cross sections are obtained after integration over all angles and summing over all fragments. Near the initial energy we see a strong quasi-elastic peak. At a lower final energy there is a broad maximum in the distribution corresponding to an energy loss ranging from 170 MeV for the lowest initial energy to 370 MeV for the greatest critical energy. The distributions are very broad. Energy losses as high as 600 MeV for an incident energy of 861 MeV have been recorded.

The dependence of the total kinetic energy cross sections on the atomic number of the lighter fragment is shown in Fig. 3.4. Quasi-elastic peaks are seen for the Z of the fragment equal to the atomic number of the projectile $^{136}_{54}\text{Xe}$ and nearby $\langle Z \rangle = 57$. However, the quasi-elastic peak disappears quite rapidly as $\langle Z \rangle$ differs from 54. In these cases the energy distribution follows a bell-shaped curve. The widths of the distribution as well as the maximum value of the cross section decreases with increasing $\langle Z \rangle$ beyond $\langle Z \rangle = 54$.

Two differing types of angular distributions can be seen in deep inelastic collisions. The strong focusing distribution that prevails in the collisions of the very heavy nuclei after integration over energy and fragmentation type is

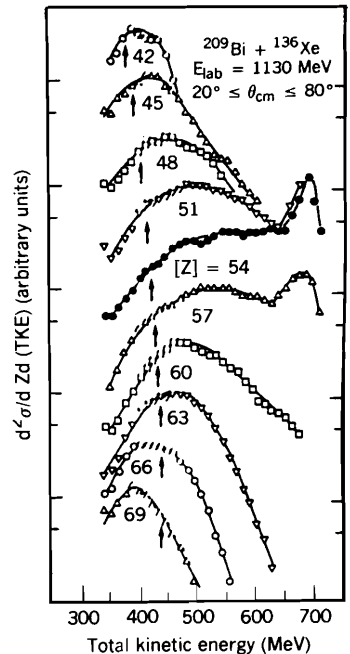


FIG. 3.4. Double-differential cross section $d^2\sigma/dZdE$ for the reaction $^{209}\text{Bi} + ^{136}\text{Xe}$ at $E_{\text{lab}} = 1130 \text{ MeV}$ integrated over $20^\circ \leq \theta_{\text{cm}} \leq 80^\circ$ [Schröder, Birkelund, et al. (78)]. [From Schröder and Huizenga (84).]

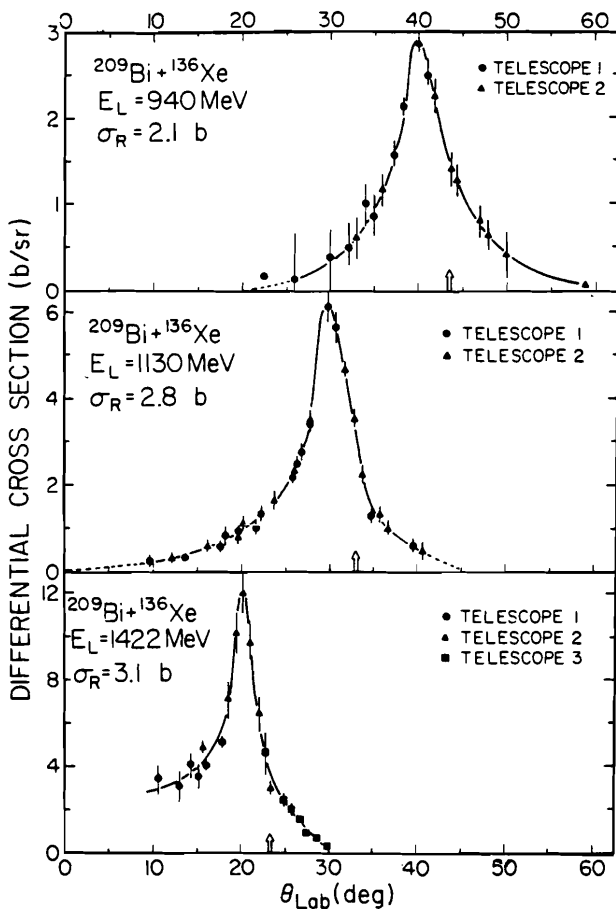


FIG. 3.5. Laboratory angular distributions for the $^{209}\text{Bi} + ^{136}\text{Xe}$ reaction at three energies. The centre-of-mass energies above the Coulomb barrier are 1.75, 3.14, and 5.29 MeV/nucleon, respectively. [From Schröder and Huizenga (84).]

illustrated in Fig. 3.5. The reaction products fall within a narrow angle peaked roughly at the grazing angle. The strong focusing is also exhibited by the Wilczyński plot of Fig. 3.6, where a contour plot of $d^2\sigma/d\Omega d(\text{TKE})$ in the $\text{TKE}-\vartheta_{\text{cm}}$ plane is shown ($\text{TKE} = \text{total kinetic energy}$). The ridge of the maximum cross section stays at a constant angle with increasing kinetic energy loss, but eventually as in the orbiting case, the rate of energy loss with angle slows down appreciably. The width of the angular distribution increases as the energy loss increases.

The angular distribution for each fragment integrated over the final fragment energies is shown in Fig. 3.7. The strong focusing effect at the grazing angle is visible for the fragments whose atomic number is near that of the projectile

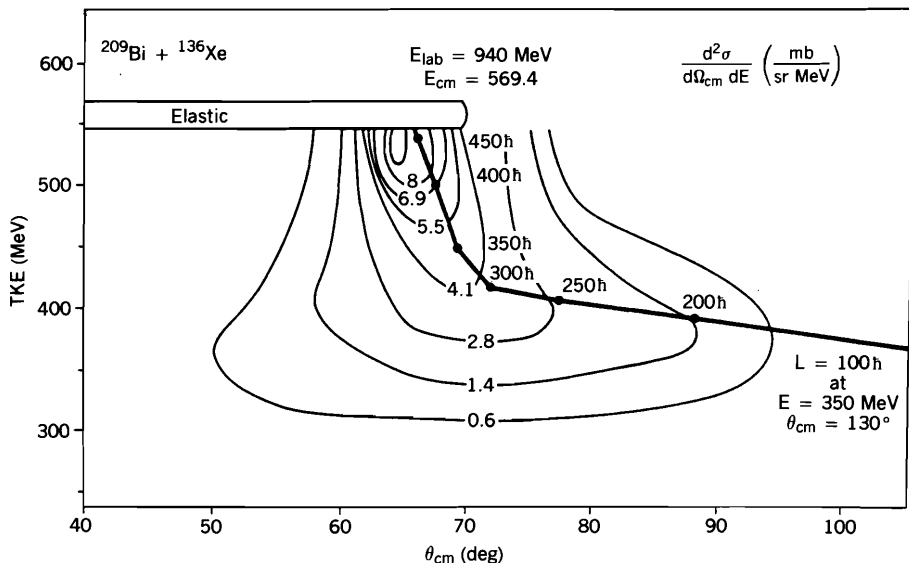


FIG. 3.6. Wilczyński plot for $^{137}\text{Xe} + ^{209}\text{Bi}$ at $E_{\text{lab}} = 9$ MeV. [From Negele (82).]

$Z = 54$. For changes from 54 of six units or larger the angular distributions broaden considerably.

The second type of angular distribution is a consequence of the *orbiting* process. It occurs for the lighter systems and higher energies. A typical Wilczyński plot for the orbiting process is shown in Fig. 3.8. The colliding nuclei are ^{18}Ar and ^{232}Th . Along the maximum cross-section ridge, the angle at first decreases rapidly, as the energy loss increases, approaching zero, and then increases quite slowly for further losses in energy. This last branch has been interpreted by Wilczyński (73) as negative angle reactions. His reasoning is illustrated by Fig. 3.9. Deep inelastic collisions are supposed to occur for those values of l (or impact parameters) that lie between l_{crit} and l_g . For $l < l_{\text{crit}}$, fusion dominates, while for $l > l_g$, quasi-elastic processes are the principal reaction channels. The trajectories near l_g will be Coulomb dominated, but as one moves away from l_g , the nuclear interaction will become more important, there will be an energy loss as a consequence, and the trajectory will be bent toward zero degrees and eventually beyond it to negative angles. Detectors do not distinguish between negative and positive angles, so that as the reaction angle passes zero, the cross sections as shown in the Wilczyński plot will be recorded as positive. We also see that the negative angle branch is closely associated with large energy loss.

The two types of angular distribution, orbital and angular focusing, are examples of extreme situations, angular focusing dominating for collisions between heavy nuclear and lower energies. The transition from one type to

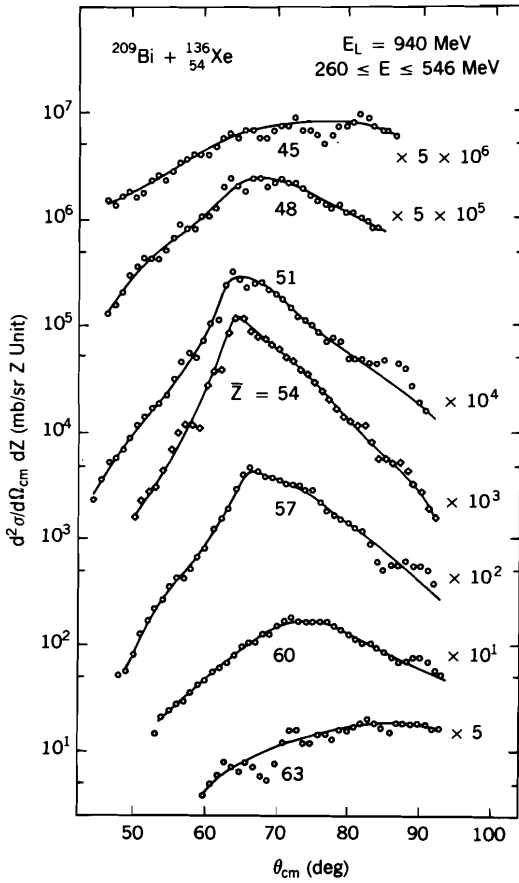


FIG. 3.7

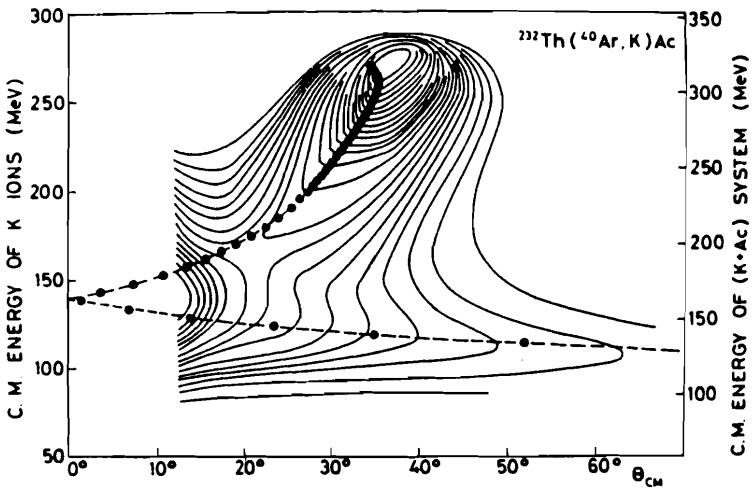


FIG. 3.8

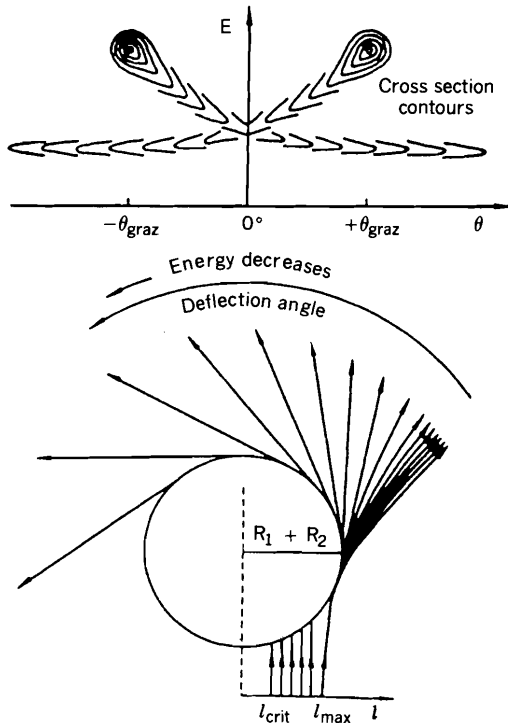


FIG. 3.9. Illustration of the orbiting phenomenon in damped nuclear reactions. Trajectories for a band of l waves between l_{max} and the critical angular momentum l_{crit} for fusion are depicted at the bottom. The associated cross section pattern is displayed at the top as a contour diagram plotted vs. final fragment energy E and deflection angle θ . Negative reaction angles correspond to rotation of the intermediate system through the beam direction ($\theta = 0^\circ$). [From J. Wilczyński (73).]

another has been found to depend empirically [Galín (76); Moretto and Schmitt (76)] on the Sommerfeld parameter evaluated at the Coulomb barrier:

$$\eta' = \frac{e^2 Z_p Z_t}{\hbar} \left[\frac{\mu}{2(E_{\text{cm}} - V_{\text{Coul}})} \right]^{1/2} \quad (3.1)$$

FIG. 3.7. Center-of-mass angular distributions of the light fragments from the damped reaction $^{209}\text{Bi} + ^{136}\text{Xe}$ at $E_{\text{lab}} = 940 \text{ MeV}$ as a function of Z . The experimental double-differential cross sections are multiplied by the factors listed on the right before plotting. [From Wilcke, Birkelund, et al. (80).]

FIG. 3.8. Contour diagram of $d^2\sigma/dE d\theta$ for the reaction $^{232}\text{Th}(^{40}\text{Ar}, \text{K})$ at $E_{\text{lab}} = 388 \text{ MeV}$. The circles indicate the predicted correlation between scattering angle and final energy for different values of the angular momentum ranging from $l = 180$ to 250. [From Lefort and Ngô (78).]

Empirically, orbiting dominates for $\eta' \lesssim 150$, while angular focusing dominates in the range $250 \lesssim \eta' \lesssim 400$. For $\eta' \gtrsim 500$ angular focusing is accompanied by a noticeable tail at larger angles.

As we shall see, correlations among many of the observables are observed. Some insight into these can be obtained from the dependence of observables on the interaction time, τ , that is, the time during which the colliding nuclei interact before separating. One expects that τ will be smallest for the largest values of the impact parameter (or l) and will increase as l decreases. This suggests two characteristic times, corresponding to two different dynamical situations. One time, τ_a , is the time required to achieve a approximate saturation value of the energy loss, achieved in this case for $l = 300$. For larger interaction times corresponding to smaller values of l , the energy loss increases very slowly with decreasing l . In the first phase, the conversion of kinetic into internal energy is generated by the flow of matter, nucleons, or clusters of nucleons from one nucleus to the other and/or the excitation of giant resonances as the surface regions of each interact.

A rough estimate of the time involved can be deduced from experiment by the following argument. In the laboratory frame, assume that the target nucleus is excited by the flow of nucleons from the projectile while the projectile is slowed down by the flow of nucleons from the target. The energy carried by each nucleon entering the target is E/A_p , where E is the incident energy of the projectile. A rough estimate of the total energy transferred to the target is obtained by assuming thermal equilibrium between the projectile and target. That energy is $(A_t/A_p + A_t)\Delta E$, where ΔE is the total energy loss. Thus the number of nucleons transferred to the target is

$$n = \frac{A_t A_p}{A_p + A_t} \frac{\Delta E}{E}$$

The time it takes each nucleon to transfer is given approximately by the distance traversed, on the order of the surface thickness s divided by the Fermi velocity. Thus the time τ_1 for the first phase is

$$\tau_1 = \frac{ns}{v_F} = \frac{A_t A_p}{A_p + A_t} \frac{s}{v_F} \frac{\Delta E}{E}$$

Turning to our example, for $l = 300$, $\Delta E = 169$ MeV, $E = 940$ MeV, $s \sim 2$ fm, and $v_F/c \sim 0.27$, we obtain 3.6×10^{-22} s and $n \sim 15$. This crude result appears to be of the correct order of magnitude as obtained from calculations using macroscopic and microscopic models.

The second phase must involve low-lying modes of excitation. The models suggest that their major effect is the slowing down of the rotational motion. The mechanism is analogous to the slowing-down action of the tides. The rotational states are thus the modes excited. The time involved is given by the

uncertainty principle by

$$\tau_2 = \frac{\hbar}{\Delta E}$$

where ΔE is of the order of 160 keV, so that $\tau_2 \sim 10^{-20}$ s, a much longer time than that occupied by the first phase.

The results above are characteristic of very heavy systems. For lighter ones the second phase is replaced by fusion, which does not occur for the heavier systems, as discussed earlier.

These considerations become explicit and quantitative in the macroscopic friction model of Gross and Kalinowski (78). Two variables are used, the distance r between the centers and φ the angle made by \mathbf{r} with the incident direction. The Newtonian equations of motion are then

$$\frac{d}{dt}(\mu\dot{r}) - \mu r\dot{\varphi}^2 + \frac{dV}{dr} + K_r\dot{r} = 0 \quad (3.2)$$

and

$$\frac{d}{dt}(\mu r^2\dot{\varphi}) + K_\varphi r^2\dot{\varphi} = 0 \quad (3.3)$$

The quantity μ is the reduced mass, while K_r , the radial friction coefficient, and K_φ , the tangential one, are both functions of r . The function V , the potential, nuclear plus Coulomb, is taken to be a function of r only. These are the most general parity-conserving equations with friction forces linearly dependent on \dot{r} and $\dot{\varphi}$. Gross and Kalinowski take point Coulomb potentials and the folding potential,

$$V_{12}(r) = \int V_1(|\mathbf{r} - \mathbf{r}'|)\rho_2(\mathbf{r}') d\mathbf{r}'$$

where V_1 is a real Woods–Saxon potential describing the interaction of a nucleon in nucleus designated by the subscript 2, with the nucleus designated by the subscript 1 integrated over nucleus 2. The function V in (3.2) is $V_N + Z_1Z_2e^2/r$, where $V_N = \frac{1}{2}(V_{12} + V_{21})$. The function ρ_2 is taken from electron scattering. Thus Gross and Kalinowski (78) use

$$\begin{aligned} \rho(r) &= \frac{\rho_0}{1 + e^{(r-R_D)/a_D}} & V_1 &= \frac{V_0}{1 + e^{(r-R_p)/a_p}} \\ \rho_0 &= 0.17 \text{ fm}^{-3} & V_0 &= -50 \text{ MeV} \\ R_D &= 1.12 - 0.86A^{-1/3} \text{ fm} & R_p &= 1.25A^{1/3} \\ a_D &= 0.54 \text{ fm} & a_p &= 0.65 \text{ fm} \end{aligned} \quad (3.4)$$

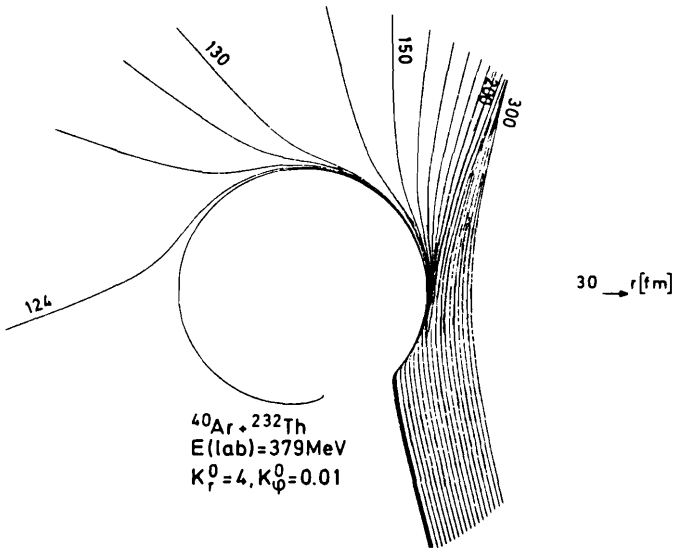


FIG. 3.10. Trajectories given by the friction model for various values of l . The last contribution to the fusion cross section is $l = 122$; the first to the deep inelastic cross section is $l = 124$. [From Gross and Kalinowski (78).]

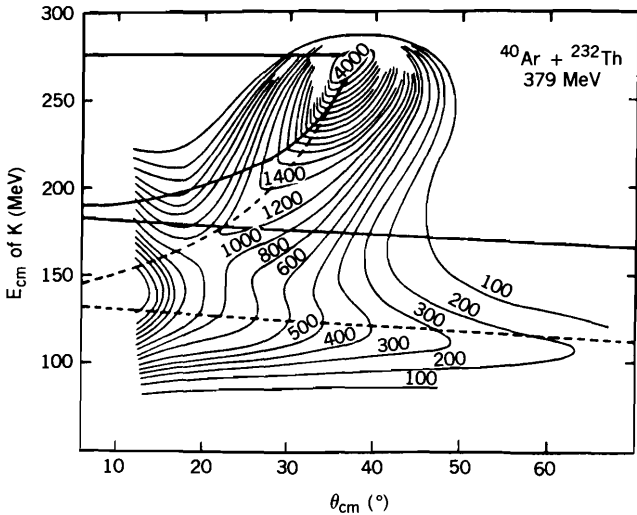


FIG. 3.11. Contour diagram of $df/ds d\theta$ ($\mu\text{B}/\text{MeV} \cdot \text{rad}$) versus scattering angle θ_{cm} and E_{cm} of K ions. The dashed line contains the effects of deformation. [From Gross and Kalinowski (78).]

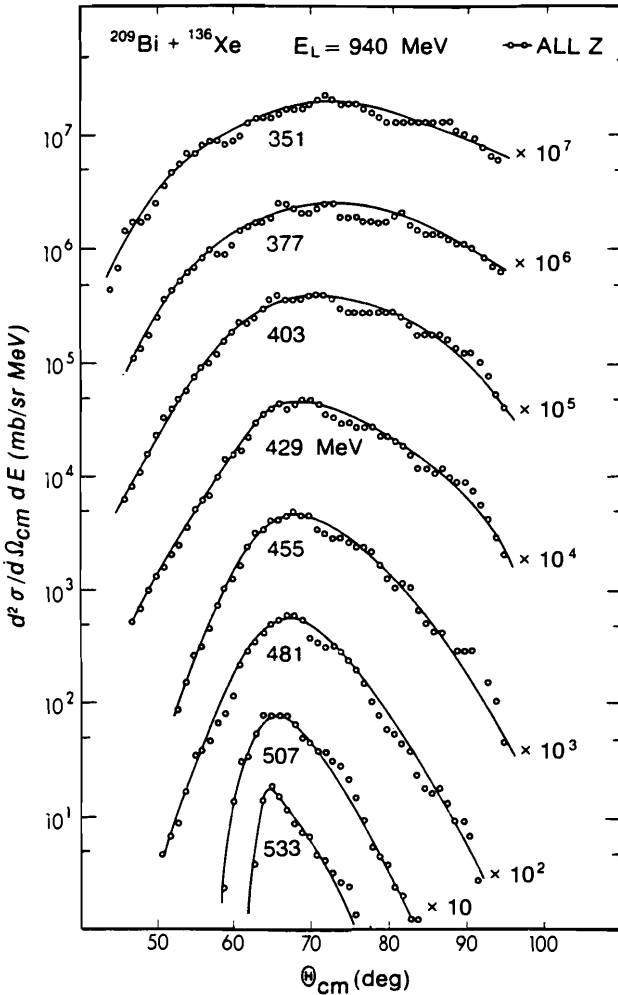


FIG. 3.12. Angular distribution as a function of total kinetic energy for the $^{209}\text{Bi} + ^{136}\text{Xe}$ reaction at $E_{\text{lab}} = 940$ MeV. Each energy bin is 26 MeV wide and is integrated over Z of the light fragments. The centroid energy of each bin is given at each curve. The solid lines are drawn through the data points. [From Wilcke, Birkelund, et al. (80).]

For the friction coefficients, these authors use the following:

$$K_r = K_r^0 (\nabla V_N)^2 \quad K_\phi = K_\phi^0 (\nabla V_N)^2 \quad (3.5)$$

These friction coefficients are most important in the surface region. The constants K_r^0 and K_ϕ^0 are taken from fits to experiment to be 4×10^{-23} and 10^{-25} s/MeV, respectively. The tangential friction is therefore much weaker than the radial one as might expect.

The time constant for the decay of the tangential motion as obtained from (3.3) is of the order of μ/\bar{K}_ϕ , where \bar{K}_ϕ is the ratio of the averages $\langle K_\phi r^2 \rangle$ and $\langle r_2 \rangle$. Estimating ∇V as $|V_0|/4a$, where $a \simeq a_D + a_p = 1.19$ fm, one obtains

$$\tau \sim 2 \times 10^{-22} \text{ s}$$

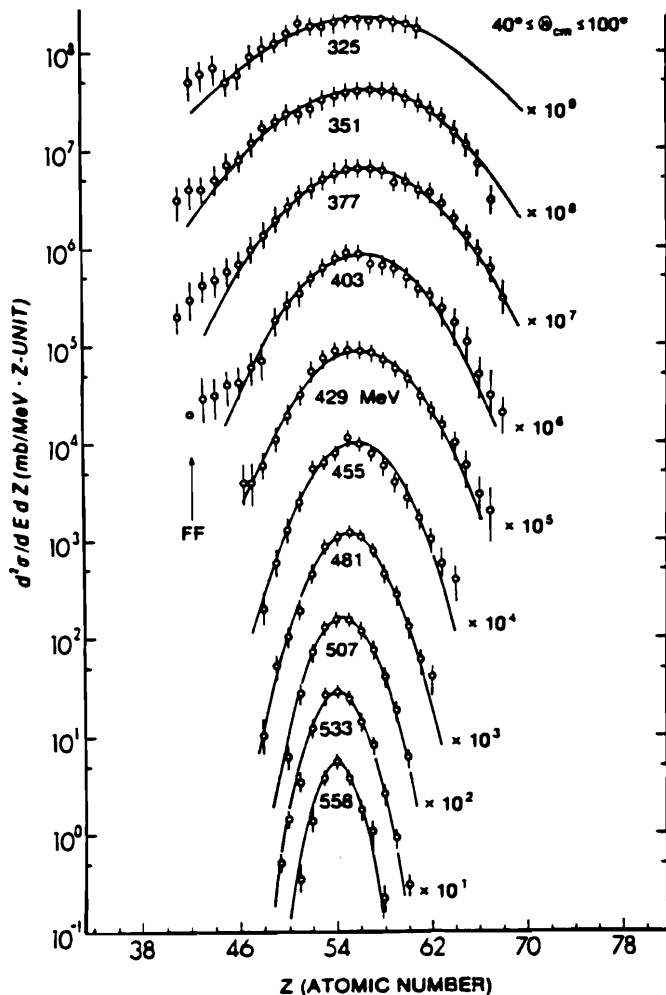


FIG. 3.13. Z distributions of fragments from the reaction $^{209}\text{Bi} + ^{136}\text{Xe}$ at $E_{\text{lab}} = 940$ MeV are plotted as a function of final total kinetic energy indicated at the curves. Energy bins are MeV wide. Solid curves represent Gaussian fits to the data (open circles). The distribution 558 MeV corresponds to elastically scattered Xe ions and illustrates the experimental resolution. The arrow (FF) indicates contamination of the data by events from sequential fission of target-like reaction fragments. [From Wilcke, Birkelund, et al. (80).]

which is close to the estimate made above. Gross and Kalinowski have given some results using (3.2), (3.3), and (3.10) which do (with one further adjustment!) reproduce the observed data to the extent that their model permits. In Fig. 3.10, the trajectories for the reaction $^{40}\text{Ar} + ^{232}\text{Th}$, laboratory energy of 379 MeV, are shown. The trajectories for angular momentum $l \geq 124$ contribute to the deep inelastic cross section, which those for $l \leq 122$ to the fusion cross section. The process pictured is then of the orbiting type. The resulting path (the solid line) on the Wilczyński plot is shown in Fig. 3.11. This theory thus does not give the full details of the Wilczyński plot but only the path followed by the ridge. The solid line gives a qualitative match to the data. It does not yield enough energy loss. These authors surmise that this may be caused by an additional energy loss because of an additional degree of freedom (deformation?) not taken into account by (3.4) and (3.5). Be that as it may, they effectively increase the energy loss by increasing the magnitude of the nuclear potential from the distance of closest approach outward, that is, during the final half of the collision [see Siwek–Wilczyński and Wilczyński (76)]. Under this assumption one obtains the dashed line, now giving an excellent fit. Using the same constants, scaling the nuclear radii as $A^{1/3}$, a good fit is obtained by Gross and Kalinowski for several cases.

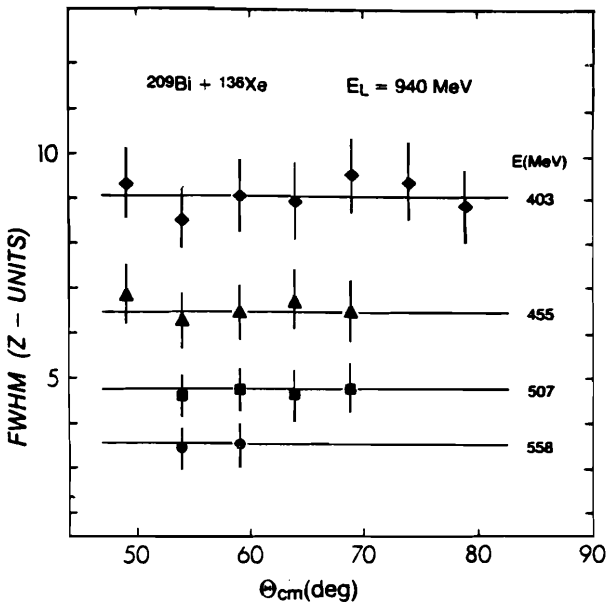


FIG. 3.14. The FWHM of Z distributions $d^3\sigma/d\Omega dE dZ$ for the indicated final kinetic energies is plotted versus center-of-mass reaction angle, for projectile-like fragments from the reaction $^{209}\text{Bi} + ^{136}\text{Xe}$ at $E_{\text{lab}} = 940$ MeV. The horizontal lines represent the fits to the angle-integrated Z distributions $d^2\sigma/dZ dE$. [From Wilcke, Birkelund, et al. (80).]

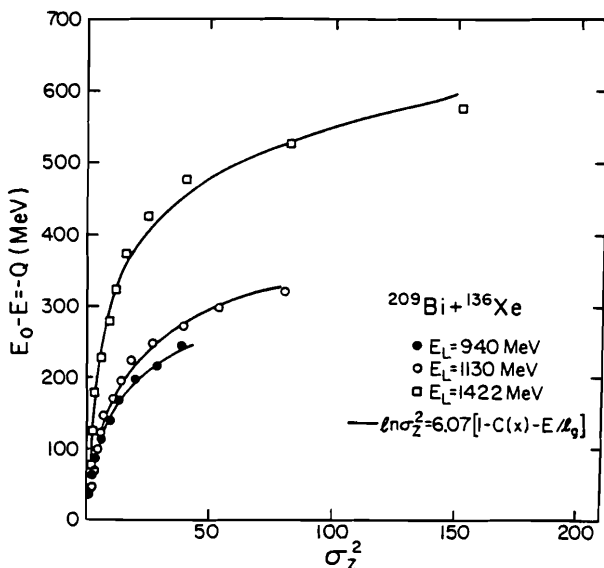


FIG. 3.15. Correlation between variance σ_z^2 of the Z distribution and total kinetic energy loss $E_{\text{loss}} = -Q$ for projectile-like fragments from the reaction $^{209}\text{Bi} + ^{136}\text{Xe}$ at three laboratory bombarding energies E_L . The curves drawn through the data points are fits. [From Huizenga and Birkelund (82).]

We learn from this discussion that particularly during the first phase of the reaction, kinetic energy loss increases as the interaction time increases. Therefore, one may use kinetic energy loss as a measure of interaction time. This permits the understanding of the direct experimental measures of various correlations. For example, we see from Fig. 3.12 the broadening of the angular distribution as the kinetic energy loss and therefore time increases. Similarly, one can expect a broadening of the distribution in atomic number Z of the nuclear reaction products as given in Fig. 3.13. The full width at half-maximum of the distributions on Z is independent of the reaction angle but does increase significantly as the kinetic energy loss increases, as shown by Fig. 3.14. These widths increase more rapidly with energy loss for increasing laboratory energy (see Fig. 3.15).

4. QUASI-ELASTIC SCATTERING[†]

We turn next to quasi-elastic scattering, which prevails for large values of the orbital angular momentum, l , according to Fig. 1.15. In this regime, the interaction time is relatively small, and direct processes that occur in the surface

[†]Arima and Kubono (84).

region dominate. These include inelastic excitation of each or both nuclei, as well as particle transfer. The processes involved are quite similar to that described for light ions in Chapter VII. Both are surface reactions but probe different parts of nuclear surface. There is one significant difference, in that heavy ions upon collision can exchange large amounts of mass, linear, and angular momentum. This exchange may be accomplished in one step, a cluster being transferred as a whole. Or in the other limit, the mass may be transferred sequentially, that is, one nucleon at a time. The sequential process involves a longer interaction time and is thus a precursor of deep inelastic scattering. Generally, these large mass and momentum transfers will excite multiparticle-hole states with high spin.

Conservation rules limit the allowable changes in linear and angular momentum of each nucleus. Brink (72), (77) has derived approximate classical conditions expressing these limitations. Brink assumes that the nucleus A_1 is moving with velocity v past the target nucleus A_2 . The cluster of mass M to be transferred from A_1 to A_2 has an internal energy in A_1 and in A_2 , equal to ε_1 and ε_2 , respectively. The interaction time is therefore given by $\hbar/(\varepsilon_1 + \frac{1}{2}Mv^2 - \varepsilon_2)$. The corresponding length is $\hbar v/(\varepsilon_1 + \frac{1}{2}Mv^2 - \varepsilon_2)$ and thus the momentum of the cluster leaving A_1 is

$$\hbar k_1 = \frac{1}{v}(\varepsilon_1 + \frac{1}{2}Mv^2 - \varepsilon_2)$$

The momentum of the cluster in A_2 can be obtained by symmetry, that is, by going to the coordinate system in which A_2 is moving and A_1 is at rest. Then the momentum of the cluster in A_2 is

$$\hbar k_2 = -\frac{1}{v}(\varepsilon_2 + \frac{1}{2}Mv^2 - \varepsilon_1)$$

The minus sign in front of the expression on the right-hand side is needed since we wish to compute the momentum of the cluster entering rather than leaving A_2 . The reaction proceeds most effectively if the angular momentum leaving A_1 matches the angular momentum of the cluster $\hbar\lambda_1$ at the surface of A_1 , that is,

$$\lambda_1 = k_1 R_1 = \frac{R_1}{\hbar v}(\frac{1}{2}Mv^2 + Q) \quad (4.1)$$

where

$$Q = \varepsilon_1 - \varepsilon_2$$

Similarly, the momentum and the angular momentum $\hbar\lambda_2$ at the surface of A_2 should agree:

$$\lambda_2 = -k_2 R_2 = \frac{R_2}{\hbar v}(\frac{1}{2}Mv^2 - Q). \quad (4.2)$$

The minus sign ($-k_2R_2$) takes account of the fact that the rotation in A_2 is opposite to that in A_1 .

Eliminating Q between (4.1) and (4.2) yields

$$\frac{\lambda_1}{R_1} + \frac{\lambda_2}{R_2} = \frac{Mv}{\hbar} \quad (4.3)$$

Taking the difference, one obtains

$$\lambda_1 - \lambda_2 = \frac{1}{\hbar v} (R_1 + R_2)Q + \frac{1}{2} (R_1 - R_2) \frac{Mv}{\hbar} \quad (4.4)$$

Equations (4.3) and (4.4) are the Brink (72, 77) kinematic conditions as usually quoted in the literature. Equation (4.3) expresses the conservation of linear momentum, while the conservation of angular momentum yields (4.4). These results hold for the transfer of neutral clusters. If the cluster is charged, one must include the change in the Coulomb energies in calculating $\varepsilon_1 - \varepsilon_2$. The net effect is to replace Q in (4.4) by Q_{eff} :

$$Q_{\text{eff}} \equiv Q - \frac{(Z_{1f}Z_{2f} - Z_{1i}Z_{2i})e^2}{d} \quad (4.5)$$

where Z_1 and Z_2 are the atomic numbers of the two nuclei, the subscripts i and f referring to their initial and final states, respectively, and d is the distance of closest approach. For other derivations, see Kahana and Baltz (77) and Ichimura, Takoda, Tamaya, and Nagatami (81); see also Bertsch and Schaeffer (77).

For a given initial spin λ_1 one can determine the optimum value, l_{opt} of $l \equiv |\lambda_1 - \lambda_2|$ and the optimum value of Q , Q_{opt} , from (4.3) and (4.4) or (4.1) and (4.2). The cross section is largest when l and Q equal or are close to l_{opt} and Q_{opt} . The range in l and Q around l_{opt} and Q_{opt} over which the cross section will be appreciable is referred to as the l window and the Q window. The width of these windows, more precisely the windows associated with (4.1) and (4.2), is given according to Brink (77) by $(\gamma_1 R_1)^{1/2}$ for (4.1) and $(\gamma_2 R_2)^{1/2}$ for (4.2), where $\gamma_i^2 = (2M/\hbar^2)|\varepsilon_i|$. Thus the larger the separation energies $|\varepsilon_i|$, the wider the l window corresponding to a more localized interaction region, while a narrow l window corresponds to a less localized interaction region.

The angular distribution of the reaction products reflect the width of the l window. When the l window is large, the angular range in which the reaction products are found is characteristically narrow. The angular distribution is then "bell shaped" around the grazing angle, as illustrated by Fig. 4.1.

On the other hand, when the l window is narrow, the angular distribution shows a diffraction pattern as illustrated by Fig. 4.2. As the figure shows, the diffraction distribution appears as the energy of the projectile is raised. This

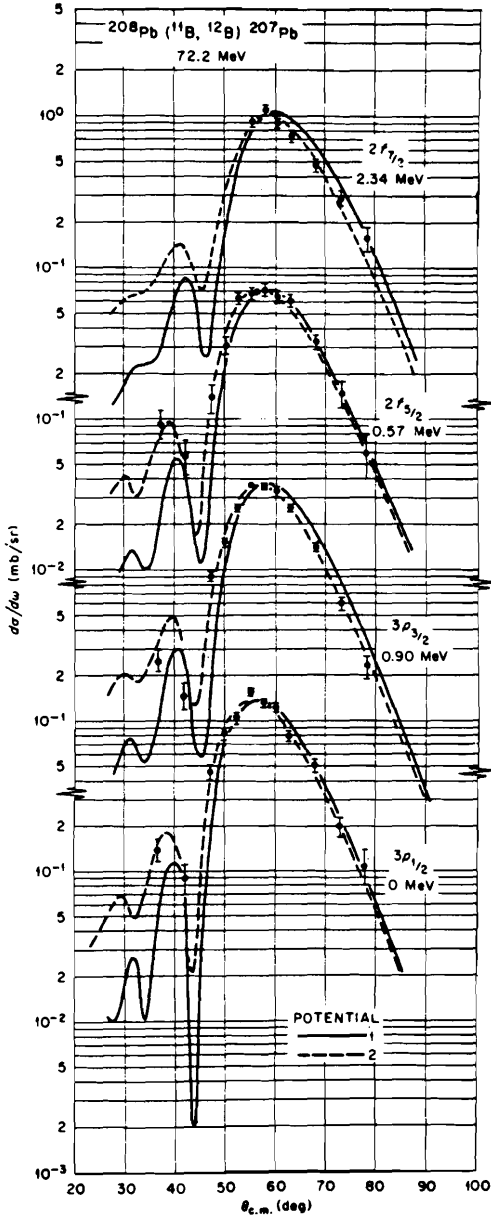


FIG. 4.1. Typical bell-shaped distributions for transfer reactions with heavy ions at energies close to the Coulomb barrier. The curves are from DWA calculations with two different optical potentials. The transitions are labeled by the hole state excited in ^{207}Pb . [From Ford, Toch, et al. (74).]

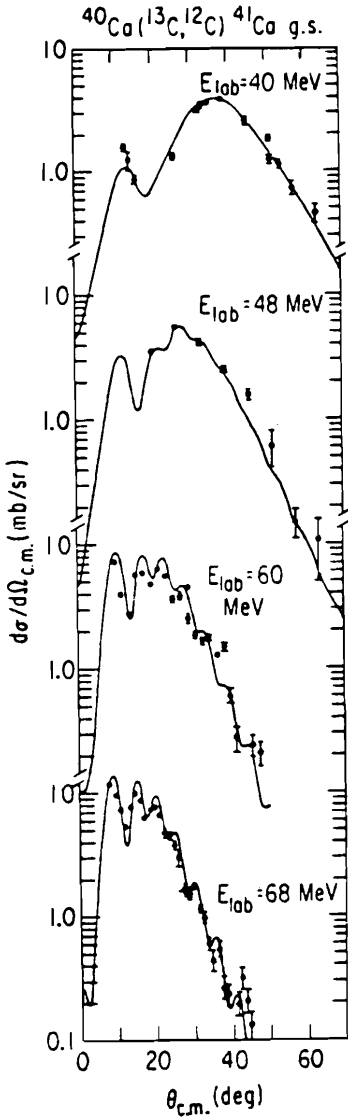


FIG. 4.2. Example of the evolution from a bell-shaped distribution to the appearance of diffraction structure as the energy is raised. [From Kahana and Baltz (77).]

behavior is expected since the penetration of the projectile increases with increasing energy so that the spatial region over which the interaction occurs increases.

In the case of a multiparticle transfer, M will be generally be large and the final state ε_2 will be highly excited so that Q will be negative. It thus becomes favorable for λ_1 to be small and λ_2 to be large according to (4.1) and (4.2). Transfer of large mass clusters will therefore predominately populate high-spin states.

In analogy with the use of stripping and pickup reactions to gain information with regard to single-particle states, one might hope to use cluster transfer reactions to explore the state of clusters within nuclei; or stated more precisely, the nature of n -particle correlations, where n is the number of particles in the cluster. Such a hope is not universally realized, since the cluster transfer must be observed in the presence of competing (and interfering!) mechanisms such as sequential transfer reactions, in which the n particles are transferred one by one. This is demonstrated by Fig. 4.3, where one can compare the importance of the single-step transfer of the two neutrons (DWA) with their transfer one neutron at a time.

However, when there is a good match between the correlations that exist in the final state of the residual nucleus and those of the transferred cluster, the spectroscopic factor and the cross section will be relatively large. This is the case for the (t, p) reaction on the tin isotopes. The cluster transferred consists of two neutrons in the 1S_0 state, the dominant component of the two-neutron amplitude in ^3H . But this is exactly the nature of the neutron correlations in the superconducting ground state of the tin isotopes enforced in that case by the pairing interaction. These form a superfluid band analogous to the rotational band in deformed nuclei. The ground state-to-ground state transition therefore has a favorable probability. [See Broglia, Hansen, and Riedel (73) for a review of this process.] It is found [Scott, Harvey, et al. (77)] that in that case the cross section for cluster transfer is more than an order of magnitude larger than the sequential transfer. A similar phenomenon may be expected for the appropriate reaction with heavy ions. One example is $^{120}\text{Sn}(^{18}\text{O}, ^{16}\text{O})\text{Sn}$, illustrated in Fig. 4.4.

The experimental and theoretical understanding of one-to-many particle transfers in heavy-ion reactions is summarized by Arima and Kubono (84), to which the reader is referred. For this volume it will suffice to present some salient features. As in the case of light-ion-induced reactions, the angular distributions, particularly the position of the first peak, depends on the orbital angular momentum, l , transferred. This is illustrated in Fig. 4.5 for the case of an α -cluster transfer, $^{54}\text{Fe}(^6\text{Li}, d)^{58}\text{Ni}$ and $^{58}\text{Ni}(^6\text{Li}, d)^{62}\text{Zn}$. In contrast to the (d, p) reaction, the (p, α) and (α, p) reactions are markedly sensitive to the total angular momentum transferred (see Fig. 4.6). The important effect of the finite size of the projectile is illustrated by Fig. 4.7. For a thorough study of the finite-size effect in the (t, p) reaction, see Bayman (70, 71). In that case Bayman shows that a substantial increase, often more than an order of magnitude, of the absolute value of the cross section results. In his case he found that the finite range effects do not change the angular distributions from that obtained from zero-range DWA. This conclusion is important because generally the zero-range DWA yields a cross section that is far smaller than the experimental one. There are other effects that go in the same direction. Because the theoretical results depend on the values of the wave functions involved in the surface region, there is a great sensitivity to the accuracy of these wave functions in that narrow region. The harmonic oscillator wave functions often used are grossly inadequate

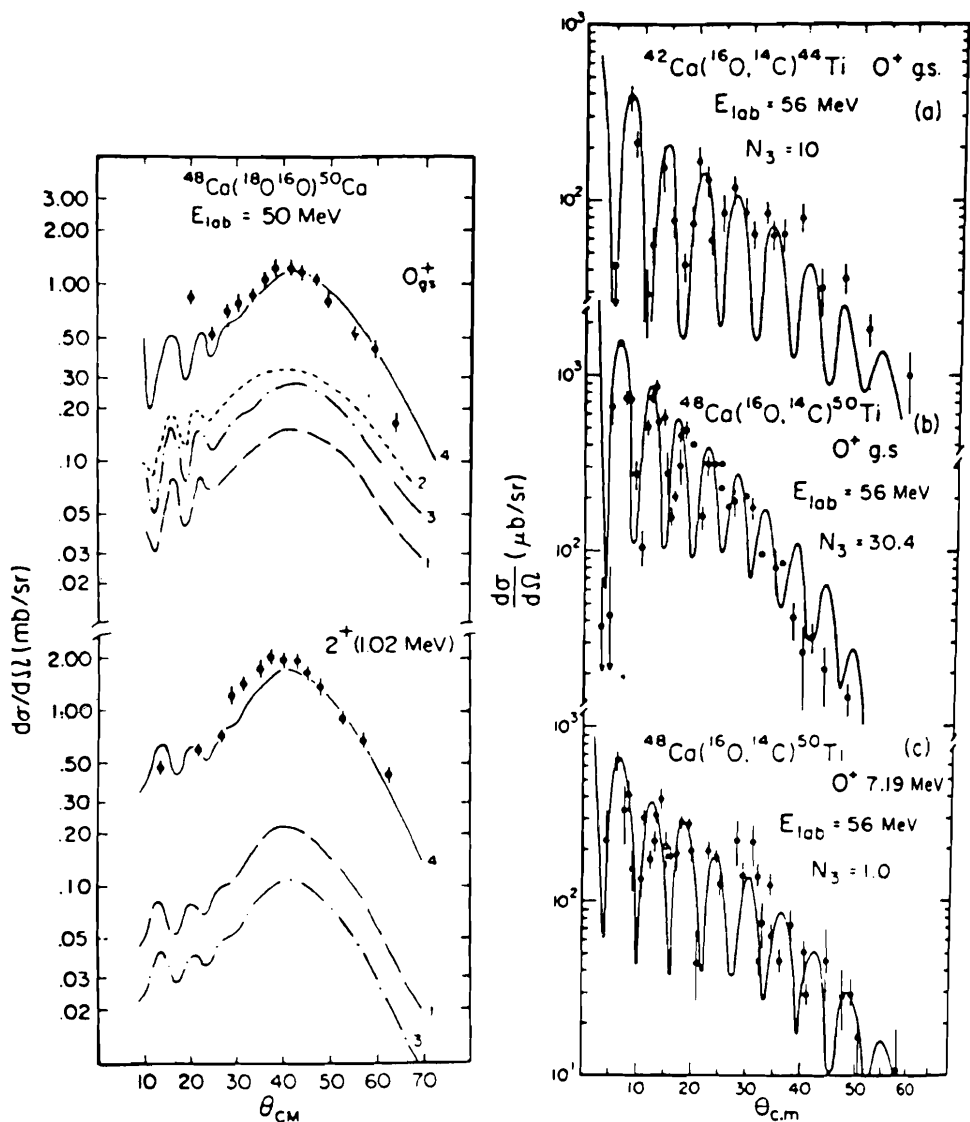


FIG. 4.3. Analysis of two-nucleon transfer reactions, including simultaneous and sequential transfer and using realistic overlap functions in exact finite-range DWA calculations. (a) Two-neutron transfer. Curves 1 and 2 are for simultaneous transfer using simple and realistic nuclear wave functions, respectively, while curve 3 is the sequential transfer. Curve 4 is for the coherent sum of the two processes. The theoretical curves have not been renormalized to fit the data. (b) Two-proton transfer. Also calculated with realistic wave functions and including simultaneous plus sequential transfer. Although the angular distributions are the same as the measured ones, only the magnitude of the transition to the excited ^{50}Ti state is in agreement. The calculated cross sections for the ground-state transitions are too small by factors of $N_3 = 10$ (^{44}Ti) and 30.4 (^{50}Ti). [From Feng, Udagawa, et al, (76).]

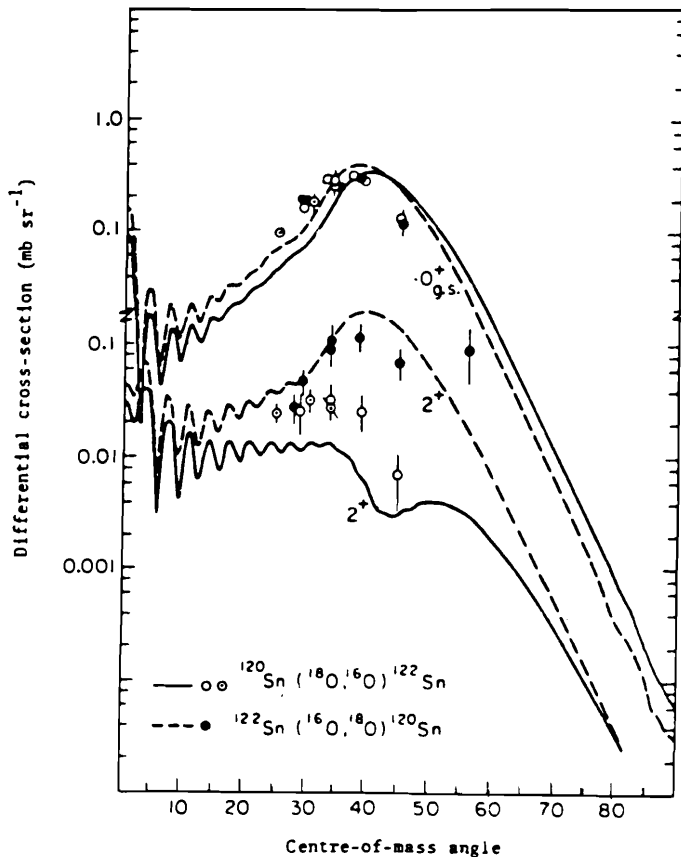


FIG. 4.4. Contrasting the direct-indirect interferences for pickup and stripping of two neutrons in a heavy-ion reaction at about 100 MeV, exciting the 2^+ vibrational states of the residual nuclei. Except for a small change in energy, the ground-state transitions are the inverses of each other, but the 2^+ states are in different nuclei. [From Scott, Harvey, et al. (75).]

since their decrease in the surface region is Gaussian rather than exponential. To obtain better agreement, it then becomes necessary to take linear combinations of many harmonic oscillator wave functions, as Tonzuka and Arima (79) found. The inadequacy of these wave functions is more severe in the case of heavy-ion compared to light-ion projectiles because the cross section is more sensitive to the wave functions for *larger* values of the radial variable.

The examples discussed above consider the excitation of discrete levels close to and including the ground state of the residual nucleus. The excitation levels in the continuum has also been observed, for example, $^{40}\text{Ca}(^{20}\text{Ne}, ^{16}\text{O})^{44}\text{Ti}$ [Frölich, Shimoda, et al. (79)], in which the ^{16}O spectrum is observed. Interestingly, the direct α -cluster transfer process is generally accompanied by

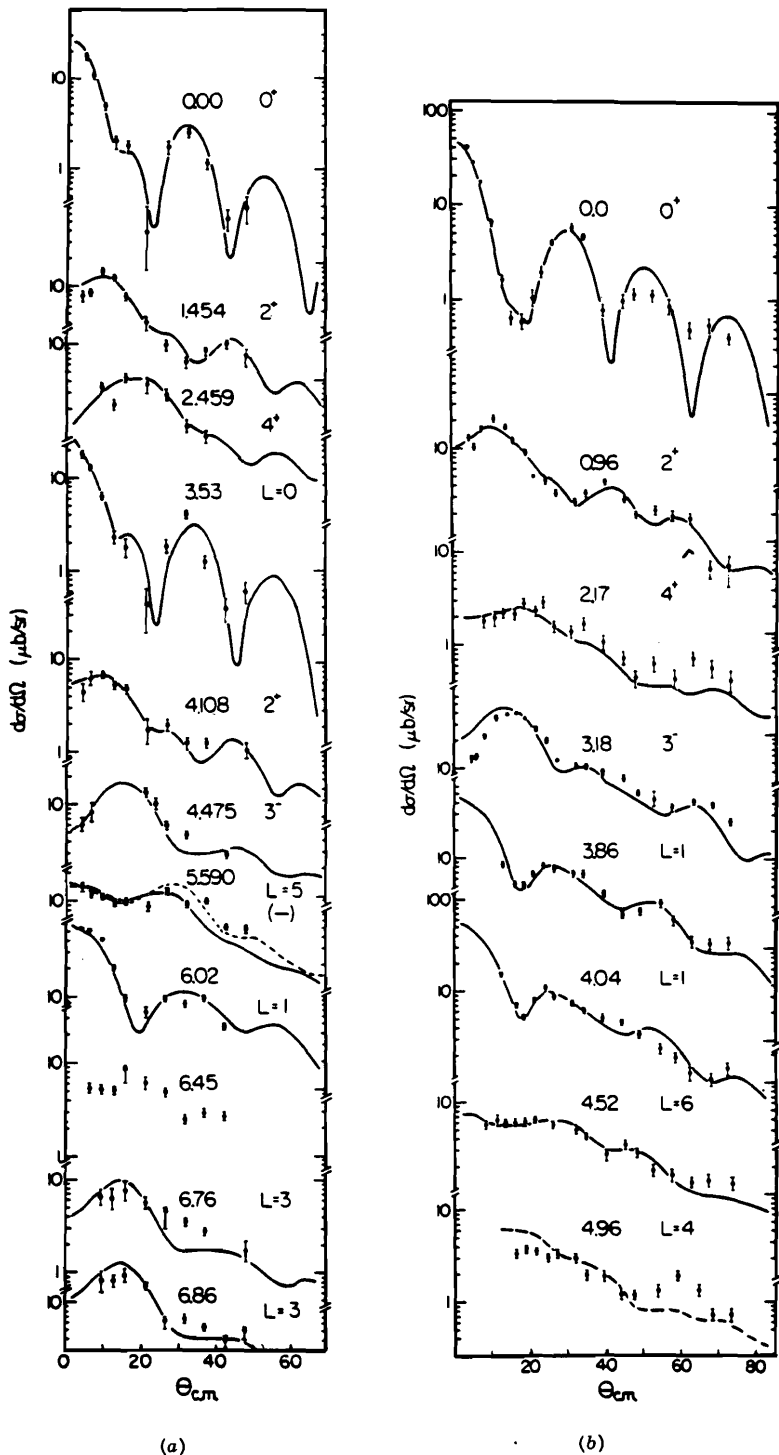


FIG. 4.5. Angular distributions of (a) the $^{54}\text{Fe}(^6\text{Li}, d)^{58}\text{Ni}$ reaction and (b) the $^{58}\text{Ni}(^6\text{Li}, d)^{62}\text{Zn}$ reaction of several transferred angular momenta at 28 MeV. The lines are the DWA calculations. [From Fulbright, Strobusch, et al. (75).]

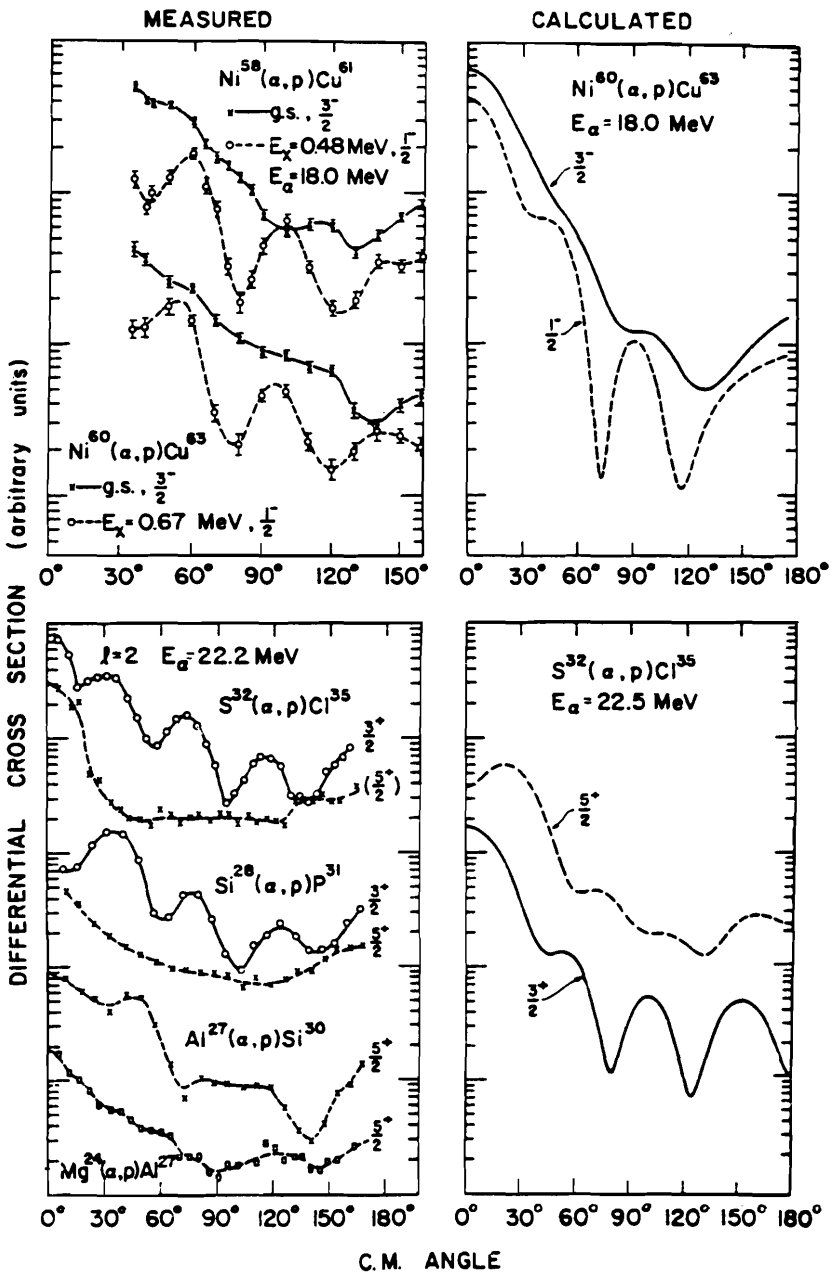


FIG. 4.6. The j -dependence of the (α, p) reactions in some l -transfer processes. The left-hand side is the experimental data and the right-hand side is the DWBA calculations with spin-orbit potentials. [From Yamazaki, Kondo, and Yamato (63); Lee, Marinov, et al. (65).]

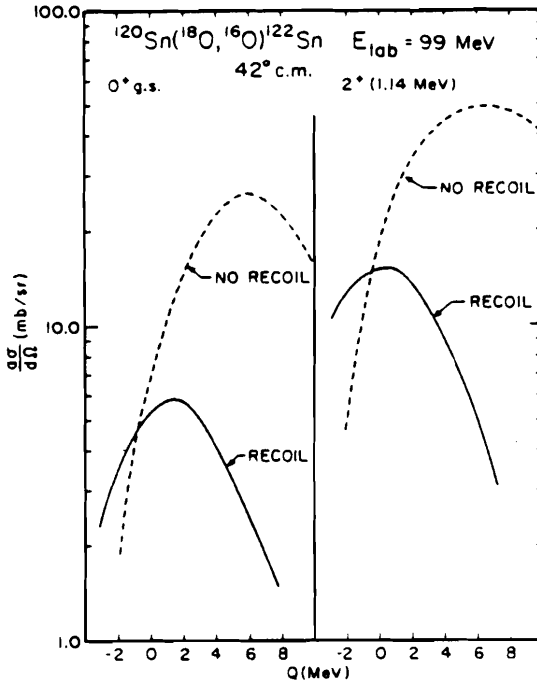


FIG. 4.7. Distortion of the Q window for a two-nucleon transfer when the no-recoil approximation is made. Calculated peak cross sections at 42° for $l=0$ and 2 transactions as a function of Q . [From Feng, Udagawa, et al. (76).]

the fragmentation of the incident projectile ^{20}Ne . The reader should recall that essentially the same process is responsible for incomplete fusion. The excitation of continuum levels involves large energy transfers from the incident kinetic energy to internal energy. In fact, one can regard the quasi-elastic domain as one in which the elementary transfer processes, which are in part responsible for fusion and deep inelastic scattering, are revealed. Because of the long interaction time for the latter reaction types, it is possible to repeat the elementary transfers several times, leading one way or another to large mass and energy transfers [see Rehm, vanden Berg, et al. (78)]. Truly massive transfers are often involved, but sequential transfers one particle or cluster at a time are equally important. At energies near the Coulomb barrier, the single neutron transfer is found to be a major part of the reaction cross section. For example, in the collision of ^{58}Ni with ^{58}Ni and ^{64}Ni and $E_{\text{cm}} \sim 100$ MeV, one finds [Rehm, Wolfs, et al. (85)] that the cross section of one and two neutron transfers is one-third of the reaction cross section and is larger than the fusion cross section.

The DWA approximation, in this heavy-ion context, does not differ conceptually from that discussed in Chapter VI on the (d, p) and (p, d) reaction.

Of course, it is far more complicated both geometrically and numerically, so that the use of modern computers is essential. Improvements on the DWA can be obtained with simple generations of the methods described in Chapter VI. The inclusion of the effects of the Pauli principle, of overlap and the reduction to coupled channels, are accomplished by exploiting the properties of a generalized K matrix. That matrix, described by (VI. 2.17), has a rank equal to the number of channels explicitly included. In the (d, p) case it was two, corresponding to the deuteron and proton channels. In the case of heavy ions one may need to include a greater number of exit channels. This is certainly the case when sequential transfer is important. Once the K matrix is determined, the next step is to determine its eigenvalues, especially those whose value is 1. One must eliminate the corresponding eigenstates, by projection or by the use of the orthogonality condition method of Saito. In any event, one then obtains the coupled-channel equations, which include rigorously the Pauli principle and overlap effects. For more details, see the paper by H. Horiuchi (77).

An alternative approach makes the semiclassical time-dependent approximation for the motion of the heavy ions. At each position in the orbit there is a transition probability that a reaction will occur. This is calculated quantum mechanically. This method was used very successfully by Alder, Bohr, et al. (56) in calculating the electromagnetic excitation of nuclei by charged particles. Its adaptation to the nuclear excitation in heavy-ion collisions has been developed by Broglia and Winther (72) and Broglia, Landowne, et al. (74). A similar procedure was developed by Bertsch and Schaeffer (77).

5. HEAVY-ION RESONANCES[†]

Resonances in the collision of heavy ions were first observed by Almqvist, Bromley and Kuehner, and (60). The heavy ions involved were ^{12}C and the center-of-mass energy was about 6 MeV, very close to the Coulomb barrier energy. The observations included scattering and reaction channels. Since that time, further resonances have been discovered in the $^{12}\text{C} + ^{12}\text{C}$ system, as well as in the $^{12}\text{C} + ^{16}\text{O}$ system, and more recently in the $^{28}\text{Si} + ^{28}\text{Si}$ system [Betts et al. (81)]. However, no such structure was observed for $^{40}\text{Ca} + ^{40}\text{Ca}$. Some examples are given in the following figures. Figure 5.1 gives the total γ -radiation yields (divided by the Coulomb transmission factor, which removes most of the energy dependence). Note the large number of peaks and the fact that spin and parity have been assigned to many. Figure 5.2 shows resonances in the $^{12}\text{C} + ^{16}\text{O}$ system, which appear in the inelastic scattering. Another example is provided by the radiative capture of ^{12}C by ^{16}O shown in Fig. 5.3. In Fig. 5.4 the 90° elastic $^{28}\text{Si} + ^{28}\text{Si}$ scattering is shown, while in Fig. 5.5 a high-resolution study of the scattering is recorded. The data exhibit two kinds of structure. There are

[†]Erb and Bromley (84).

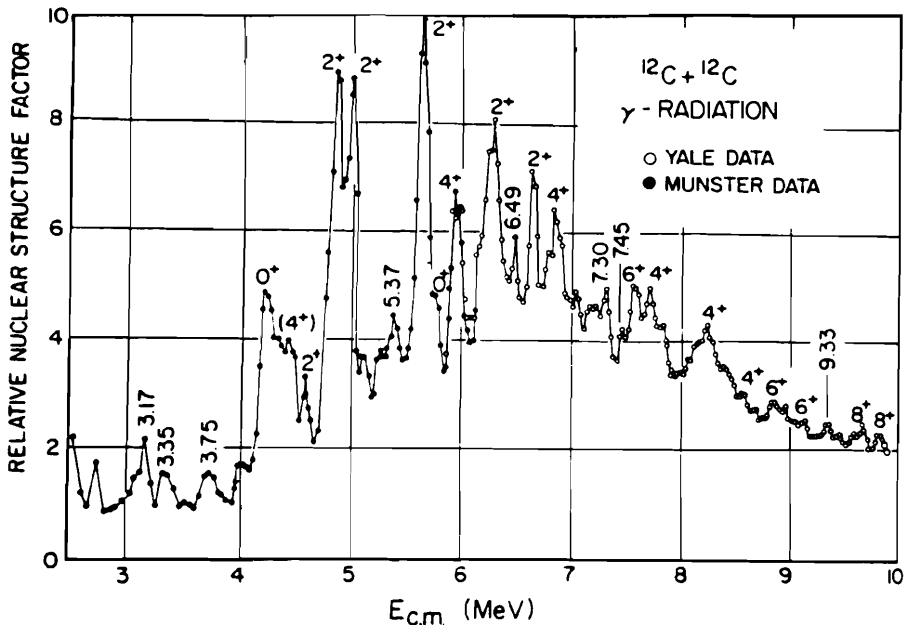


FIG. 5.1. Nuclear structure factors derived from the total γ -radiation yields of the $^{12}\text{C} + ^{12}\text{C}$ interaction. The nuclear structure factor is defined by

$$T_L = \frac{E\sigma(E)}{\sum_{L=0}^{10} (2L+1)T_L} = \frac{KR}{F_L^2(KR) + G_L^2(KR)}$$

where $R = 1.4(12^{1/3} + 12^{1/3})$ and F_L and G_L are the regular and irregular Coulomb wave functions, respectively. [From Erb and Bromley (84).]

broad envelopes with a width on the order of 150 keV and an energy separation of the order of a few hundred keV.

Most systems do not resonate. Or stated more carefully, the resonance amplitudes, if they exist, are not sufficiently strong to be observable. As an example, see Fig. 5.6, giving the total γ -radiation in the neighborhood of the Coulomb barrier of $^{16}\text{O} + ^{16}\text{O}$. One sees very little structure, which hardly compares with violent fluctuations, which appear in Fig. 5.1 for $^{12}\text{C} + ^{12}\text{C}$.

In analyzing the experimental data, two problems must be solved. In one, the issue is distinguishing the resonance peaks from the Ericson random fluctuations. In the other, how can the spin and parity of the resonances be determined? Turning to the first of these, one can obtain an estimate of the magnitude of the Ericson fluctuations using the statistical theory of nuclear reactions. If the peak under study has a width much larger than predicted by the statistical theory and/or if its magnitude is much greater, it is probably a resonance. Another indication is obtained by comparing reactions involving

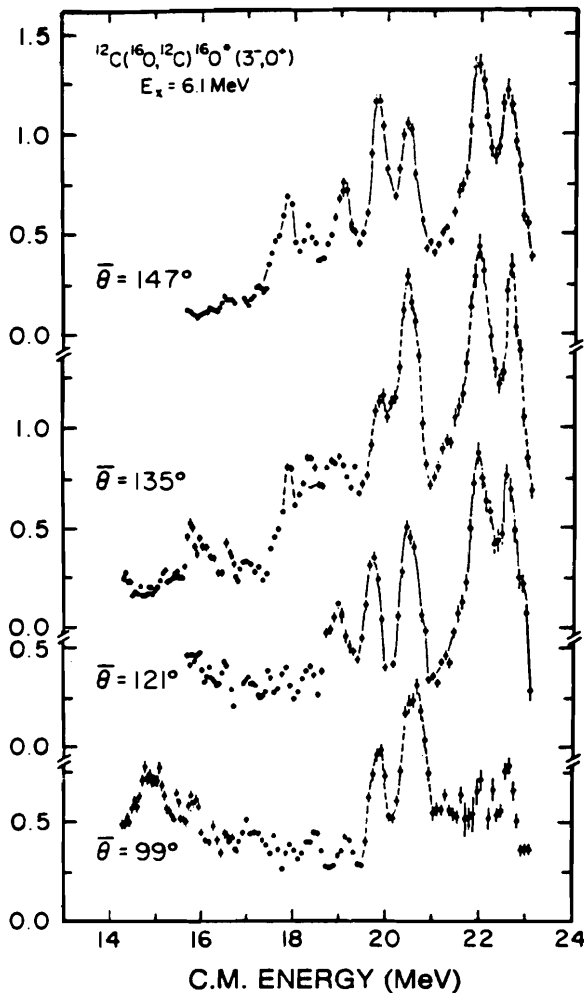


FIG. 5.2. $^{16}\text{O}(3^-)$ in elastic yields. [From Malmin, Harris, and Paul (78).]

the same compound nucleus. If peaks appear in one channel and not in the other, one is certainly not dealing with Ericson fluctuations. As an example, see the comparison of $^{12}\text{C}(^{16}\text{O}, \alpha)^{24}\text{Mg}$ and $^{14}\text{N}(^{14}\text{N}, \alpha)^{24}\text{Mg}$ in Fig. 5.7. The cross section for the first reaction has structure, the second does not. Second, if one sums the cross sections for differing channels, the statistical fluctuations will tend to average out so that peaks in the summed cross section are probably resonances. Finally, if one can establish a correlation among the peaks in the various channel cross sections, a resonance of the system is indicated. One must be careful since the energy of a peak may shift from one channel to the next by the order of a width because of interference with a nonresonant amplitude.

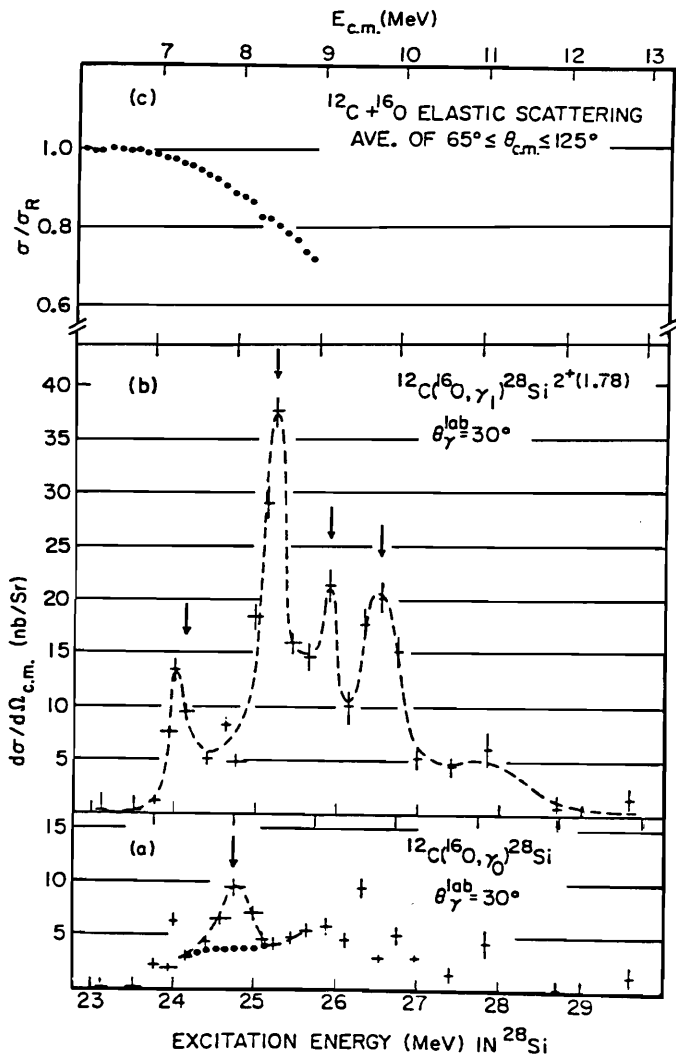


FIG. 5.3. Excitation functions for the radiative capture of ^{12}C by ^{16}O . The elastic scattering data are from Spinka and Winkler (74). The dashed lines are drawn to guide the eye. [From Collins and Sandorfi (82).]

An example of this analysis is shown in Figs. 5.8 and 5.9. In Fig. 5.8 the cross sections to different levels of ^{20}Ne formed by the reaction $^{12}\text{C}(^{12}\text{C}, \alpha)^{20}\text{Ne}$ are plotted together with their sum. The shown shows several peaks. The anomalies at 7.71, 9.84, and 10.59 MeV are studied [Erb et al. (77)]. The widths of the 7.71- and 9.84-MeV peaks are one to two orders of magnitude greater than that given by a Hauser-Feshbach calculation. The 10.59-MeV peak turns out

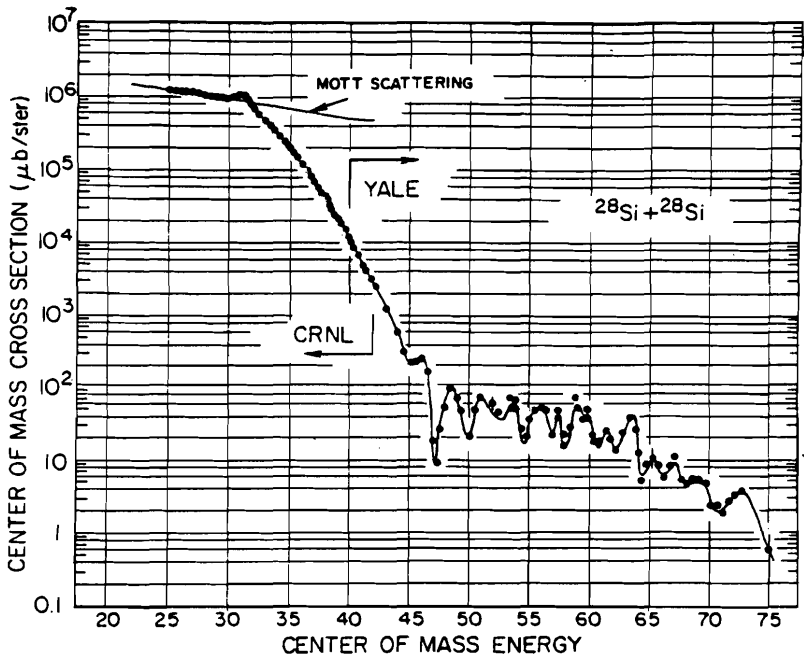


FIG. 5.4. Excitation function for $^{28}\text{Si} + ^{28}\text{Si}$ elastic scattering at $\theta_{\text{cm}} = 90^\circ$. [From Erb and Bromley (84).]

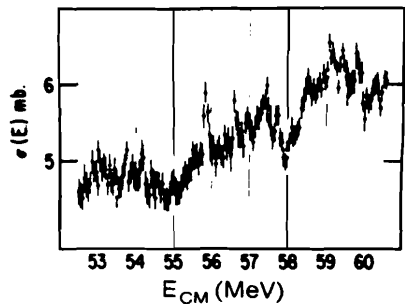


FIG. 5.5. High-resolution cross-section of the summed elastic and inelastic excitation function for the $^{28}\text{Si} + ^{28}\text{Si}$ system. [From Betts, Diczno, and Peterson (81).]

not to have an unusual strength, so that it is probably a fluctuation and not a resonance. Figure 5.9 gives the angular distribution of the α -particles for the 7.71- and 9.84-MeV peaks. We see that these beautifully follow $|P_4(\cos \vartheta)|^2$ and $|P_8(\cos \vartheta)|^2$ distributions suggesting the spin of 4 in the 7.71-MeV resonance and 8 for the 9.84 resonance.

This description provides one method for determining the spin of a resonance. It is by itself not enough but should be augmented by a study of the energy dependence of the angular distribution. This is illustrated by Fig. 5.10, where

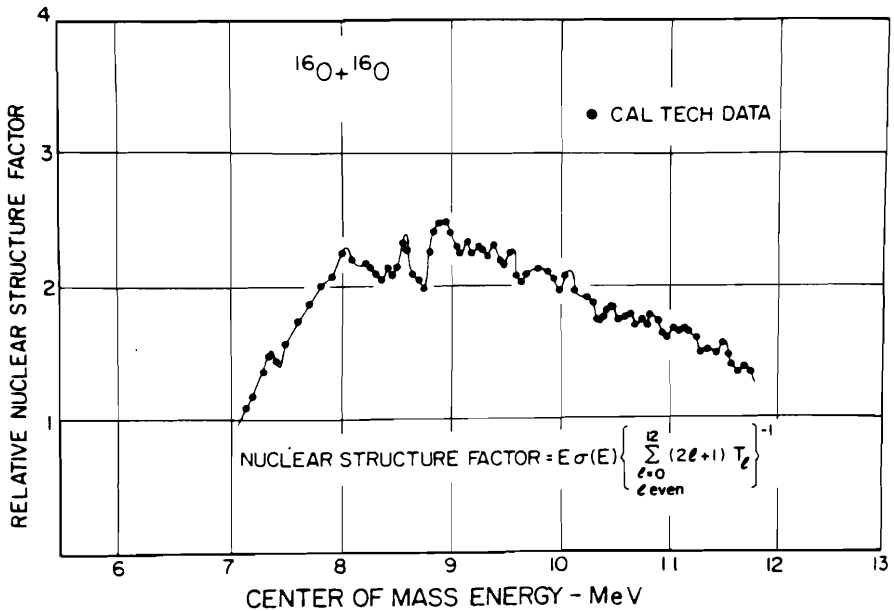


FIG. 5.6. Nuclear structure factors for the $^{16}\text{O} + ^{16}\text{O}$ interaction (see Fig. 5.1). [From Erb and Bromley (84).]

one sees the comparatively featureless angular distributions interrupted by strong oscillatory behavior at, for example, energies 7.71 and 9.84 MeV.

Another general procedure is to attempt a phase shift analysis of the elastic scattering. As long as the number of nuclear partial waves is low, this is a practical method. A closely related method involves fitting the energy-averaged cross section by an optical model. To obtain the intermediate structure, one adds Breit-Wigner contributions to the optical model phase shifts. An example of the first of these two methods is given in Fig. 5.11. Note that the magnitude of the S matrix, η_L , has deep minima at the resonant energies of 6.65 MeV in the $L = 2$ partial wave and 6.85 MeV in the $L = 4$ partial wave, thus identifying the spin of these resonances. Similar analyses have been made at higher energies by Cosman et al. (82). From the Breit-Wigner fit one can get an estimate of the ratio Γ_{el}/Γ . For the $L = 2$ case this turns out to be 0.29, while for the $L = 4$ case it is 0.09. Both values are much larger than the statistical estimates of these partial width ratios.

These analyses provide a list of isolated resonant states. Overlapping states have been discussed, but disentangling these has not proved practical, especially for states of high spin. Our first question is: What are the nature of these resonant states? Our second is: What is the mechanism that produces these resonances? And as a corollary: What conditions need to be met?

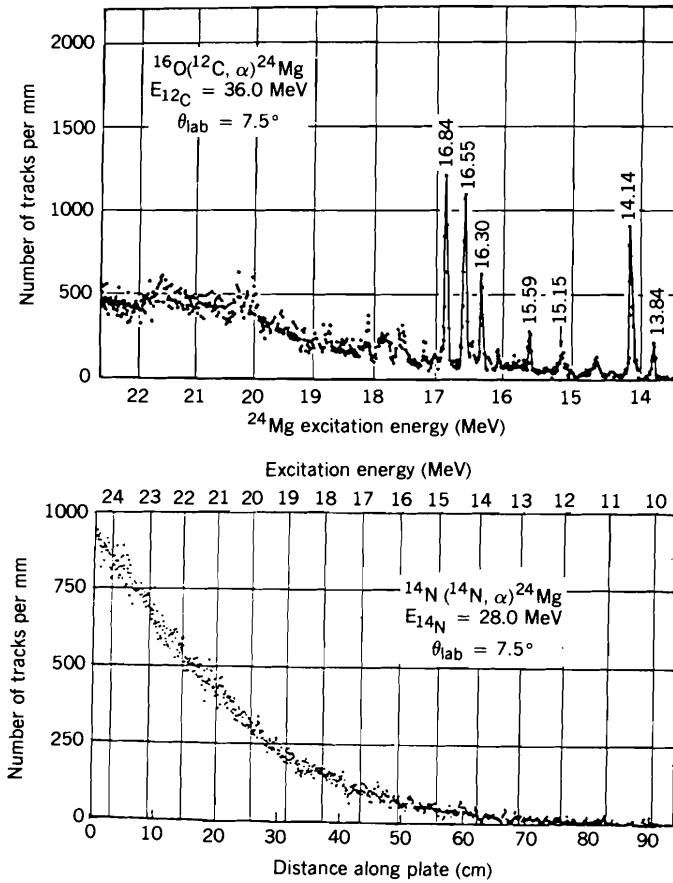


FIG. 5.7. Alpha particle spectra from the $^{16}\text{O}(^{12}\text{C}, \alpha)^{24}\text{Mg}$ and $^{14}\text{N}(^{14}\text{N}, \alpha)^{24}\text{Mg}$ reactions. [From Bromley (78).]

With regard to the first question, it is clear that these states are doorway states. Their widths ($\sim 100 \text{ keV}$) are much smaller than the width of structures (e.g., shape resonances) generated by an optical model on the order of 2.5 MeV . On the other hand, these widths are too large to be compound nuclear widths. Indeed, if very high resolution measurements are made [Bromley (78)], one finds the Ericson fluctuation structure (see also Fig. 5.5).

We can refer to Section III.4 for a discussion of doorway states. The expression for the transition amplitude for a reaction proceeding through an isolated doorway resonance, (III.4.16), is appropriate here. It is

$$\langle \mathcal{F}_{fi} \rangle = \mathcal{F}_{fi}^P + \frac{\langle \chi_f^{(-)} | H_{PD} \psi_d \rangle \langle \psi_d | H_{DF} \chi_i^{(+)} \rangle}{E - E_d + i/2(\Gamma_d^\uparrow + \Gamma_d^\downarrow)} \quad (\text{III.4.16})$$

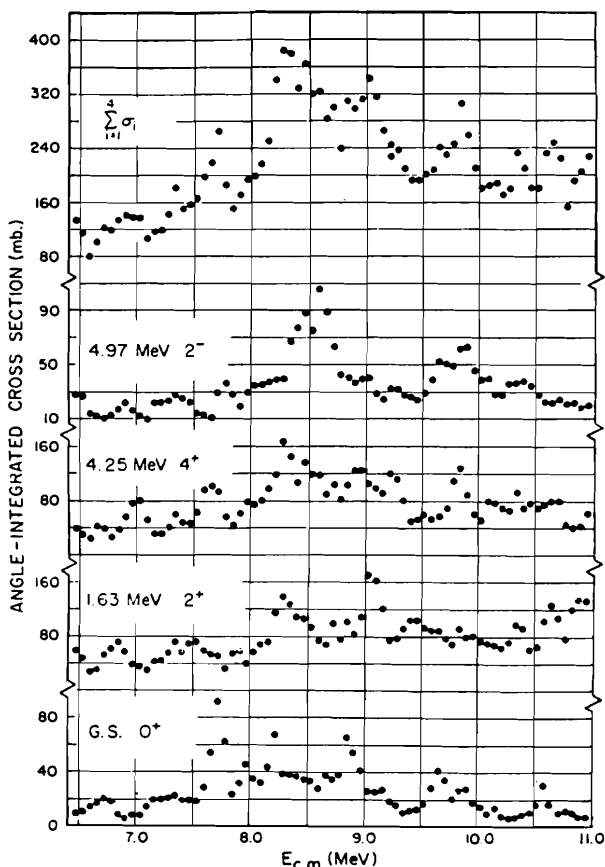


FIG. 5.8. Angle integrated cross sections as functions of the energy for the $^{12}\text{C}(^{12}\text{C}, \alpha)^{20}\text{Ne}^*$ reaction populating low-lying levels of ^{20}Ne . [From Erb et al. (77).]

The average is over the fine structure. H_{DP} and H_{PD} are the operators connecting the entrance channel or exit channel wave functions $\chi_i^{(+)}$ and $\chi_f^{(-)}$ with the doorway wave function ψ_d . \mathcal{T}^P is the transition for the prompt, nonresonant amplitude, while Γ_d^\dagger is the escape width:

$$\Gamma_d^\dagger = 2\pi \sum_\gamma |\langle \chi_\gamma^{(-)} | H_{PD} \psi_D \rangle|^2$$

which gives the probability that the doorway state will decay into an exit channel, $\chi_\gamma^{(-)}$. The spreading width, Γ_d^\downarrow , gives the probability that the doorway state will decay into the more complex states. For elastic scattering and a particular partial wave, the S matrix $\langle S_{e1} \rangle$ can be obtained directly from

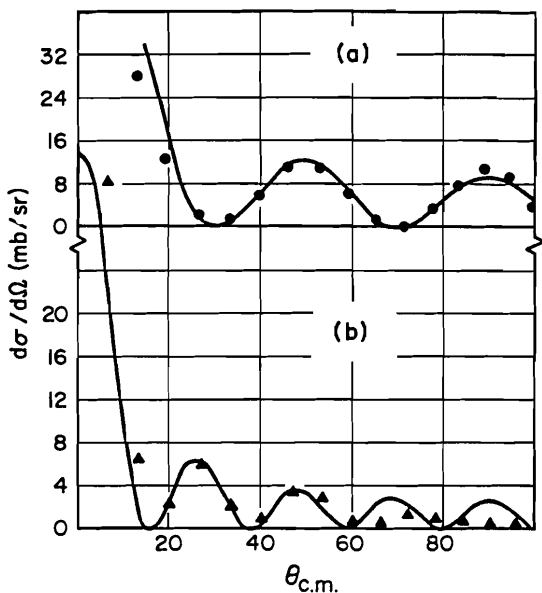


FIG. 5.9. The $^{12}\text{C}(^{12}\text{C}, \alpha)^{20}\text{Ne}$ angular distribution compared to the Legendre functions $|P_L(\cos\theta)|^2$, not normalized: (a) $E_{cm} = 7.71$ MeV ($L = 4$); (b) $E_{cm} = 9.84$ MeV ($L = 8$). [From Erb et al. (77).]

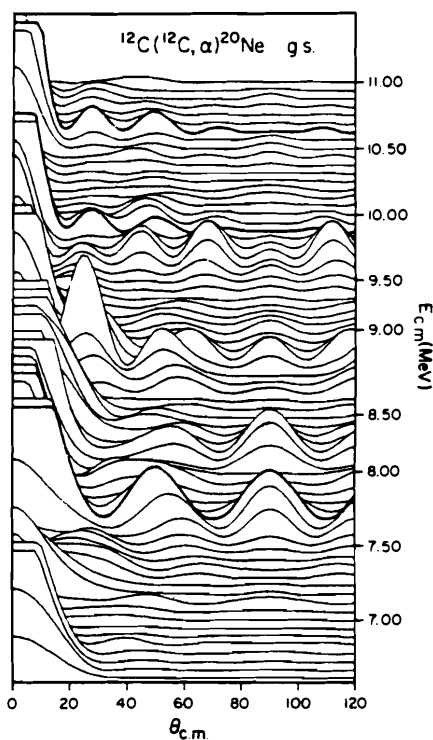


FIG. 5.10. Evolution of the ^{20}Ne ground-state angular distributions as a function of bombarding energy. The heavy curves signify angular distributions at energies of maxima in the total yields that are particularly well fitted by pure $|P_L(\cos\theta)|^2$ shapes. [From Erb and Bromley (84).]

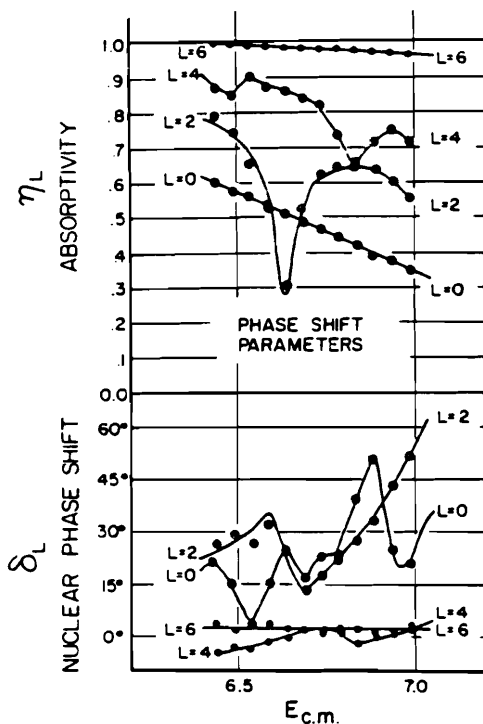


FIG. 5.11. Phase-shift parameters $S = \eta_L e^{i\delta_L}$ deduced from the phase-shift analysis of $^{12}\text{C} + ^{12}\text{C}$ elastic scattering. [From Korotky, Erb, Willett, and Bromley (79).]

(III.4.16). One obtains

$$\langle S_{el} \rangle = e^{2i\delta} \frac{(E - E_d) + \frac{1}{2}i(\Gamma_d^{\downarrow} - \Gamma_d^{\uparrow})}{(E - E_d) + \frac{1}{2}i(\Gamma_d^{\downarrow} + \Gamma_d^{\uparrow})} \quad (\text{III.4.18})$$

where δ is the phase associated with the prompt (potential) scattering. Note that the magnitude of $\langle S_{el} \rangle$ squared is

$$e^{-4\eta} = \frac{(E - E_d)^2 + \frac{1}{4}(\Gamma_d^{\downarrow} - \Gamma_d^{\uparrow})^2}{(E - E_d)^2 + \frac{1}{4}(\Gamma_d^{\downarrow} + \Gamma_d^{\uparrow})^2}$$

We see that this magnitude has a minimum at $E = E_d$ as observed (see Fig. 5.11).

We turn now to the second question, the nature of the doorway states and the mechanism that generates them. In the $^{12}\text{C} + ^{12}\text{C}$ case, it is possible to establish a qualitative understanding. Toward that end, examine Fig. 5.12, where we have plotted the energy of the observed resonance versus $J(J + 1)$ [Feshbach (76, 77)]. Look also at a plot of the excitation energy centroids of the levels of

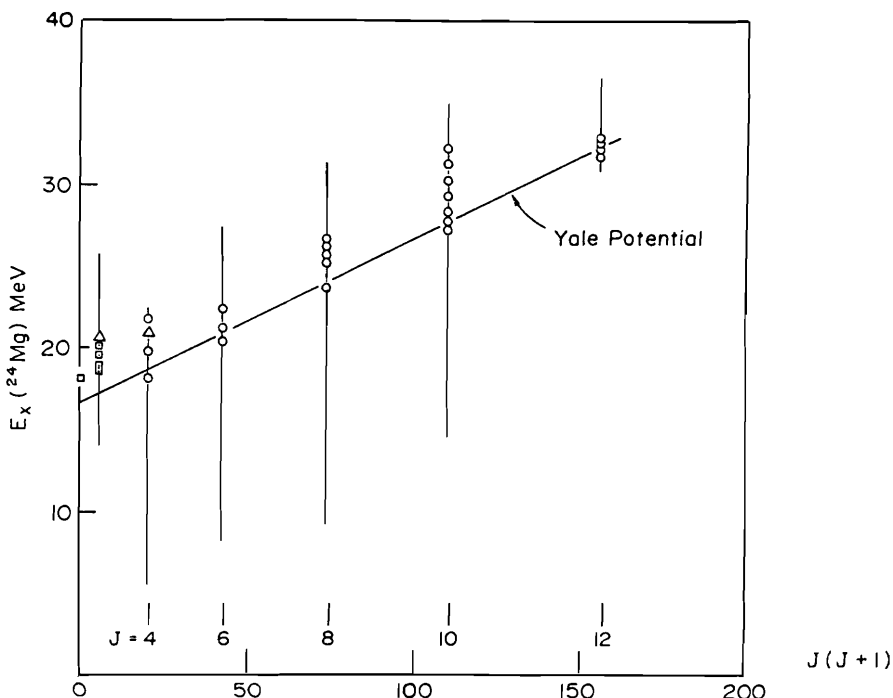


FIG. 5.12. Excitation energy of $^{12}\text{C} + ^{12}\text{C}$ resonances as a function of $J(J+1)$, $J =$ spin of the resonance. The line marked "Yale potential" is the locus of the values of J and E_x corresponding to grazing [Feshbach (77, 78).]

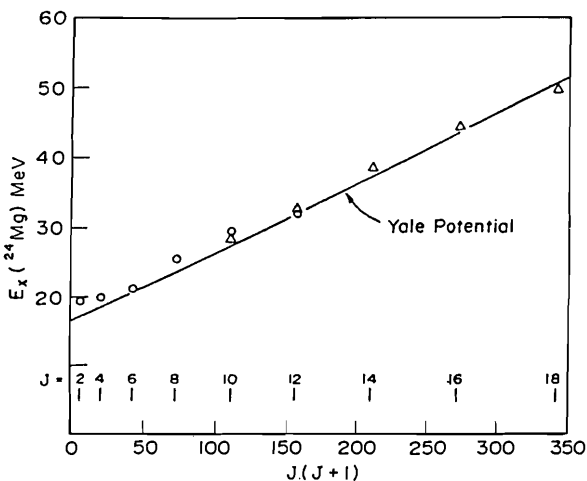


FIG. 5.13. Average energy of levels in ^{24}Mg excited in the $^{12}\text{C} + ^{12}\text{C}$ versus $J(J+1)$. [From Feshbach (78).]

a given J given in Fig. 5.13. The line labeled the “Yale potential” is obtained by Arima et al. (72) by determining the values of the orbital angular momentum L and energies at which the potential devised by Reilly et al. (73) to fit the elastic $^{12}\text{C} + ^{12}\text{C}$ scattering generates a pole in the S matrix. These values of L will not differ especially from the grazing L . That potential is a central potential composed of Woods–Saxon forms for both the real and imaginary parts (see Chapter V). The parameters are $V = 14$ MeV, $R = 6.18$ fm, $a = 0.35$ fm, $W = 0.4 + 0.1E$, $R_I = 6.41$ fm, and $a_I = 0.35$ fm. The shallow depth, and especially the weak imaginary terms, are required to obtain the rather large oscillations of the observed angular distributions (see Fig. 5.14).

The experimental fact that the centroids are a linear function of $J(J + 1)$ is noteworthy (see Fig. 5.13). The fact that this straight line follows from the Yale potential suggests the following model [Feshbach (76)]. At special values of the energy there will be an optical model resonance (a peak would be sufficient) in a given partial wave, say L . The energy width of these peaks is on the order of a few MeV, and a corresponding lifetime of a few times 10^{-22} s. During this time, the system will couple with other partitions of the $^{12}\text{C} + ^{12}\text{C}$ system. This could include inelastic excitations of either or both ^{12}C to such levels as the 2^+ , 4.43-MeV level or the 0^+ , 7.63-MeV level. It could include such reaction channels as $^{20}\text{Ne} + \alpha$ or $^8\text{Be} + ^{16}\text{O}$, involving various excited states of these nuclei. This coupling will convert some of the initial kinetic energy of the system into internal energy of excitation, making possible the formation of quasi-bound states. Generally, the coupling will tend to fragment the optical model resonance (or shape maximum) into a number of resonances of a smaller width as observed [Fletcher, Foy, et al. (76)]. These are the doorway states, which couple to even more complex states. Interestingly, the sum of the widths for the doorway state resonance of a given L is on the order of the width of the optical potential resonance. This qualitative description leaves problems for the theorists and experimentalists. For the latter it requires experiments that will determine which of the various excitations are involved and with what amplitudes. Theoretically, it is necessary to solve the coupled Schrödinger equations implied by the description above and to find the conditions under which isolated doorway state resonances will be developed.

However, some qualitative conditions follow from (III.4.16). Obviously, Γ^\dagger , that is, the probability of coupling to more complex modes, cannot be too large, for then the resonant amplitude will be much reduced. This width depends multiplicatively on the density of the more complex states and the coupling matrix element. Table 5.1 gives the level density in the compound nucleus relative to $^{12}\text{C} + ^{12}\text{C}$ at the Coulomb barrier energy [Hanson, Stokstad, et al. (74)].

We have only tabulated those cases with the lowest relative level density, except for the $^{14}\text{N} + ^{14}\text{N}$ case, which shows the large effect of the entrance channel. The condition of low relative level density is not a sufficient condition, as the absence of resonances in the $^9\text{Be} + ^{12}\text{C}$ reaction suggests. It is proposed as a necessary condition. It is, in addition, necessary that the matrix elements coupling the doorway state to more complex states also be small. In the

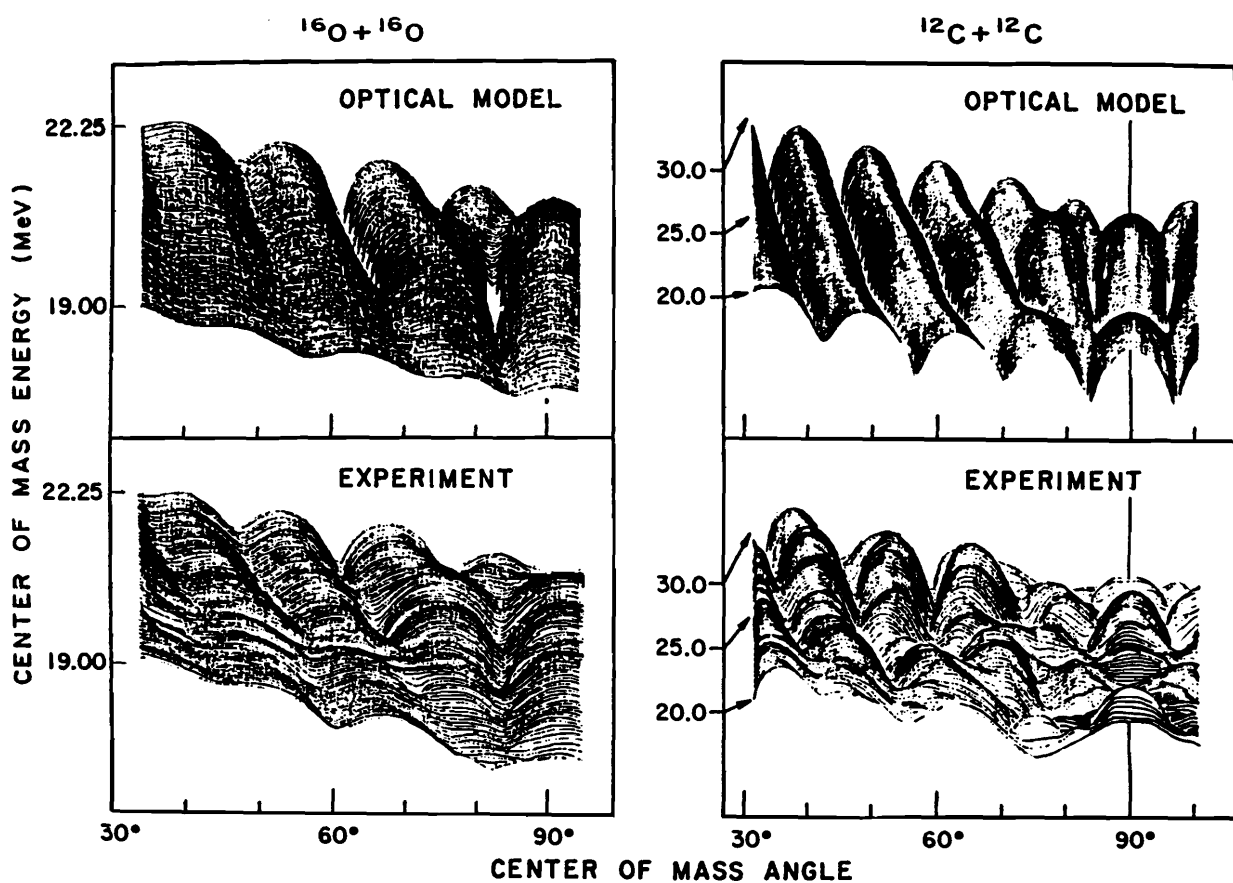


FIG. 5.14. Comparison of the experimental angle-energy cross-section surfaces with the corresponding optical model for the $^{16}\text{O} + ^{16}\text{O}$ and $^{12}\text{C} + ^{12}\text{C}$ systems. [From Gobbi, Wieland, et al. (73).]

TABLE 5.1

Reaction	Compound System	E_x Coulomb Barrier, (MeV)	Relative Level Density
$^{12}\text{C} + ^{12}\text{C}$	^{24}Mg	20.6	1
$^9\text{Be} + ^{12}\text{C}$	^{21}Ne	21.7	3.3
$^{12}\text{C} + ^{16}\text{O}$	^{28}Si	25.2	3.8
$^{14}\text{N} + ^{14}\text{N}$	^{28}Si	35.8	110
$^{12}\text{C} + ^{13}\text{C}$	^{25}Mg	22.9	7.1
$^{11}\text{B} + ^{12}\text{C}$	^{23}Na	23.8	11
$^{12}\text{C} + ^{14}\text{C}$	^{26}Mg	25.7	13
$^{10}\text{B} + ^{12}\text{C}$	^{22}Na	23.0	15

$^{12}\text{C} + ^{12}\text{C}$ case this is likely, since both nuclei are deformed, so that the combined system may not have good overlap with many of the ^{24}Mg levels present at 20.6 MeV, an example of shape isomerism. This leads to the prediction that resonances are more likely to be observable when the colliding nuclei are deformed. In the case of $^9\text{Be} + ^{12}\text{C}$, the relatively easy polarizability of ^9Be because of the valence neutron makes it likely that the coupling matrix elements will be relatively large as will be Γ^{\dagger} .

Another condition requires that the resonant energy E_d fall within the width of the shape resonance. The shape resonance maximizes the value of the matrix element $\langle \phi_i | H_{DP} \chi_i^{(+)} \rangle$ since $\chi_i^{(+)}$ has its maximum value in the interaction region. When the coupling between the entrance channel wave function and the intermediate channels is strong, there may very well be a correspondingly strong energy shift, which may move E_d outside the range in energies in which $\chi_i^{(+)}$ is large. One should also note that the transition matrix element to the final state $\langle \chi_f^{(-)} | H_{PD} \psi_d \rangle$ must be sufficiently large so that the particular final state show the resonance. As a corollary, the cross section to not all final states will have an observable resonance.

Finally, note that an important parameter is the angular momentum range over which the incident channel wave function is relatively large. In the case of $^{12}\text{C} + ^{12}\text{C}$ this angular momentum window is narrow. This may not be the case for other systems. If so, one may well find resonances with differing values of L within a given energy interval. This is the case for the $^{12}\text{C} + ^{16}\text{O}$ system, where the angular momentum window is on the order of 3 to 4 units. See Fletcher and Frawley (81) and Braun-Munzinger (81).

It appears that $^{12}\text{C} + ^{12}\text{C}$ is a unique system in that the conditions discussed above for isolated resonances to be observable seem to be satisfied. The $^{12}\text{C} + ^{16}\text{O}$ system is not as clear cut, as there is much controversy with regard to spin assignments.

The relatively large $^{12}\text{C} + ^{12}\text{C}$ elastic widths reported above imply that the $^{12}\text{C} + ^{12}\text{C}$ amplitude, in which both ^{12}C 's are in their ground states, is a significant part of the entire wave function; or in other words, the probability

of finding the system in that incident channel is substantial. It is for this reason that Bromley et al. properly refer to these states as the states of a nuclear molecule. The existence of components of the wave function in which one or both of the ^{12}C 's is excited to the 2^+ , 4.43-MeV level has been detected by Cormier, Applegate et al. (77) and Cormier, Jackenski et al. (78), for example by measuring the 4.43-MeV radiation and the correlation of its magnitude with the resonance structure. This demonstrates that the wave function of the system is a combination of the elastic channel with channels in which one or both carbon nuclei are excited and presumably other channels, such as $^{20}\text{Ne} + \alpha$ and $^8\text{Be} + ^{16}\text{O}$.

The spherical potential (labeled "Yale") is an oversimplification. In the first place the carbon nuclei in their ground state are oblate. As a consequence, their interaction will depend on the relation orientation of their symmetry axes. Second, as we see next, the Pauli principle plays an essential role.

Harvey (75) has given an intuitive and instructive demonstration of the importance of the Pauli principle, and at the same time has shown that the intermediate state is deformed. It is in fact "superdeformed." As illustrated in Fig. 5.15, the nucleus C in its ground state, according to the harmonic oscillator model, consists of four nucleons on the $1s$ shell and eight on the $1p$ shell. The figure shows the nucleon configuration for the two colliding ^{12}C nuclei. Assuming that the nuclei approach along the z axis with their axes of symmetry perpendicular to that axis, only the value of n_z is presumed to change. For example, four of the nucleons in the $1s$ state in the incident carbons will go into $1s$ state in $^{24}\text{Mg}^*$, which precludes its being filled by nucleons in the $(00\frac{1}{2})$ state in ^{12}C . These must go to the (002) and (003) state. There is no way of

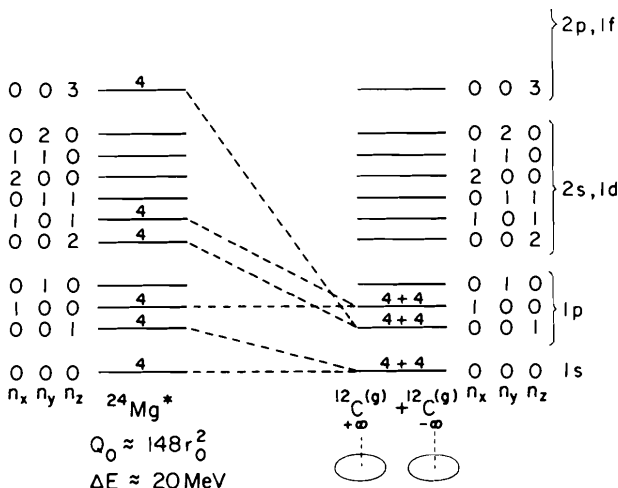


FIG. 5.15. Formation of excited states of ^{24}Mg by $^{12}\text{C} + ^{12}\text{C}$ collision. Symmetry axes are parallel. [From Harvey (75); Rae (87).]

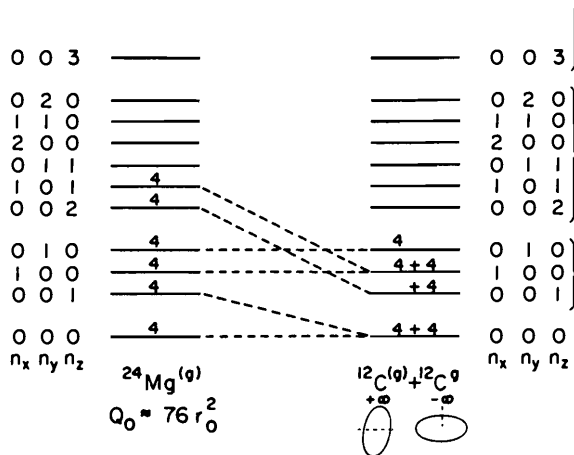


FIG. 5.16. Formation of excited states of ^{24}Mg by $^{12}\text{C} + ^{12}\text{C}$ collision. Symmetry axes are orthogonal. [From Harvey (75).]

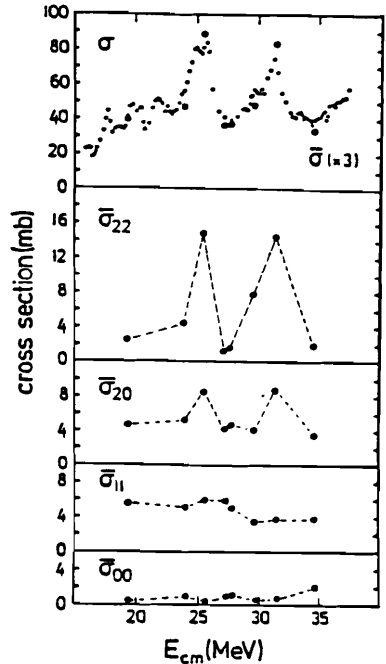
filling the (010) state in ^{24}Mg . The result is a four particle–four-hole state, substantially deformed.

On the other hand, if the axes of the two carbon nuclei are orthogonal as in Fig. 5.16, then as shown in the figure the ground state of ^{24}Mg can be populated. A collision with this orientation of the symmetry axes cannot produce the resonant states we have been discussing but rather, would produce the states of the ground-state band.

Remarkably, this picture has been verified by experiment [Konnerth, Dürnweber et al. (85)]. These authors studied the spin orientations in the reaction $^{12}\text{C} + ^{12}\text{C} \rightarrow ^{12}\text{C}(2^+) + ^{12}\text{C}(2^+)$ by measuring the directions of both 4.439-MeV γ -ray emitted by each $^{12}\text{C}(2^+)$ in coincidence with each mutually inelastic scattering event. Taking the axis of quantization perpendicular to the scattering plane and integrating over the azimuth, it becomes possible to decompose the cross section for the reaction into components $\bar{\sigma}_{|m_1||m_2|}$. Here m_i is the projection of the spin of the quadrupole radiation and therefore of the spin of the emitting $^{12}\text{C}^*$ on the quantization axis. The results are shown in Fig. 5.17. The resonance examined are two of those observed by Cormier, Applegate et al. (77) and Cormier, Jackenski, et al. (78) at $E_{\text{cm}} = 25.6$ and 31.5 MeV. We see very strong maxima in the $\bar{\sigma}_{22}$ cross section, implying that, for the most part, the spins of the two emitting nuclei are parallel while they rotate about each other with the appropriate angular momentum. This result confirms Harvey's picture presented in Figs. 5.15 and 5.16.

It is necessary to go beyond Harvey's considerations, to obtain a more quantitative and clearer understanding. Several models have been studied. Leander and Larsson (75) and Larsson et al. (76) calculated the potential energy surface for $N = Z$ nuclei using essentially the Nilsson–Strutinsky procedure.

FIG. 5.17. Decomposition of the cross section for mutually inelastic $^{12}\text{C} + ^{12}\text{C}$ scattering into the contributions from different m -substate combinations. The particle-inclusive cross section $\bar{\sigma}$ (scaled up by a factor of 3 in the upper panel, large dots) and the contributions $\bar{\sigma}|m_1||m_2|$ (the sum of which yields $\bar{\sigma}$) are integrated over the angular range $45^\circ < \theta_{\text{cm}} < 90^\circ$. The total integrated cross section σ (small dots, upper panel) is taken from Cormier, Applegate, et al. (77). The target thickness corresponds to an average over $E_{\text{cm}} = 100$ to 170 KeV. [From Konnerth, Dünneweber, et al. (85).]



Chandra and Mosel (78) used the two-center model, while Rae (87) and Rae and Marsh (85) employ the cranked-cluster model. The results are quite consistent.

Leander and Larsson's results are summarized in Table 5.2 and an example of (^{24}Mg) of the potential energy surface is shown in Fig. 5.18. The table lists the minima together with the ratios of the harmonic oscillator parameters ω_x : ω_y : ω_z . For many of the minima these are ratios of whole numbers and would be expected to give rise to superdeformed bands. The ground state of ^{24}Mg and the next minimum ($\epsilon = 1.0$, $\gamma = 0$, $\epsilon_3 = 0.3$) correspond to prolate spheroid shapes; the next three are oblate ($\epsilon = 1.23$, $\gamma = 6^\circ$), triaxial ($\epsilon = 1.26$, $\gamma = 42^\circ$), and "chain" ($\epsilon = 1.25$, $\gamma = 0$). The corresponding density contours as obtained by Rae and Marsh [Rae (87)] are shown in Fig. 5.19. We see that the chain consists of 6α clusters in a row; the oblate is given by (d) while the triaxial (g) appears to be two-carbon nuclei aligned perpendicular to the line joining their centers. The prolate configuration (e) appears to be of the α - ^{16}O - α form. The triaxial minimum corresponds, then, to the resonances observed by Cormier, Applegate, et al. (77) and Cormier, Jackenski, et al. (78). With respect to the resonances at lower energies there is some debate. Rae (87) believes these to be generated by the prolate configuration, while Cosman (81) and Ledoux, Ordonez, et al. (84) assign all the resonances to the triaxial minimum. According to Rae, the Cormier resonances have spins of 16, 18, and 20, starting a new band,

TABLE 5.2 Properties of the Minima in the Potential Energy Surfaces for the Doubly Even $N-Z$ Nuclei^a

Nucleus	ε	ε_3	ε_4	γ (deg)	Configuration	$\omega_x:\omega_y:\omega_z$	Energy (MeV)	
							Min.	Barr.
¹² C	0.83	0	0.20	60	(1) ⁻⁴	2:1:1	0	
	1.11	0	0.24	0	(1) ⁻⁸ (2) ⁴	3:3:1	1	14
¹⁶ O	0.00	0	0.00	0		1:1:1	0	
	1.04	0	0.24	43	(1) ⁻⁴ (2) ⁴	4:2:1	9	16
²⁰ Ne	1.2	0	0.24	0	(1) ⁻⁸ (2) ⁴ (3) ⁴	4:4:1	9	20
	0.40	0	-0.10	0	(2) ⁴	2:2:1	0	
	1.17	0	0.24	50	(1) ⁻⁴ (2) ⁸	8:3:2	9	14
	1.25	0	0.24	0	(1) ⁻⁸ (2) ⁴ (3) ⁴ (4) ⁴	5:5:1	13	21
²⁴ Mg	0.45	0	0.08	20	(2) ⁸	4:3:2	0	
	1.0	0.3	0.20	0	(2) ⁴ (3) ⁴		(6)	12.5
	1.23	0 ^b	0.24	60	(1) ⁻⁴ (2) ¹²	3:1:1	8	14.5
	1.26	0	0.24	42	(1) ⁻⁴ (2) ⁸ (3) ⁴	5:2:1	10	14.5
	1.25	0	0.08	0	(1) ⁻⁸ (2) ⁴ (3) ⁴ (4) ⁴ (5) ⁴	6:6:1	20	25
²⁸ Si	0.49	0	-0.06	60	(2) ¹²	2:1:1	0	
	0.45	0	0.16	0	(2) ¹²	3:3:2	1	3.5
	1.0	0.3	0.20	0	(2) ⁴ (3) ⁴ (4) ⁴		13	15.5
	1.35	0	0.24	60	(1) ⁻⁴ (2) ¹² (3) ⁴		13	17.5
³² S	1.32	0	0.24	35	(1) ⁻⁴ (2) ⁸ (3) ⁴ (4) ⁴	6:3:1	19	20
	0.21	0	0.08	20	(2) ⁻⁸	5:4:3	0	
	0.68	0	0.08	0	(2) ⁻¹² (3) ⁴	2:2:1	0.1	4.5
	1.42	0	0.24	54	(1) ⁻⁴ (2) ⁻¹² (3) ⁸	10:3:2	16	18
	1.0	0.3	0.20	0	(2) ⁸ (3) ⁴ (4) ⁴		16	17
³⁶ Ar	1.30	0	0.24	30	(1) ⁻⁴ (2) ⁸ (3) ⁸ (4) ⁴		21	23
	0.29	0	0.16	60	(2) ⁻⁴	3:2:2	0	
	0.74	0	0.16	7	(2) ⁻¹² (3) ⁸		9	11
	1.45	0	0.24	55	(1) ⁻⁴ (2) ⁻¹² (3) ¹²		27	27.5
⁴⁰ Ca	1.33	0	0.24	47	(1) ⁻⁴ (2) ⁻¹² (3) ⁸ (4) ⁴		27	27.5
	0.00	0	0.00	0		1:1:1	0	
	0.45	0	0.16	50	(2) ⁻⁴ (3) ⁴	7:5:4	9	10.5
⁴⁴ Ti	0.84	0	0.08	5	(2) ⁻¹² (3) ⁸ (4) ⁴		17	18
	1.50	0	0.24	60	(1) ⁻⁴ (2) ⁻¹² (3) ¹⁶		34	36.5
	0.18	0	0.00	0	(3) ⁴	3:3:2	0	
	0.52	0	0.16	38	(2) ⁻⁴ (3) ⁸		3	5.5
	0.86	0	0.16	0	(2) ⁻¹² (3) ¹² (4) ⁴		11	15
	1.50	0	0.24	60	(1) ⁻⁴ (2) ⁻¹² (3) ¹⁶ (4) ⁴		29	31.5

^aThe deformation parameters ε , ε_3 , ε_4 , γ are defined in the legend to Fig. 5.18. The last two columns contain the energy and minimum barrier height relative to the ground-state minimum.

^b $\varepsilon_{33} = 0.05$.

Source: Leander and Larsson (75).

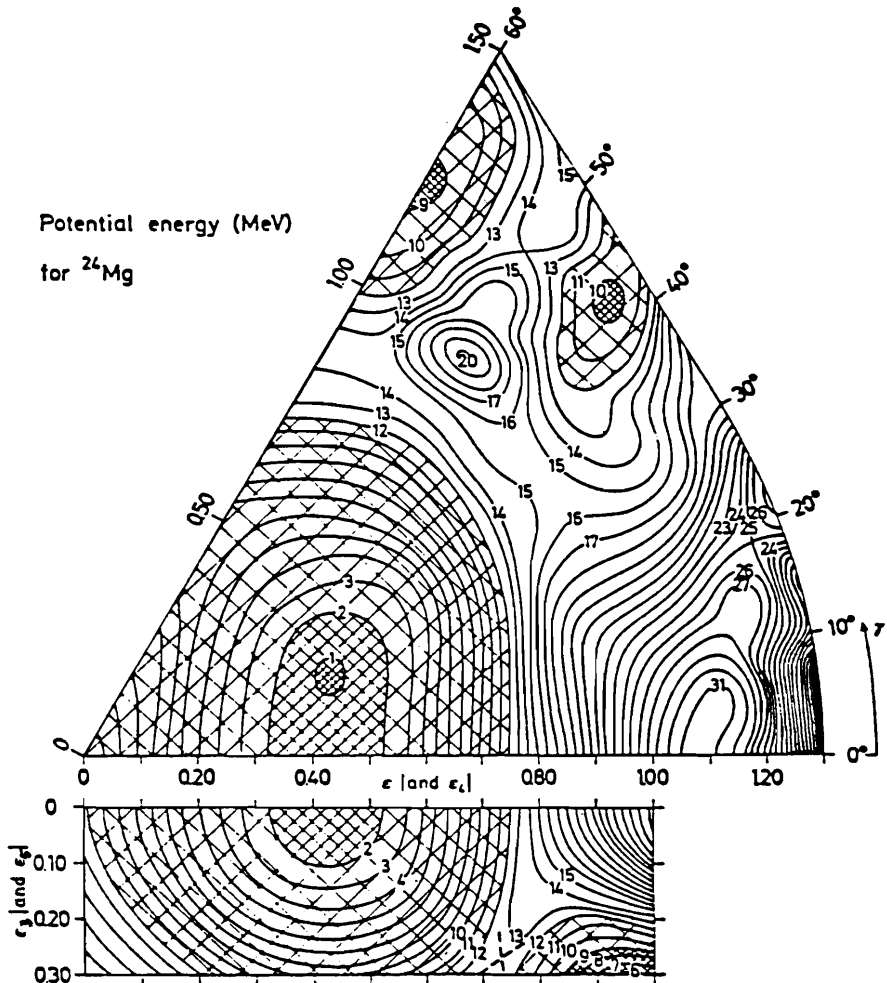


FIG. 5.18. Potential energy surface for ^{24}Mg . The deformation parameters are defined by the deformed nuclear potential:

$$\begin{aligned}
 V = & \frac{1}{2} \hbar \omega_0 \rho^2 [1 + 2\epsilon_1 P_1(\cos \theta_t) - \frac{2}{3} \epsilon \cos \gamma P_2(\cos \theta_t) \\
 & + \frac{1}{3} \epsilon \sin \gamma \sqrt{\frac{8}{5}} \pi (Y_{22}(\theta_t, \phi_t) + Y_{2-2}(\theta_t, \phi_t)) \\
 & + 2\epsilon_3 P_3(\cos \theta_t) + 2\epsilon_{33} \sqrt{\frac{4}{7}} \pi (Y_{33}(\theta_t, \phi_t) - Y_{3-3}(\theta_t, \phi_t)) \\
 & + 2\epsilon_4 P_4(\cos \theta_t) + 2\epsilon_5 P_5(\cos \theta_t)] \\
 & - \kappa \hbar \omega_0 [2l_t \cdot s + \mu(l_t^2 - \langle l_t^2 \rangle)].
 \end{aligned}$$

The potential energy in the (ϵ, γ) plane, including the macroscopic energy, was calculated for each value of (ϵ, γ) and then minimized with respect to ϵ_4 . For the (ϵ, ϵ_3) plane $\gamma = 0$. For definitions of ρ, θ_t , and ϕ_t , see the original reference. [From Leander and Larsson (75).]

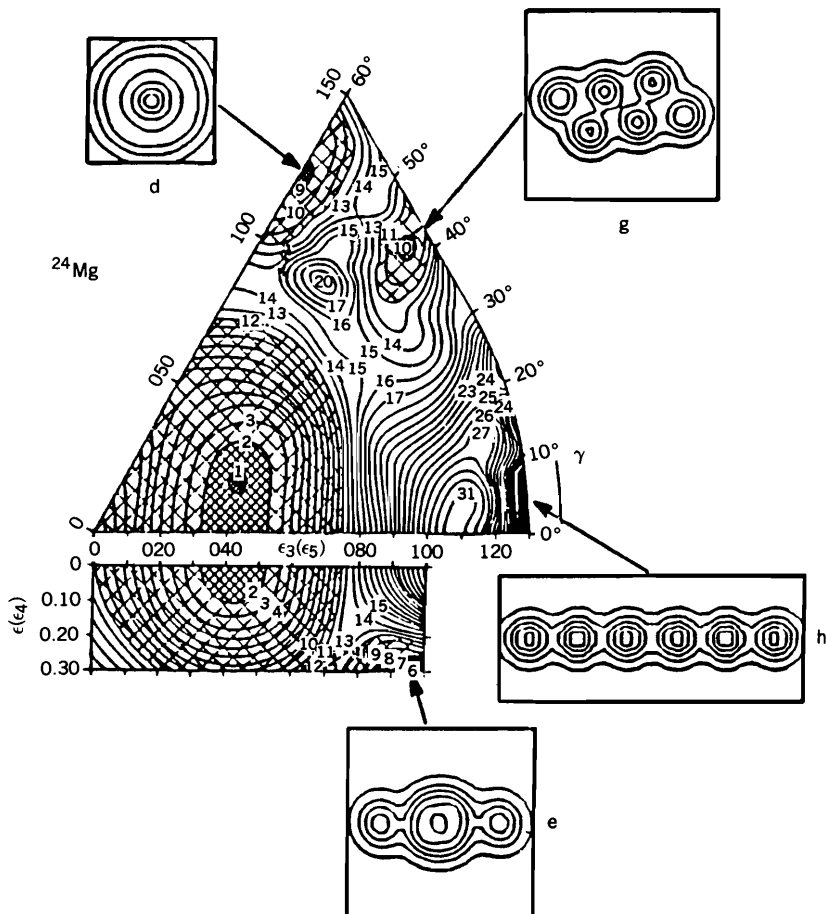


FIG. 5.19. Potential energy surface for ^{24}Mg (see Fig. 5.19) together with density contours for the stable cluster configurations. [From Rae and Marsh as described by Rae (87).]

while Cosman and Ledoux et al. would have spins of 14, 16, and 18, joining in with the lower-energy band.

In any event it is evident that deformation must be taken explicitly into account before the $^{12}\text{C} + ^{12}\text{C}$ resonances will be understood. However, at the present time a calculation of the reaction cross sections for the excitation of the resonances taking deformation into account has not been made.

The various theoretical approaches to the problem of heavy-ion resonances, particularly in the $^{12}\text{C} + ^{12}\text{C}$ and $^{12}\text{C} + ^{16}\text{O}$ cases, fit the rubric described earlier. The intermediate states that couple to the incident channel is taken to be $^{12}\text{C}(\text{g.s.}) + ^{12}\text{C}(2^+)$ by Imanishi (68, 69). Konda, Abe, and Matsuse (79) include the excitation of both ^{12}C 's to the 2^+ state. Similar studies have been

made by Schied, Greiner, and Lemmer (70) and their colleagues [Greiner and Scheid (71)]; Fink et al. (72); Park et al. (74)]. The α -particle model of Michaud and Vogt (69, 72) can be considered as equivalent to involving intermediate states in which the ^{12}C nuclei are excited to the 7.67-MeV 0^+ level. The calculations made are of the coupled-channel variety. A simplified version has been presented by Abe (78). However, these calculations do not take into account the deformation effects alluded to above.

Other models have been proposed by Cindro (78a), Cindro and Greiner (83), and Iachello (81). Cindro assumes that the resonance energies are given by the spectrum of the rotational and vibrational excitations of a quadrupole. Iachello assumes that the spectrum is that of a three-dimensional vibrator. His four-parameter expression for the resonances fits the observed spectrum quite clearly [Erb and Bromley, (81)], but an underlying microscopic justification is still lacking. The prolate spheroidal configuration (e) of the cluster model according to Rae and Marsh (85), would provide such a justification. Additional supporting evidence is provided by time-dependent Hartree-Fock (TDHF) calculations [Strayer, Cusson, et al. (84); Umar, Strayer, et al. (85); Umar and Strayer (86)]. See also Satpathy et al. (86) and critical remarks by Kato and Abe (87).

6. DIFFUSION THEORY

The remaining sections of this chapter are devoted to theory, with emphasis on the deep inelastic process. It is not possible to review here all of the many theoretical models that have been proposed for the description of this process. In this regard not even the Bromley volumes are complete. The semiclassical method is the subject of a book by Broglia and Winther (1981). The master equation, which has been used, for example, by Agassi, Ko, and Wiedenmuller (77, 79), is reviewed by Dietrich (85). The hydrodynamic model, advanced by W. Greiner and his colleagues, is discussed by Maruhn (85) in the same set of lectures. A transport theory that takes into account the coupling between the collective and intrinsic degrees of freedom because of two-body collisions has been developed by Nörenberg (85) [see also Ayik and Nörenberg (82) and Cassing and Nörenberg (83)]. He refers to this description as "dissipative adiabatic dynamics." Hofmann and Siemens (76, 77) have investigated a linear response theory. The internuclear cascade has been exploited by Fraenkel and his colleagues [Chen et al. (68); Yariv and Fraenkel (79, 81)] and by Cugnon (82). This procedure is briefly discussed in Chapter IX. There are many others, other names to be associated with the above as well as other approaches. In this chapter we discuss the application of the classical transport equation of Uehling and Uhlenbeck, by Aichelin and Bertsch [(85)], Aichelin [(86)] as well as the time-dependent Hartree-Fock (TDHF) methods [Negele (82)], but not the adiabatic time-dependent Hartree-Fock method of Villars (77) and Moya de Guerra and Villars (77). This choice is idiosyncratic, based in part on a prejudice

for theories that do not assume thermal equilibrium, based in part on the availability of examples of quantitative applications.

All of these theories require extensive numerical calculations, making it difficult to establish an intuitional understanding of the dynamics for a wide set of parameters. For that reason we first establish some qualitative features making use of the theory of multistep direct reactions described in Chapter VII, which is appropriate for the study of deep inelastic processes. Note that the application of that theory uses the cross section for the single-step process, which is obtained from the understanding of the quasi-elastic cross sections. The double differential cross section for the statistical multistep direct process is given by (VII.5.29) and repeated below:

$$\left[\frac{d^2\sigma(\mathbf{k}_f, \mathbf{k}_i)}{d\Omega_f dU_f} \right]_{msd} = \sum_{\substack{\alpha, m \\ m = \alpha \pm 1}} \int \frac{d\mathbf{k}_1}{(2\pi)^3} \dots \int \frac{d\mathbf{k}_\alpha}{(2\pi)^3} \left[\frac{d^2 w_{m,\alpha}(\mathbf{k}_f, \mathbf{k}_\alpha)}{d\Omega_f dU_f} \right] \left[\frac{d^2 w_{\alpha,\alpha-1}(\mathbf{k}_\alpha, \mathbf{k}_{\alpha-1})}{d\Omega_\alpha dU_\alpha} \right] \dots \left[\frac{dw_{2,1}(\mathbf{k}_2, \mathbf{k}_1)}{d\Omega_2 dU_2} \right] \left[\frac{d^2\sigma_{1i}(\mathbf{k}_1, \mathbf{k}_i)}{d\Omega_1 dU_1} \right] \quad (6.1)$$

The cross section for a single-step process is to added. The sum is over α which indicates the number of steps that is followed by transition to the final states designated by $\alpha \pm 1$ and \mathbf{k}_f . The momenta $\hbar\mathbf{k}_\alpha$ are the relative momenta of the two interacting nuclei, while the subscript α includes the internal quantum numbers and energies of the states of the two nuclei. Note that the deep inelastic process is a two-body reaction, so that \mathbf{k}_f refers to the relative momentum of the two final nuclei. U_f is then the total excitation energy given by

$$U_f = E - \frac{\hbar^2}{2\mu} k_f^2 \quad (6.2)$$

where μ is the reduced mass. It is necessary to include the independent variables describing the exchange of charge and mass. Following Greiner these are taken to be

$$\eta^{(A)} \equiv \frac{A_t - A_p}{A_t + A_p} \quad \eta^{(Z)} \equiv \frac{Z_t - Z_p}{Z_t + Z_p} \quad (6.3)$$

where the subscripts t and p refer to the target and projectile, respectively. The one-step transition probabilities are dependent on the variables $\eta_\alpha^{(A)}$ and $\eta_\alpha^{(Z)}$ and $\eta_{\alpha-2}^{(A)}$ and $\eta_{\alpha-1}^{(Z)}$ where the subscript α denotes the stage. The differential transition probability is given by (VII.5.30)

$$\frac{d^2 w_{\alpha,\alpha-1}(\mathbf{k}_\alpha, \eta_\alpha; \mathbf{k}_{\alpha-1}, \eta_{\alpha-1})}{dU_\alpha d\Omega_\alpha} = 2\pi^2 \rho(\mathbf{k}_\alpha) \rho(U_\alpha) |\bar{v}(\mathbf{k}_\alpha, \eta_\alpha; \mathbf{k}_{\alpha-1}, \eta_{\alpha-1})|^2$$

where the dependence on $\eta_\alpha^{(A)}$ and $\eta_\alpha^{(Z)}$ is indicated by η_α . Finally, changes in

deformation of each of the nuclei in the transition from stage to stage may occur so that deformation parameters should also be included as independent variables in (6.4).

Equation (6.1) provides a framework for the calculation of the cross section. The physics has yet to be inserted, namely the nature of each of the intermediate stages. There are many possibilities for a heavy-ion reaction and a method for a rapid exploration has not been developed; presumably, some simulation using a Monte Carlo evaluation could be used. One therefore turns to an approximate method that will yield an expression whose form can be compared with experiment, yielding some overall information on the intermediate stages involved.

For reasons of clarity we shall suppress, for the time being, the dependence on $\eta^{(A)}$ and $\eta^{(Z)}$. Define the transfer function $Y_\alpha(\mathbf{k}_\alpha)$ as follows:

$$Y_\alpha(\mathbf{k}_\alpha) \equiv \int \frac{d\mathbf{k}_1}{(2\pi)^3} \dots \int \frac{d\mathbf{k}_{\alpha-1}}{(2\pi)^3} \frac{d^2 w_{\alpha,\alpha-1}}{d\Omega_\alpha dU_\alpha} \dots \frac{d^2 w_{2,1}}{d\Omega_2 dU_2} \frac{d^2 w_{1i}}{d\Omega_1 dU_1} \quad (6.4)$$

The cross section is then given by

$$\begin{aligned} \left[\frac{d^2 \sigma(\mathbf{k}_f, \mathbf{k}_i)}{d\Omega_f dU_f} \right]_{\text{msd}} &= \frac{2\pi\mu}{\hbar^2 k_{i,m,v}} \sum \int \frac{d\mathbf{k}_v}{(2\pi)^3} \frac{d^2 w_{m,v}}{dU_f d\Omega_f} Y_v(\mathbf{k}_v) \\ &= \sum_v \int \frac{d\mathbf{k}_v}{(2\pi)^3} \left[\frac{d^2 \sigma(\mathbf{k}_{v+1}, \mathbf{k}_v)}{d\Omega_f dU_f} \Bigg|_{\mathbf{k}_{v+1} \rightarrow \mathbf{k}_f} + \frac{d^2 \sigma(\mathbf{k}_{v-1}, \mathbf{k}_v)}{d\Omega_f dU_f} \Bigg|_{\mathbf{k}_{v-1} \rightarrow \mathbf{k}_f} \right] \quad (6.4') \end{aligned}$$

The transfer function Y_v satisfies the equation

$$Y_v(\mathbf{k}_v) = \int \frac{d\mathbf{k}_{v-1}}{(2\pi)^3} \frac{d^2 w_{v,v-1}(\mathbf{k}_v, \mathbf{k}_{v-1})}{d\Omega_v dU_v} Y_{v-1}(\mathbf{k}_{v-1}). \quad (6.5)$$

The assumption is now made that the change in momentum in the transition from stage $v-1$ to stage v is small. One may therefore expand $Y_{v-1}(\mathbf{k}_{v-1})$ in terms of $Y_{v-1}(\mathbf{k}_v)$ as follows:

$$Y_{v-1}(\mathbf{k}_{v-1}) = Y_{v-1}(\mathbf{k}_v) + (\mathbf{k}_{v-1} - \mathbf{k}_v) \cdot \nabla Y_{v-1} + \frac{1}{2} [(\mathbf{k}_{v-1} - \mathbf{k}_v) \cdot \nabla]^2 Y_{v-1} \dots$$

Inserting this equation in (6.5) yields

$$Y_v(\mathbf{k}_v) = W_v^{(0)}(\mathbf{k}_v) Y_{v-1}(\mathbf{k}_v) + \mathbf{W}_v^{(1)}(\mathbf{k}_v) \cdot \nabla Y_{v-1}(\mathbf{k}_v) + \frac{1}{2} \sum_{a,b} W_{ab} \nabla_a \nabla_b Y_{v-1}(\mathbf{k}_v) \quad (6.6)$$

where

$$W_v^{(0)} = \int \frac{d\mathbf{k}_{v-1}}{(2\pi)^3} \frac{d^2 w_{v,v-1}(\mathbf{k}_v, \mathbf{k}_{v-1})}{d\Omega_v dU_v} \quad (6.7a)$$

$$\mathbf{W}_v^{(1)} = \int \frac{d\mathbf{k}_{v-1}}{(2\pi)^3} (\mathbf{k}_{v-1} - \mathbf{k}_v) \frac{d^2 w_{v,v-1}(\mathbf{k}_v, \mathbf{k}_{v-1})}{d\Omega_v dU_v} \quad (6.7b)$$

and

$$W_{ab} = \int \frac{d\mathbf{k}_{v-1}}{(2\pi)^3} (\mathbf{k}_{v-1} - \mathbf{k}_v)_a (\mathbf{k}_{v-1} - \mathbf{k}_v)_b \frac{d^2 w_{v,v-1}(\mathbf{k}_v, \mathbf{k}_{v-1})}{d\Omega_v dU_v} \quad (6.7c)$$

The subscripts a and b refer to Cartesian components. We simplify (6.6) by introducing the quantity

$$f_v \equiv \prod_1^v W_\alpha^0(\mathbf{k}_\alpha) \quad W_v^0 = \frac{f_v}{f_{v-1}} \quad v \geq 1, \quad f_0 = 1 \quad (6.8)$$

and the new dependent variable Z_v

$$Z_v \equiv \frac{Y_v}{f_v} \quad (6.9)$$

Equation (6.6) becomes

$$W_v^0(Z_v - Z_{v-1}) = \frac{1}{f_{v-1}} [\mathbf{W}_v^{(1)} \cdot \nabla (f_{v-1} Z_{v-1})] + \frac{1}{2f_{v-1}} \sum_{ab} W_{ab} \nabla_a \nabla_b (f_{v-1} Z_{v-1}) \quad (6.10)$$

We replace the discrete variable v by continuous variables τ such that $\Delta\tau = 1/W_v^0$. Then the left-hand side of (6.10) is given by $\Delta Z/\Delta\tau$, which is approximated by $\partial Z/\partial\tau$. Note that

$$\tau = \sum_{\alpha=1}^v \frac{1}{W_\alpha^0} \quad (6.11)$$

It is clearly a variable that measures the number of stages and can be conveniently thought of as the interaction time.[‡] It is a function of v and \mathbf{k}_v among other variables. One eliminates v on the right side of (6.10) by solving (6.11) for v in terms of τ and \mathbf{k} . The equation for Z becomes

$$\frac{\partial Z}{\partial \tau} = \frac{1}{f(\tau, \mathbf{k})} [\mathbf{w}_1 \cdot \nabla (fZ) + \frac{1}{2} \sum w_{ab} \nabla_a \nabla_b (fZ)] \quad (6.12)$$

[‡]If W_α^0 is independent of α , $\tau = v/W_0$. If as is more realistic, $W_\alpha^0 = e^{-\alpha\gamma} W$, $W\tau = (e^{\gamma(v+1)} - 1)/e^\gamma - 1$. Solving for v , $v = 1/\gamma \ln [(1 - W\tau)e^{-\gamma} + W\tau]$, which approaches $v = 1/\gamma \ln W\tau$ for large γ and $W\tau - 1$ for small γ .

where

$$\mathbf{w}_1(\tau, \mathbf{k}) = W_v^{(1)}(\mathbf{k}_v) \quad \text{etc.} \quad (6.13)$$

We have thus obtained a momentum Fokker–Planck diffusion equation for Z in a very general form. To make further progress, assume that

$$w_{ab} = \delta_{ab}w$$

and that f depends only on τ . This is accomplished by replacing \mathbf{k} in f by \mathbf{k}_τ . See (6.15). Then (6.12) becomes

$$\frac{\partial Z}{\partial \tau} = \mathbf{w}_1 \cdot \nabla Z + \frac{1}{2}w \nabla^2 Z. \quad (6.14)$$

Further simplification is obtained by assuming that w is independent of k . Equation (6.14) can be solved in a closed form when \mathbf{w}_1 is a constant vector or proportional to a unit vector tangent to the unit sphere in \mathbf{k} space. We shall follow an approximate procedure that reproduces correctly the solutions for the above assumptions for \mathbf{w}_1 , but is capable of dealing with a more general form for this vector.

We assume that

$$Z(\mathbf{k}, \tau) = \left(\frac{1}{2\pi w \tau} \right)^{3/2} e^{-(1/2\tau w)(\mathbf{k} - \mathbf{k}_\tau)^2} \quad (6.15)$$

where \mathbf{k}_τ is a function of τ reducing to \mathbf{k}_0 at $\tau = 0$. Note that $Z(k, \tau) \rightarrow \delta(\mathbf{k} - \mathbf{k}_0)$ as $\tau \rightarrow 0$. Here \mathbf{k}_0 is taken to be \mathbf{k}_i the incident \mathbf{k} for the collision of light nuclei. For heavy nuclei when the collision is Coulomb dominated, \mathbf{k}_0 is taken to be equal in magnitude to k_i but with the direction given by the grazing Coulomb orbit at the point of grazing. To determine \mathbf{k}_τ we calculate

$$\langle \mathbf{k} \rangle \equiv \int \mathbf{k} Z(\mathbf{k}, \tau) d\mathbf{k} \quad (6.16)$$

Equation (6.14) will then yield a differential equation for \mathbf{k}_τ .

We assume the following form for \mathbf{w}_1 linear in \mathbf{k}

$$\mathbf{w}_1 = \mathbf{w}_C + w_R(\hat{\mathbf{k}}_0 \times \mathbf{k}) + \frac{1}{4}w_D \mathbf{k} \quad (6.17)$$

where \mathbf{w}_C is a constant vector independent of \mathbf{k} . Multiplying (6.14) by \mathbf{k} and integrating yields

$$\frac{d\mathbf{k}_\tau}{d\tau} = -[\mathbf{w}_C + (\hat{\mathbf{k}}_0 \times \mathbf{k}_\tau)w_R + w_D \mathbf{k}_\tau] \quad (6.18)$$

These equations can be integrated subject to the condition $\mathbf{k}_\tau(0) = \mathbf{k}_0$. Let the direction along \mathbf{k}_0 to be designated by the 0 subscript. One obtains

$$(\mathbf{k}_\tau)_0 = \mathbf{k}_0 e^{-w_D \tau} - \frac{(\mathbf{w}_C)_0}{w_D} (1 - e^{-w_D \tau}) \quad (6.19)$$

and

$$\begin{aligned} (\mathbf{k}_\tau)_\perp = \frac{1}{w_D^2 + w_R^2} \{ & \hat{\mathbf{k}}_0 \times (\hat{\mathbf{k}}_0 \times \mathbf{w}_C) [w_D (1 - \cos \omega_R \tau e^{-w_D \tau}) + \omega_R \sin \omega_R \tau e^{-w_D \tau}] \\ & + (\hat{\mathbf{k}}_0 \times \mathbf{w}_C) [w_R (1 - \cos \omega_R \tau e^{-w_D \tau}) - w_D \sin \omega_R \tau e^{-w_D \tau}] \} \end{aligned} \quad (6.19a)$$

Here $(\mathbf{k}_\tau)_\perp$ is the component of \mathbf{k}_τ in the plane perpendicular to \mathbf{k}_0 . The sinusoidal terms describe a damped rotation in the $(k_\tau)_\perp$ plane with a radius given by $w_{C\perp} / \sqrt{w_D^2 + w_R^2}$. For large τ

$$(k_\tau)_\perp \xrightarrow{\tau \rightarrow \infty} \frac{1}{w_D^2 + w_R^2} [(\hat{\mathbf{k}}_0 \times (\hat{\mathbf{k}}_0 \times \mathbf{w}_C)) w_D + (\hat{\mathbf{k}}_0 \times \mathbf{w}_C) w_R] \quad (6.20)$$

The component of \mathbf{k}_τ in the \mathbf{k}_0 direction decreases because of the damping of the \mathbf{k}_0 term. It is also affected by the 0 component of \mathbf{w}_C , subtracting or adding according to whether w_{C0} is positive or negative; w_D is a magnitude and therefore positive. Asymptotically

$$(k_\tau)_0 \rightarrow -\frac{(\mathbf{w}_C)_0}{w_D} \quad (6.21)$$

The value of k_τ^2 , which is proportional to the average kinetic energy is given by the sum $(k_\tau)_\perp^2 + (k_\tau)_0^2$, where

$$\begin{aligned} (k_\tau)_\perp^2 &= \frac{w_{C\perp}^2}{w_D^2 + w_R^2} (1 - 2 \cos \omega_R \tau e^{-w_D \tau} + e^{-2w_D \tau}) \xrightarrow{\tau \rightarrow \infty} \frac{w_{C\perp}^2}{w_D^2 + w_R^2} \\ (k_\tau)_0^2 &= \left[\mathbf{k}_0 e^{-w_D \tau} - \frac{(\mathbf{w}_C)_0}{w_D} (1 - e^{-w_D \tau}) \right]^2 \xrightarrow{\tau \rightarrow \infty} \frac{w_{C0}^2}{w_D^2} \end{aligned} \quad (6.22)$$

Returning to (6.15) for $Z(\mathbf{k}, \tau)$ we see that as τ increases, Z broadens while its center moves from the direction \mathbf{k}_0 to \mathbf{k}_τ given by (6.19). For the motion of \mathbf{k}_τ one can "predict" the solid center lines in Fig. 3.6 (if \mathbf{w}_C , w_R and w_D are known or fitted, if not) where E would be obtained from (6.22) and the deviation from the original \mathbf{k}_0 direction from the equation

$$\tan(\vartheta - \theta_0) = \frac{(k_\tau)_\perp}{(k_\tau)_0} \quad (6.23)$$

where θ_0 is the direction of \mathbf{k}_0 . Note that \mathbf{k}_τ and the energy approach constant asymptotic values, as indicated by Fig. 3.6. Subsequently the energy loss is dominated by excitation of low-lying modes which are described on page 596 as a process that involves long interaction times and a smaller rate of energy loss. This would require a different set of values of w_C , w_R , and w_D as obtained for example from (6.7).

The function $Y(\mathbf{k}, \tau)$ is now obtained from (6.9). Making the reasonable approximation that W_α^0 is independent of α (we have already assumed that it is independent of \mathbf{k}), f_ν is given by $(W_0)^\nu$. Converting from ν to τ dependence, we parametrize f_ν by

$$f_\nu = f_0 e^{-\gamma\tau} \quad (6.24)$$

since τ is proportional to ν . With $Y(\mathbf{k}, \tau)$ known, the cross section can be obtained by summing over ν according to (6.4). The sum over ν is replaced by an integration over τ :

$$\sum_\nu \rightarrow W_0 \int d\tau$$

Hence

$$\begin{aligned} \left[\frac{d^2\sigma}{d\Omega_f dU_f} \right]_{\text{msd}} &= \frac{4\pi\mu}{\hbar^2 k_i} W_0 \int Y d\tau = W_0 \int (s_{\nu+1} + s_{\nu-1}) Y_1(\mathbf{k}_f, \tau) d\tau \\ &\simeq 2W_0 \bar{s} \int Y(\mathbf{k}_f, \tau) d\tau \end{aligned} \quad (6.25a)$$

where we have assumed that

$$\left. \frac{k_\nu}{k_i} \frac{d^2\sigma(\mathbf{k}_{\nu+1}, \mathbf{k}_\nu)}{d\Omega_f dU_f} \right|_{\mathbf{k}_{\nu+1}=\mathbf{k}_f} \simeq (2\pi)^3 \delta(\mathbf{k}_f - \mathbf{k}_\nu) s_{\nu+1} \quad (6.25b)$$

To obtain these equations we have assumed that the angular distribution is sharply pointed in the direction of \mathbf{k}_ν and that the energy is not substantially changed. Finally, it is assumed that s_ν varies slowly with ν and can be replaced by an average \bar{s} .

We now consider the integral.

$$I = \int Y d\tau = f_0 \int_0^\infty \frac{d\tau}{(2\pi\omega\tau)^{3/2}} e^{-\gamma\tau - (1/2\tau w)(\mathbf{k} - \mathbf{k}_\tau)^2} \quad (6.26)$$

As an example of the results which follow from this analysis we taken $w_R = 0$. Then

$$\mathbf{k}_\tau = \mathbf{k}_0 - \left(\frac{w_C}{w_D} + \mathbf{k}_0 \right) (1 - e^{-w_D\tau}) \quad w_R = 0 \quad (6.27)$$

Furthermore, assume that $w_D\tau < 1$. The conditions under which this inequality will hold will be determined in what follows. Then

$$\mathbf{k}_\tau \simeq \mathbf{k}_0 + \mathbf{k}_1\tau \quad (6.28)$$

$$\mathbf{k}_1 = -(\mathbf{w}_C + \mathbf{k}_0 w_D)$$

With this approximation, the integral can be done exactly. However, to identify the important value of τ and so be able to assess the range of validity of the result, we shall use the method of steepest descents. Toward that end one places the derivative of the exponent in (6.26) equal to zero. Solving for τ , one finds that

$$\tau^2 = \frac{(\mathbf{k}_0 - \mathbf{k})^2}{k_1^2 + 2\gamma w} \quad (6.29)$$

We thus see that $w_D\tau$ will be small if $|\mathbf{k}_0 - \mathbf{k}|$ is sufficiently small. For small w_C the condition is

$$w_D\tau \sim \frac{|\mathbf{k}_0 - \mathbf{k}|}{k_0} \ll 1 \quad (6.30)$$

This condition restricts the region of applicability to the forward quadrant but does not strongly restrict the difference between k_0 and k .

The steepest descent result for the integral, (6.26) yields

$$I(\mathbf{k}) = \frac{f_0}{\sqrt{2}(2\pi w)} \frac{1}{|\mathbf{k}_0 - \mathbf{k}|} \exp - \frac{1}{w} [K_1 |\mathbf{k}_0 - \mathbf{k}| + \mathbf{k}_1 \cdot (\mathbf{k}_0 - \mathbf{k})] \quad (6.31)$$

where $K_1^2 \equiv k_1^2 + 2\gamma w$. The cross section is from (6.25)

$$\left[\frac{d^2\sigma}{d\Omega_f dU_f} \right]_{\text{msd}} = 2W_0 \bar{s} I(\mathbf{k}_f). \quad (6.32)$$

The peak of the angular distribution will occur at the minimum of the bracketed expression in (6.31). Let ϑ be the angle between \mathbf{k}_0 and \mathbf{k} and let the minimum occur at $\bar{\vartheta}$. Assuming $\bar{\vartheta}$ to be small, one finds that

$$\sin \bar{\vartheta} = \frac{k_1 |k_0 - k| \sin \psi}{k_0 k_1 + k_1 |k_0 - k| \cos \psi} \quad (6.33)$$

where ψ is the angle between \mathbf{k}_0 and the component of \mathbf{k}_1 in the $(\mathbf{k}, \mathbf{k}_0)$ plane. For ϑ near $\bar{\vartheta}$ the angular distribution is Gaussian.

The energy spectrum at each angle can also be determined from (6.31). Generally, one finds that as the angle increases the rate of exponential decrease

of the cross section increases. [One can always obtain an exponential decay with E for any function $e^{-f(E)}$ for small $E_0 - E$ as long as $f'(E_0)$ is positive as it is in this case.] This is identical to the exponential decrease obtained in the statistical theory [see (I.4.5) to (I.4.7)]. One thus finds the statement in the experimental literature that the "temperature" decreases with increasing angle. However, as we see from the calculation one cannot conclude that the system has approached a thermal equilibrium. For that conclusion to be correct the angular distribution must be spherical corresponding to an angle-independent temperature.

There are other variables, besides the momentum \mathbf{k} , such as mass and charge asymmetry [see (6.3)], and deformation parameters, which can change with each stage of the multistep process. The discussion given above presumes a known path in reaction space or an averaging over the various possibilities. However, this is not adequate when, for example, we wish to calculate the charge and mass distributions of the final fragment. In the analysis to be presented below, we develop a Fokker-Planck equation which explicitly contains the effects of the mass asymmetry $\eta^{(A)}$. Analogous equations can readily be obtained for variations in charge asymmetry or other parameters.

One must first make explicit the dependence of $d^2w/d\Omega dU$ on η as follows:

$$\frac{d^2w(\mathbf{k}_\alpha, \mathbf{k}_{\alpha-1})}{dU_\alpha d\Omega_\alpha} d\mathbf{k}_{\alpha-1} \rightarrow \frac{d^3w(\mathbf{k}_\alpha, \eta_\alpha^{(A)}, \mathbf{k}_{\alpha-1}, \eta_{\alpha-1}^{(A)})}{dU_\alpha d\Omega_\alpha d\eta_\alpha^{(A)}} d\mathbf{k}_{\alpha-1} d\eta_{\alpha-1}^{(A)} \quad (6.34)$$

giving the probability that the system will undergo a transition from a momentum between $\mathbf{k}_{\alpha-1}$ and $\mathbf{k}_{\alpha-1} + d\mathbf{k}_{\alpha-1}$ and a mass parameter between $\eta_{\alpha-1}^{(A)}$ and $\eta_{\alpha-1}^{(A)} + d\eta_{\alpha-1}^{(A)}$ to \mathbf{k}_α and $\eta_\alpha^{(A)}$, respectively. Equation (6.1) is replaced by

$$\begin{aligned} \frac{d^3\sigma(\mathbf{k}_f, \eta_f^{(A)}, \mathbf{k}_i, \eta_i^{(A)})}{d\Omega_f dU_f d\eta_f^{(A)}} &= \sum_{m=\alpha \pm 1} \int \frac{d\mathbf{k}_1}{(2\pi)^3} d\eta_1 \cdots \int \frac{d\mathbf{k}_\alpha}{(2\pi)^3} d\eta_\alpha^{(A)} \left[\frac{d^3w_{m,\alpha}(\mathbf{k}_f, \eta_f^{(A)}, \mathbf{k}_\alpha, \eta_\alpha^{(A)})}{d\Omega_f dU_f d\eta_f^{(A)}} \right] \\ &\times \left[\frac{d^3w_{\alpha,\alpha-1}(\mathbf{k}_\alpha, \eta_\alpha^{(A)}, \mathbf{k}_{\alpha-1}, \eta_{\alpha-1}^{(A)})}{d\Omega_\alpha dU_\alpha d\eta_\alpha^{(A)}} \right] \cdots \left[\frac{d^3w_{2,1}(\mathbf{k}_2, \eta_2^{(A)}, \mathbf{k}_1, \eta_1^{(A)})}{d\Omega_2 dU_2 d\eta_1^{(A)}} \right] \\ &\times \left[\frac{d^2\sigma_{1i}(\mathbf{k}_1, \eta_1^{(A)}, \mathbf{k}_i, \eta_i^{(A)})}{d\Omega_1 dU_1 d\eta_1^{(A)}} \right] \end{aligned} \quad (6.35)$$

One now introduces the function $Y_\alpha(\mathbf{k}_\alpha, \eta_\alpha^{(A)})$ [see (6.4)]:

$$\begin{aligned} Y_\alpha(\mathbf{k}_\alpha, \eta_\alpha^{(A)}) &= \int \frac{d\mathbf{k}_1 d\eta_1}{(2\pi)^3} \cdots \int \frac{d\mathbf{k}_{\alpha-1} d\eta_{\alpha-1}}{(2\pi)^3} \frac{d^3w_{\alpha,\alpha-1}}{d\Omega_\alpha dU_\alpha d\eta_\alpha^{(A)}} \\ &\cdots \frac{d^3w_{2,1}}{d\Omega_2 dU_2 d\eta_2^{(A)}} \frac{d^3w_{1i}}{d\Omega_1 dU_1 d\eta_1^{(A)}} \end{aligned} \quad (6.36)$$

The differential cross section in terms of Y_α is

$$\frac{d^3\sigma(\mathbf{k}_f, \eta_f^{(A)}, \mathbf{k}_i, \eta_i^{(A)})}{d\Omega_f dU_f d\eta_f^{(A)}} = \frac{2\pi\mu}{\hbar^2 k_{i,m,v}} \sum \int \frac{d\mathbf{k}_v}{(2\pi)^3} d\eta_v^{(A)} \frac{d^3 w_{m,v}}{dU_f d\Omega_f d\eta_f^{(A)}} \quad (6.37)$$

The function Y_v satisfies the equation

$$Y_v(\mathbf{k}_v, \eta_v^{(A)}) = \int \frac{d\mathbf{k}_{v-1}}{(2\pi)^3} d\eta_{v-1} \frac{d^3 w_{v,v-1}(\mathbf{k}_v, \eta_v^{(A)}, \mathbf{k}_{v-1}, \eta_{v-1}^{(A)})}{dU_v d\Omega_v d\eta_v^{(A)}} Y_{v-1}(\mathbf{k}_{v-1}, \eta_{v-1}^{(A)}) \quad (6.38)$$

The assumption is made that the change in momentum and $\eta^{(A)}$ in the transition from stage $v-1$ to stage v is small. One may therefore expand $Y_{v-1}(\mathbf{k}_{v-1}, \eta_{v-1}^{(A)})$ in terms of $Y_{v-1}(\mathbf{k}_v, \eta_v^{(A)})$ as follows:

$$\begin{aligned} Y_v(\mathbf{k}_{v-1}, \eta_{v-1}^{(A)}) &= Y_{v-1}(\mathbf{k}_v, \eta_v^{(A)}) + (\mathbf{k}_{v-1} - \mathbf{k}_v) \cdot \nabla Y_{v-1} + (\eta_{v-1}^{(A)} - \eta_v^{(A)}) \frac{\partial Y_{v-1}}{\partial \eta_v^{(A)}} \\ &\quad + \frac{1}{2} \left[(\mathbf{k}_{v-1} - \mathbf{k}_v) \cdot \nabla + (\eta_{v-1}^{(A)} - \eta_v^{(A)}) \frac{\partial}{\partial \eta_v^{(A)}} \right]^2 Y_{v-1} \end{aligned}$$

Inserting this equation into (6.38) yields

$$\begin{aligned} Y_v(\mathbf{k}_v, \eta_v^{(A)}) &= W_v^{(00)} Y_{v-1}(\mathbf{k}_{v-1}, \eta_{v-1}^{(A)}) \\ &\quad + \left[\mathbf{W}_v^{(10)} \cdot \nabla Y_{v-1}(\mathbf{k}_v, \eta_v^{(A)}) + W_v^{(01)} \frac{\partial Y_{v-1}(\mathbf{k}_v, \eta_v^{(A)})}{\partial \eta_v^{(A)}} \right] \\ &\quad + \frac{1}{2} \sum_{a,b} W_{ab}^{(20)} \nabla_a \nabla_b Y_{v-1}(\mathbf{k}_v, \eta_v^{(A)}) \\ &\quad + \mathbf{W}_v^{(11)} \cdot \nabla \left(\frac{\partial Y_{v-1}}{\partial \eta_v^{(A)}} \right) + \frac{1}{2} W_v^{(02)} \frac{\partial^2 Y_{v-1}}{\partial \eta_v^{(A)2}} \end{aligned} \quad (6.39)$$

where the coefficients W are generalizations of (6.7). Reducing this equation follows the procedure described after (6.7). The function Z_v is introduced as before by

$$Z = \frac{Y_v}{f_v} \quad f_v = \prod_1^v W_\alpha^{(00)}(\mathbf{k}_\alpha, \eta_\alpha^{(A)})$$

Finally, the interaction time variable τ by

$$\tau = \sum_1^v \frac{1}{W_\alpha^{(00)}}$$

One finally obtains

$$\frac{\partial Z}{\partial \tau} = \frac{1}{f(\tau, \mathbf{k}, \eta^{(A)})} \left[\mathbf{w}^{(10)} \cdot \nabla (fZ) + w^{(01)} \frac{\partial (fZ)}{\partial \eta^{(A)}} + \frac{1}{2} \sum_{ab} w_{ab}^{(20)} \nabla_a \nabla_b (fZ) \right. \\ \left. + \mathbf{w}^{(11)} \cdot \nabla \frac{\partial (fZ)}{\partial \eta^{(A)}} + \frac{1}{2} w^{(02)} \frac{\partial^2 (fZ)}{\partial \eta^2} \right] \quad (6.40)$$

We again make the assumption that f is independent of \mathbf{k} and η^A so that (6.40) becomes

$$\frac{\partial Z}{\partial \tau} = \mathbf{w}^{(10)} \cdot \nabla Z + w^{(01)} \frac{\partial Z}{\partial \eta^{(A)}} + \frac{1}{2} \sum_{ab} w_{ab}^{(20)} \nabla_a \nabla_b Z \\ + \mathbf{w}^{(11)} \cdot \nabla \frac{\partial Z}{\partial \eta^{(A)}} + \frac{1}{2} w^{(02)} \frac{\partial^2 Z}{\partial \eta^{(A)2}} \quad (6.41)$$

One can now follow the procedure described after (6.13). We shall leave the discussion to the reader, the coupling between the \mathbf{k} and $\eta^{(A)}$ dependence being the new feature of interest.

We shall content ourselves with integrating both sides of (6.41) with respect to \mathbf{k} . Assuming that all the coefficients are independent of \mathbf{k} [compare with (6.17)], let

$$\zeta(\eta^{(A)}) \equiv \int Z d\mathbf{k} \quad (6.42)$$

Then

$$\frac{\partial \zeta}{\partial \tau} = w^{(01)} \frac{\partial \zeta}{\partial \eta^{(A)}} + \frac{1}{2} w^{(02)} \frac{\partial^2 \zeta}{\partial \eta^{(A)2}} \quad (6.43)$$

This equation can be integrated. Let

$$\eta' = \eta^{(A)} + w^{(01)} \tau \quad \tau' = \tau$$

Then

$$\frac{\partial \zeta}{\partial \tau'} + \frac{\partial \zeta}{\partial \eta'} w^{(01)} = w^{(01)} \frac{\partial \zeta}{\partial \eta'} + \frac{1}{2} w^{(02)} \frac{\partial^2 \zeta}{\partial \eta'^2}$$

or

$$\frac{\partial \zeta}{\partial \tau'} = \frac{1}{2} w^{(02)} \frac{\partial^2 \zeta}{\partial \eta'^2}$$

The solution has the one-dimensional form [see (6.15)]

$$\zeta(\eta^{(A)}, \tau) = \left(\frac{1}{2\pi w^{(02)}\tau} \right)^{1/2} e^{-[1/2\tau w^{(02)}](\eta^{(A)} + w^{(01)}\tau - \eta^{(A)}(0))^2} \tag{6.44}$$

where $\eta^{(A)}(0)$ is the initial value of $\eta^{(A)}$. The mass asymmetry is in this approximation a Gaussian whose center changes linearly with τ and whose width changes like $\tau^{1/2}$.

Returning to (6.37) for the cross section, and once again utilizing (6.24) and (6.25a), one obtains

$$\int d\mathbf{k}_f \frac{d^3\sigma(\mathbf{k}_f, \eta_f^{(A)}, \mathbf{k}_i, \eta_i^{(A)})}{d\Omega_f d\Omega_f d\eta_f^{(A)}} = \frac{4\pi\mu f_0 \bar{s}W^{(00)}}{\hbar^2 k'_i} \int_0^\infty \frac{d\tau e^{-\gamma\tau - [1/2\tau w^{(02)}](\eta^{(A)} + w^{(01)}\tau - \eta^{(A)})^2}}{(2\pi w^{(02)}\tau)^{3/2}}$$

The integral can be performed, yielding

$$\int d\mathbf{k}_f \frac{d^3\sigma(\mathbf{k}_f, \eta_f, \mathbf{k}_i, \eta_i)}{d\Omega_f dU_f d\eta_f^{(A)}} = \frac{4\sqrt{2\pi}\mu f_0 \bar{s}W^{(00)}}{\hbar^2 k_1 |\eta - \eta_0|} \times e^{-1/w^{(02)}[\sqrt{2\gamma w^{(02)} + (w^{(01)})^2}|\eta_f^{(A)} - \eta^{(A)}(0)| + w^{(01)}(\eta_f^{(A)} - \eta^{(A)}(0))} \tag{6.45}$$

The distribution is no longer symmetric about $\eta_f^{(A)} = \eta_0^{(A)}$, falling off less rapidly for $\eta_f^{(A)} < \eta^{(A)}(0)$ when $w^{(01)}$ is positive, and vice versa when it is negative.

7. THE LORENTZ, BOLTZMANN, UHLENBECK, AND UEHLING (LBUU) METHOD[‡]

This method for treating heavy-ion collisions is based on a classical (nonquantum) method, describing the motion of A particles, employed in kinetic theory [Huang (87)]. The Hamiltonian determining the many-body motion is taken to be

$$H = \sum_{i=1}^A \left[\frac{\mathbf{p}_i^2}{2m} + V(r_i) \right] + \sum_{i < j} v(|\mathbf{r}_i - \mathbf{r}_j|) \tag{7.1}$$

The potential V is the mean potential and v is the residual two-body potential.

One asks for the distribution function $f(\mathbf{r}_1, \mathbf{r}_2, \dots, \mathbf{r}_A; \mathbf{p}_1, \mathbf{p}_2 \dots \mathbf{p}_A, t)$, the number density for finding particle 1 at \mathbf{r}_1 with a momentum \mathbf{p}_1 , particle 2 at \mathbf{r}_2 with momentum \mathbf{p}_2 , and so on, at a time t . The one-particle distribution $f_1(\mathbf{r}_1; \mathbf{p}_1)$ defined as the number density at a time t for finding a particle at \mathbf{r}_1

[‡]Huang (87).

with momentum \mathbf{p}_1 is given by

$$f_1(\mathbf{r}_1; \mathbf{p}_1 t) = \int d\mathbf{r}_2 d\mathbf{p}_2 d\mathbf{r}_3 d\mathbf{p}_3 \cdots f(\mathbf{r}_1, \mathbf{r}_2, \mathbf{r}_3, \dots, \mathbf{r}_A; \mathbf{p}_1, \mathbf{p}_2, \mathbf{p}_3, \dots, \mathbf{p}_A; t) \quad (7.2)$$

The number density at a time for finding s particles at $\mathbf{r}_1, \mathbf{r}_2, \dots, \mathbf{r}_s$ with momenta $\mathbf{p}_1, \mathbf{p}_2, \dots, \mathbf{p}_s$ is

$$f_s(\mathbf{r}_1 \cdots \mathbf{r}_s; \mathbf{p}_1 \cdots \mathbf{p}_s; t) = \frac{(A-1)!}{(A-s)!} \int d\mathbf{r}_{s+1} \cdots d\mathbf{r}_A d\mathbf{p}_{s+1} \cdots d\mathbf{p}_A f(\mathbf{r}_1 \cdots \mathbf{r}_A; \mathbf{p}_1 \cdots \mathbf{p}_A; t) \quad (7.3)$$

The normalization of f is given by

$$\int d\mathbf{r}_1 \cdots d\mathbf{r}_A d\mathbf{p}_1 \cdots d\mathbf{p}_A f(\mathbf{r}_1 \cdots \mathbf{r}_A; \mathbf{p}_1 \cdots \mathbf{p}_A; t) = \int d\mathbf{r}_1 d\mathbf{p}_1 f_1(\mathbf{r}_1; \mathbf{p}_1; t) = A \quad (7.4)$$

The probability density ρ is obtained from the number density by division by A :

$$\rho(\mathbf{r}_1 \cdots \mathbf{r}_A; \mathbf{p}_1 \cdots \mathbf{p}_A; t) = \frac{1}{A} f(\mathbf{r}_1 \cdots \mathbf{r}_A; \mathbf{p}_1 \cdots \mathbf{p}_A; t) \quad (7.5)$$

The space defined by the vectors $\mathbf{r}_1 \cdots \mathbf{r}_A; \mathbf{p}_1 \cdots \mathbf{p}_A$ is referred to as *phase space*. Its dimension is $6A$. We will denote a vector with components $\mathbf{r}_1 \cdots \mathbf{p}_A$ by ζ , so that (7.4) reads

$$\int d\zeta f(\zeta, t) = A$$

Since ρ is a probability density, the average value of any function $O(\zeta)$ in phase space is given by

$$\langle O(\zeta) \rangle = \int d\zeta \rho(\zeta) O(\zeta)$$

Because the number of particles is conserved as a function of time, the density must satisfy the equation of continuity:

$$\frac{\partial \rho}{\partial t} + \text{div}(\rho \mathbf{v}_\zeta) = 0 \quad (7.6)$$

where v_ζ is the velocity in phase space with components $\dot{\mathbf{r}}_1, \dot{\mathbf{r}}_2, \dots, \dot{\mathbf{p}}_A$. The divergence is taken in the $6A$ -dimensional space. Using this equation and

Hamilton's equation, *Liouville's theorem*,

$$\frac{d\rho}{dt} = 0 \quad (7.7)$$

can be obtained. The proof follows. First note that

$$\frac{d\rho}{dt} = \frac{\partial\rho}{\partial t} + \nabla\rho \cdot \mathbf{v}_\zeta$$

From (7.6) we have

$$-\frac{\partial\rho}{\partial t} = \nabla\rho \cdot \mathbf{v}_\zeta + \rho \operatorname{div} \mathbf{v}_\zeta \quad (7.8)$$

where

$$\operatorname{div} \mathbf{v}_\zeta = \sum_i [(\nabla_r)_i \cdot \dot{\mathbf{r}}_i + (\nabla_p)_i \cdot \dot{\mathbf{p}}_i]$$

But

$$\mathbf{r}_i = (\nabla_p)_i H \quad \dot{\mathbf{p}}_i = -(\nabla_r)_i H$$

so that

$$\operatorname{div} \mathbf{v}_\zeta = 0 \quad (7.9)$$

The flow in phase space is like that of an incompressible fluid. Inserting this equation into (7.8) and the result in the equation for $d\rho/dt$ yields (7.7).

The Liouville theorem is the fundamental equation of kinetic theory. We shall return to it later. For the present we shall consider directly the equation satisfied by f_1 . Recall that $f_1(\mathbf{r}, \mathbf{p}) d\mathbf{r} d\mathbf{p}$ is the number of particles in $d\mathbf{r} d\mathbf{p}$ at \mathbf{r} and \mathbf{p} . The function f_1 changes with time because (1) as a consequence of their velocity, particles leave the volume $d\mathbf{r}$; (2) the particles are acted on by the mean field forces $(-\nabla V_i)$ changing their momenta; and (3) particles collide with each other as induced by $\Sigma(v|\mathbf{r}_i - \mathbf{r}_j|)$.

If there are no collisions, the points in a volume element $d\mathbf{p} d\mathbf{r}$ will simply move into another volume element located at $\mathbf{r} + \mathbf{v} dt$ and $\mathbf{p} - (\nabla_r V) dt$. The change in f_1 in a time dt will be written $(\partial f_1 / \partial t)_{\text{coll}}$. Therefore,

$$f_1(\mathbf{r} + \mathbf{v} dt, \mathbf{p} - (\nabla_r V) dt, t + dt) = f_1(\mathbf{r}, \mathbf{p}, t) + \left(\frac{\partial f_1}{\partial t} \right)_{\text{coll}} dt$$

or

$$\frac{\partial f_1}{\partial t} + \mathbf{v} \cdot \nabla_r f_1 - \nabla_r V \cdot \nabla_p f_1 = \left(\frac{\partial f_1}{\partial t} \right)_{\text{coll}} \quad (7.10)$$

We assume that only binary collisions are important. The effects of a collision will depend on the number of pairs in a volume element $d\mathbf{r}$ with momenta \mathbf{p}_1 and \mathbf{p}_2 in the volume $d\mathbf{p}_1 d\mathbf{p}_2$. Let this be $F(\mathbf{r}, \mathbf{p}_1, \mathbf{p}_2, t) d\mathbf{r} d\mathbf{p}_1 d\mathbf{p}_2$. The number of particles leaving $d\mathbf{r} d\mathbf{p}_1$ per unit time because of collisions is

$$d\mathbf{r} d\mathbf{p}_1 \int \int F(\mathbf{r}, \mathbf{p}_1, \mathbf{p}_2, t) dw(\mathbf{p}'_1, \mathbf{p}'_2; \mathbf{p}_1, \mathbf{p}_2) d\mathbf{p}_2 d\mathbf{p}'_2 \quad (7.11)$$

Here dw is the probability per unit time that a pair of particles with momenta \mathbf{p}_1 and \mathbf{p}_2 will, upon collision, acquire momenta \mathbf{p}'_1 and \mathbf{p}'_2 . Since we are interested only in the total number of particles leaving $d\mathbf{r} d\mathbf{p}_1$, we integrate over \mathbf{p}_2 and \mathbf{p}'_2 . The value of \mathbf{p}'_1 is given by energy and momentum conservation. The value of dw is

$$dw(\mathbf{p}'_1, \mathbf{p}'_2; \mathbf{p}_1, \mathbf{p}_2) = \frac{2\pi}{\hbar} j_i \rho(E') |\mathcal{T}(\mathbf{p}_1 \rightarrow \mathbf{p}'_1, \mathbf{p}_2 \rightarrow \mathbf{p}'_2)|^2 d\Omega' \quad (7.12)$$

where j_i is the magnitude of the incident current density, $|\mathbf{v}_1 - \mathbf{v}_2|$ and \mathcal{T} is the transition matrix. Inserting (7.12) into (7.11) yields

$$d\mathbf{r} d\mathbf{p}_1 \int \int F(\mathbf{r}, \mathbf{p}_1, \mathbf{p}_2, t) |\mathbf{v}_1 - \mathbf{v}_2| \frac{d\sigma}{d\Omega'}(\mathbf{p}_1 \rightarrow \mathbf{p}'_1, \mathbf{p}_2 \rightarrow \mathbf{p}'_2) d\mathbf{p}_2 d\Omega' \quad (7.13a)$$

Similarly, the number entering volume element $d\mathbf{r} d\mathbf{p}_1$ because of collisions is

$$d\mathbf{r} d\mathbf{p}_1 \int \int F(\mathbf{r}, \mathbf{p}'_1, \mathbf{p}'_2, t) |\mathbf{v}'_1 - \mathbf{v}'_2| \frac{d\sigma}{d\Omega}(\mathbf{p}'_1 \rightarrow \mathbf{p}_1, \mathbf{p}'_2 \rightarrow \mathbf{p}_2) d\mathbf{p}'_2 d\Omega \quad (7.13b)$$

Using detailed balance gives

$$|\mathcal{T}(\mathbf{p}_1 \rightarrow \mathbf{p}'_1, \mathbf{p}_2 \rightarrow \mathbf{p}'_2)|^2 = |\mathcal{T}(\mathbf{p}'_1 \rightarrow \mathbf{p}_1, \mathbf{p}'_2 \rightarrow \mathbf{p}_2)|^2$$

One may rewrite (7.13b) as follows:

$$d\mathbf{r} d\mathbf{p}_1 \int \int F(\mathbf{r}, \mathbf{p}'_1, \mathbf{p}'_2, t) |\mathbf{v}_1 - \mathbf{v}_2| \frac{d\sigma}{d\Omega'} d\mathbf{p}_2 d\Omega' \quad (7.14)$$

Combining (7.13a) and (7.13b) yields

$$\left(\frac{\partial f_1}{\partial t} \right)_{\text{coll}} = \int \int d\mathbf{p}_2 d\Omega' |\mathbf{v}_1 - \mathbf{v}_2| \frac{d\sigma}{d\Omega'} [F(\mathbf{r}, \mathbf{p}'_1, \mathbf{p}'_2, t) - F(\mathbf{r}, \mathbf{p}_1, \mathbf{p}_2, t)] \quad (7.15)$$

To obtain the Lorentz-Boltzmann equation, one further approximation is made.

It is assumed that the probability of particle 1 being at \mathbf{r} with momentum \mathbf{p} does not depend on the position or momentum of particle 2. Hence

$$F(\mathbf{r}, \mathbf{p}_1, \mathbf{p}_2, t) \approx f_1(\mathbf{r}, \mathbf{p}_1, t)f_1(\mathbf{r}, \mathbf{p}_2, t) \tag{7.15'}$$

Introducing this assumption into (7.15), one can now complete (7.10). One finds that

$$\frac{\partial f_1}{\partial t} + \mathbf{v} \cdot \nabla_{\mathbf{r}} f_1 - \nabla_{\mathbf{r}} V \cdot \nabla_{\mathbf{p}_1} f_1 = \int d\mathbf{p}_2 d\Omega' |\mathbf{v}_1 - \mathbf{v}_2| \frac{d\sigma}{d\Omega'} [f'_1 f'_2 - f_1 f_2] \tag{7.16}$$

where f'_2 is $f_1(\mathbf{r}, \mathbf{p}'_2, t)$, and so on. The values of \mathbf{p}_1 and \mathbf{p}'_2 on the right side of this equation are given by conservation of energy and momentum applied to the binary collision. Equation (7.16) is referred to as the *Lorentz-Boltzmann equation*. Because of assumption (7.15'), one expects it to be most useful for dilute systems. To improve upon (7.16) it is necessary to consider correlations, and therefore f_2 of (7.3), $s=2$ for correlations, and more generally, f_s for higher-order correlations. As we shall show, f_s coupled only to f_{s+1} , that is, f_1 to f_2 , f_2 to f_3 . This is a consequence of the assumption that the particle interaction potentials [see (7.1)] are two-body. This system of equations is called the BBGKY (Bogoliubov, Born, Green, Kirkwood, Yvon) hierarchy. We shall follow Huang (87) in developing these equations.

One begins with the Liouville theorem, (7.7):

$$\frac{\partial \rho}{\partial t} + \mathbf{v}_\zeta \cdot \nabla_{\mathbf{p}} \rho = 0 \tag{7.7}$$

In component form,

$$\begin{aligned} \mathbf{v}_\zeta \cdot \nabla_{\mathbf{p}} \rho &= \sum_i [\dot{\mathbf{r}}_i \cdot \nabla_{\mathbf{r}_i} \rho + \dot{\mathbf{p}}_i \cdot \nabla_{\mathbf{p}_i} \rho] \\ &= \sum_i [(\nabla_{\mathbf{p}_i} H) \cdot \nabla_{\mathbf{r}_i} - (\nabla_{\mathbf{r}_i} H) \cdot \nabla_{\mathbf{p}_i}] \rho \end{aligned}$$

Introducing H as given by (7.1), one obtains

$$\frac{\partial \rho}{\partial t} + \hat{h}_A \rho = 0 \tag{7.17}$$

where

$$\begin{aligned} \hat{h}_A &= \sum_i \left[\frac{\mathbf{p}_i}{m} \cdot \nabla_{\mathbf{r}_i} + \left\{ \mathbf{F}_i - \sum_{i \neq j} \nabla_{\mathbf{r}_i} v(|\mathbf{r}_i - \mathbf{r}_j|) \right\} \cdot \nabla_{\mathbf{p}_i} \right] \\ &\equiv \sum_i \hat{S}_i + \frac{1}{2} \sum_{i \neq j} \hat{P}_{ij} \end{aligned} \tag{7.18}$$

Here

$$\hat{S}_i \equiv \frac{\mathbf{P}_i \cdot \nabla_{\mathbf{r}_i} + \mathbf{F}_i}{m} \quad \mathbf{F}_i = -\nabla_{\mathbf{r}_i} V \quad (7.19)$$

and

$$\hat{P}_{ij} = \mathbf{K}_{ij} \cdot \nabla_{\mathbf{p}_i} + \mathbf{K}_{ji} \cdot \nabla_{\mathbf{p}_j} \quad \mathbf{K}_{ij} = -\nabla_{\mathbf{r}_i} v(|\mathbf{r}_i - \mathbf{r}_j|) \quad (7.20)$$

The distribution function f_s then satisfies

$$\frac{\partial f_s}{\partial t} = \frac{A!}{(A-s)!} \int d\zeta_{s+1} \frac{\partial \rho}{\partial t} = -\frac{A!}{(A-s)!} \int d\zeta_{s+1} \hat{h}_A \rho \quad (7.21)$$

where

$$d\zeta_{s+1} = d\mathbf{r}_{s+1} d\mathbf{r}_{s+2} \cdots d\mathbf{r}_A d\mathbf{p}_{s+1} d\mathbf{p}_{s+2} \cdots d\mathbf{p}_A$$

We now break up \hat{h}_A into terms that depend on ζ_1 to ζ_s and those that depend on ζ_{s+1} to ζ_A :

$$\hat{h}_A = \sum_{i=1} \hat{S}_i + \frac{1}{2} \sum_{i \neq j} \hat{P}_{ij} + \sum_{i=s+1}^A \hat{S}_i + \frac{1}{2} \sum_{i,j=s+1}^A \hat{P}_{ij} + \sum_{i=1}^s \sum_{j=s+1}^A \hat{P}_{ij}$$

This can be rewritten as

$$\hat{h}_A = \hat{h}_s + \hat{h}_{A-s} + \sum_{i=1}^s \sum_{j=s+1}^A \hat{P}_{ij} \quad (7.22)$$

Note that

$$\int d\zeta_{s+1} \hat{h}_{A-s} \rho = 0 \quad (7.23)$$

since \hat{h} involves momentum-dependent gradient operators linearly while \mathbf{K}_{ij} depends only on spatial coordinates. Equation (7.22) would not be correct if the two-body potential were velocity dependent.

Inserting (7.22) into (7.21) yields

$$\begin{aligned} \frac{\partial f_s}{\partial t} + \hat{h}_s f_s &= -\frac{A!}{(A-s)!} \int d\zeta_{s+1} \sum_{i=1}^s \sum_{j=s+1}^A \hat{P}_{ij} \rho \\ &= -\sum_{i=1}^s \iint d\mathbf{r}_{s+1} d\mathbf{p}_{s+1} \frac{A!}{(A-s-1)!} \hat{P}_{i,s+1} \int d\zeta_{s+2} \rho \\ &= -\iint d\mathbf{r}_{s+1} d\mathbf{p}_{s+1} \left(\sum_{i=1}^s \hat{P}_{i,s+1} \right) f_{s+1} \end{aligned} \quad (7.24)$$

Substituting for $\hat{P}_{i,s+1}$ from (7.20), one finally obtains the BBGKY hierarchy:

$$\frac{\partial f_s}{\partial t} + \hat{h}_s f_s = -\iint d\mathbf{r}_{s+1} d\mathbf{p}_{s+1} \left(\sum_{i=1}^s \mathbf{K}_{i,s+1} \cdot \nabla_{\mathbf{p}_i} f_{s+1} \right) \quad (7.25)$$

For example,

$$\frac{\partial f_1}{\partial t} + \hat{h}_1 f_1 = - \iint d\mathbf{r}_2 d\mathbf{p}_2 \mathbf{K}_{12} \cdot \nabla_{\mathbf{p}_1} f_2 \quad (7.26a)$$

$$\frac{\partial f_2}{\partial t} + \hat{h}_2 f_2 = - \iint d\mathbf{r}_3 d\mathbf{p}_3 (\mathbf{K}_{13} \cdot \nabla_{\mathbf{p}_{p+1}} + \mathbf{K}_{23} \cdot \nabla_{\mathbf{p}_2}) f_3 \quad (7.26b)$$

To obtain the Lorentz–Boltzmann equation (7.16), one truncates (7.25) by placing f_3 and $\partial f_2/\partial t = 0$. Finally, one assumes that $f_2(\mathbf{r}_1, \mathbf{p}_1, \mathbf{r}_2, \mathbf{p}_2)$ can be written as $f_1(\mathbf{r}_1, \mathbf{p}_1) f_2(\mathbf{r}_2, \mathbf{p}_2)$ thereby dropping two-body correlations.

The solutions of the Lorentz–Boltzmann satisfy conditions that follow from conservation laws such as conservation of mass, momentum, and energy satisfied in the two-body collision. Following Huang, let $\chi(\mathbf{r}, p)$ be such a conserved quantity, that is,

$$\chi(\mathbf{r}, \mathbf{p}_1) + \chi(\mathbf{r}, \mathbf{p}_2) = \chi(\mathbf{r}, \mathbf{p}'_1) + \chi(\mathbf{r}, \mathbf{p}'_2) \quad (7.27)$$

We can now show that

$$J = \iint \left(\frac{\partial f_1}{\partial t} \right)_{\text{coll}} \chi(\mathbf{r}, \mathbf{p}) d\mathbf{p} = 0 \quad (7.28)$$

We use expression (7.11), bearing in mind the symmetries satisfied by F and dw .

Equation (7.28), including now explicitly the conservation of energy and momentum, is

$$J = \int d\mathbf{p}_1 d\mathbf{p}_2 d\mathbf{p}'_1 d\mathbf{p}'_2 \delta(E_1 + E_2 - E'_1 - E'_2) \delta(\mathbf{p}_1 + \mathbf{p}_2 - \mathbf{p}'_1 - \mathbf{p}'_2) \\ \times w(\mathbf{p}'_1, \mathbf{p}'_2, \mathbf{p}_1, \mathbf{p}_2) [F(\mathbf{r}, \mathbf{p}'_1, \mathbf{p}'_2, t) - F(\mathbf{r}, \mathbf{p}_1, \mathbf{p}_2, t)] \chi(\mathbf{r}, \mathbf{p}_1)$$

Now we note that J is unchanged if under the integral spin we exchange \mathbf{p}_1 and \mathbf{p}_2 or \mathbf{p}_1 and \mathbf{p}'_1 together with the exchange of \mathbf{p}_2 and \mathbf{p}'_2 or if one exchanges \mathbf{p}_1 and \mathbf{p}'_2 together with \mathbf{p}_2 and \mathbf{p}'_1 . This result is a consequence of the symmetry of both w and F . Performing the exchanges and adding the results yields

$$J = \int d\mathbf{p}_1 d\mathbf{p}_2 d\mathbf{p}'_1 d\mathbf{p}'_2 \delta(E_1 + E_2 - E'_1 - E'_2) \delta(\mathbf{p}_1 + \mathbf{p}_2 - \mathbf{p}'_1 - \mathbf{p}'_2) \\ \times w(\mathbf{p}'_1, \mathbf{p}'_2, \mathbf{p}_1, \mathbf{p}_2) [F(\mathbf{r}, \mathbf{p}'_1, \mathbf{p}'_2, t) - F(\mathbf{r}, \mathbf{p}_1, \mathbf{p}_2, t)] \\ \times [\chi(\mathbf{r}, \mathbf{p}_1) + \chi(\mathbf{r}, \mathbf{p}_2) - \chi(\mathbf{r}, \mathbf{p}'_1) - \chi(\mathbf{r}, \mathbf{p}'_2)]$$

Hence because of conservation condition (7.27), $J = 0$, proving (7.28).

As a consequence of this equation, one obtains from the Lorentz–Boltzmann equation the equation

$$\int d\mathbf{p} \chi(\mathbf{r}, \mathbf{p}) \left[\frac{\partial f_1}{\partial t} + \sum_i \frac{\mathbf{p}_i}{m} \frac{\partial f_1}{\partial x_i} + F_i \frac{\partial f_1}{\partial p_i} \right] = 0 \quad (7.29)$$

where

$$F_i \equiv -\nabla_r U$$

We now rewrite this equation so that no derivatives act on f_1 under the integral sign. Thus

$$\begin{aligned} 0 = & \frac{\partial}{\partial t} \int d\mathbf{p} \chi f_1 + \sum \frac{\partial}{\partial x_i} \int d\mathbf{p} \frac{\mathbf{p}_i}{m} \chi f_1 - \sum_i \int d\mathbf{p} \left(\frac{\mathbf{p}_i}{m} \frac{\partial \chi}{\partial x_i} \right) f_1 \\ & + \sum F_1 \int d\mathbf{p} \frac{\partial(\chi f_1)}{\partial p_i} - \sum_i F_i \int d\mathbf{p} \left(\frac{\partial \chi}{\partial p_i} \right) f_1 \end{aligned} \quad (7.30)$$

Integrating the fourth term on the right yields zero. We introduce the definitions

$$\begin{aligned} \langle A \rangle & \equiv \frac{\int d\mathbf{p} A f_1}{\int d\mathbf{p} f_1} = \frac{1}{n} \int d\mathbf{p} A f_1 \\ \mathbf{v} & = \frac{1}{m} \mathbf{p} \end{aligned}$$

Note that n , the number of particle density, is a function of \mathbf{r} and t . Equation (7.30) becomes

$$0 = \frac{\partial}{\partial t} \langle n\chi \rangle + \nabla_r \cdot \langle n\mathbf{v}\chi \rangle = \langle n\mathbf{v} \cdot \nabla_r \chi \rangle - \left\langle \frac{n}{m} \mathbf{F} \cdot \nabla_v \chi \right\rangle \quad (7.31)$$

The functions n and \mathbf{F} can be removed from inside the brackets since they do not depend on \mathbf{p} .

For conservation of mass, $\chi = m$, (7.31) becomes the equation of continuity:

$$\frac{\partial n}{\partial t} + \nabla_r \cdot (n\mathbf{u}) = 0 \quad (7.32)$$

where

$$\mathbf{u} = \langle \mathbf{v} \rangle \quad (7.33)$$

For conservation of momentum, $\chi = m\mathbf{v}$,

$$0 = \frac{\partial}{\partial t} (n\mathbf{v}) + \nabla_r \cdot n \langle \mathbf{v}\mathbf{v} \rangle - \frac{1}{m} n\mathbf{F} \quad (7.34)$$

where the dot product in the second term is with the \mathbf{v} that immediately follows the dot. We now replace $\langle \mathbf{v}\mathbf{v} \rangle$ as follows:

$$\langle \mathbf{v}\mathbf{v} \rangle = \langle (\mathbf{v} - \mathbf{u})(\mathbf{v} - \mathbf{u}) \rangle + \mathbf{u}\mathbf{u}$$

Substituting in (7.26) and using (7.24), one obtains

$$n \left[\frac{\partial \mathbf{u}}{\partial t} + (\mathbf{u} \cdot \nabla) \mathbf{u} \right] = \frac{1}{m} n \mathbf{F} + \nabla \cdot n \langle (\mathbf{v} - \mathbf{u})(\mathbf{v} - \mathbf{u}) \rangle \quad (7.35)$$

The pressure tensor P_{ij} is defined by

$$P_{ij} \equiv mn \langle (v_i - u_i)(v_j - u_j) \rangle \quad (7.36)$$

so that

$$n \left[\frac{\partial \mathbf{u}}{\partial t} + (\mathbf{u} \cdot \nabla) \mathbf{u} \right] = \frac{1}{m} n \mathbf{F} + \frac{1}{m} \nabla \cdot \vec{P} \quad (7.37)$$

where

$$\nabla \cdot \vec{P} = \sum \frac{\partial P_{ij}}{\partial x_i}$$

Problem. Prove that this quantity is conserved in a two-body collision.

Finally, we exploit the conservation of energy by letting $\chi = \frac{1}{2} |\mathbf{v} - \mathbf{u}|^2$. The analysis is straightforward. The result is

$$n \frac{\partial T}{\partial t} + n \mathbf{u} \cdot \nabla_r T + \frac{2}{3} \nabla_r \cdot \mathbf{q} = - \frac{2}{3} \vec{P} \cdot \vec{\Lambda} \quad (7.38)$$

where

$$\vec{P} \cdot \vec{\Lambda} = \sum_{ij} P_{ij} \Lambda_{ij} \quad (7.39)$$

and

$$\Lambda_{ij} = \frac{1}{2} \left(\frac{\partial u_j}{\partial x_i} + \frac{\partial u_i}{\partial x_j} \right) \quad (7.40)$$

T is the temperature in energy units:

$$T = \frac{1}{3} \langle |\mathbf{v} - \mathbf{u}|^2 \rangle$$

The vector \mathbf{q} measures the heat flux:

$$\mathbf{q} = \frac{1}{2} n \langle (\mathbf{v} - \mathbf{u}) |\mathbf{v} - \mathbf{u}|^2 \rangle \quad (7.41)$$

The exploitation of (7.32), (7.37), and (7.38) requires evaluation of the average values indicated by the bracket and therefore knowledge of f_i . If, for example, one assumes local thermal equilibrium, so that f_1 is given locally by the Maxwell distribution,

$$f_1 \approx \frac{n}{(2\pi mT)^{3/2}} e^{-(m/2T)(\mathbf{v}-\mathbf{u})^2}$$

one obtains the equations describing nonviscous hydrodynamics. If f_1 is improved by a first-order term, one obtains the Navier–Stokes equation for viscous flow [see Huang (87)]. Therefore, the equations of hydrodynamics are an approximation to the Lorentz–Boltzmann equation obtained by averaging that equation over an assumed distribution function.

A. Quantum Transport[†]

The discussion above is classical so that the question of quantum effects naturally surfaces. Of course, the exact evaluation of the quantum effects requires the solution of the quantum-mechanical many-body problem. What would be useful would be a statement of the quantum problem, which is similar in form to the Lorentz–Boltzmann equation. The analog to the one-particle distribution function is given by one-particle Wigner function (30) defined by

$$f_w(\mathbf{r}, \mathbf{k}, t) = \left(\frac{1}{2\pi}\right)^3 \int d\mathbf{r}_0 e^{-i\mathbf{k}\cdot\mathbf{r}_0} \psi^*(\mathbf{r} - \frac{1}{2}\mathbf{r}_0, t) \psi(\mathbf{r} + \frac{1}{2}\mathbf{r}_0, t) \quad (7.42)$$

or

$$f_w(\mathbf{r}, \mathbf{k}, t) = \left(\frac{1}{2\pi}\right)^3 \int d\mathbf{r}_0 e^{-i\mathbf{k}\cdot\mathbf{r}_0} \rho\left(\mathbf{r} - \frac{1}{2}\mathbf{r}_0, \mathbf{r} + \frac{1}{2}\mathbf{r}_0, t\right) \quad (7.43)$$

Integrating f_w with respect to \mathbf{k} yields

$$\int f_w(\mathbf{r}, \mathbf{k}, t) d\mathbf{k} = \rho(\mathbf{r}, t) \quad (7.44)$$

Taking moments, one finds that

$$\begin{aligned} \int f_w(\mathbf{r}, \mathbf{k}, t) \mathbf{k} d\mathbf{k} &= \left(\frac{1}{2\pi}\right)^3 \int d\mathbf{k} \int d\mathbf{r}_0 i\nabla_0 e^{-i\mathbf{k}\cdot\mathbf{r}_0} \psi^*\left(\mathbf{r} - \frac{\mathbf{r}_0}{2}, t\right) \psi\left(\mathbf{r} + \frac{\mathbf{r}_0}{2}, t\right) \\ &= \left(\frac{1}{2\pi}\right)^3 \int d\mathbf{k} \int d\mathbf{r}_0 e^{-i\mathbf{k}\cdot\mathbf{r}_0} \left(\frac{1}{i} \nabla_0(\psi^*\psi)\right) \end{aligned}$$

[†]Carruthers and Zachariasen (83); Zachariasen (85).

$$= \left(\frac{1}{2\pi}\right)^3 \int d\mathbf{k} \int d\mathbf{r}_0 e^{-i\mathbf{k}\cdot\mathbf{r}_0} \left[-\frac{1}{2i} \left(\nabla\psi^* \left(\mathbf{r} - \frac{\mathbf{r}_0}{2}, t \right) \psi \left(\mathbf{r} + \frac{\mathbf{r}_0}{2}, t \right) \right) \right. \\ \left. + \frac{1}{2i} \psi^* \left(\mathbf{r} - \frac{\mathbf{r}_0}{2}, t \right) \nabla\psi \left(\mathbf{r} + \frac{\mathbf{r}_0}{2}, t \right) \right]$$

or

$$\int f_W(\mathbf{r}, \mathbf{k}, t) \frac{\mathbf{p}}{m} d\mathbf{k} = \mathbf{j}(\mathbf{r}, t) \quad (7.45)$$

Finally,

$$\int f_W(\mathbf{r}, \mathbf{k}, t) \frac{p^2}{2m} d\mathbf{k} = K(\mathbf{r}, t) \quad (7.46)$$

where $K(\mathbf{r}, t)$ is the kinetic energy density. [The reader should verify (7.46).] These results, (7.44), (7.45), and (7.46), are identical to those that can be obtained using the classical distribution function. But the Wigner distribution is not a probability distribution, as is the case for the classical distribution. This follows because f_W is not positive definite. Because of the close similarity to the Boltzmann distribution function, it is not surprising that f_W satisfies a Lorentz-Boltzmann type of equation. To demonstrate this, evaluate $\partial f_W/\partial t$ using the Schrödinger equation:

$$i\hbar \frac{\partial\psi}{\partial t} = H\psi \quad \text{and} \quad -i\hbar \frac{\partial\psi^*}{\partial t} = H\psi^*$$

assuming H to be Hermitian. One obtains

$$\frac{\partial f_W}{\partial t} = \left(\frac{1}{2\pi}\right)^3 \int d\mathbf{r}_0 e^{-i\mathbf{k}\cdot\mathbf{r}_0} \left[\left(\frac{i}{\hbar} H\psi^*\right)\psi - \frac{i}{\hbar} \psi^*(H\psi) \right]$$

Replace H by $-(\hbar^2/2m)\nabla^2 + V$, where ∇^2 operates on the dependence on the spatial coordinates $\mathbf{r} - \frac{1}{2}\mathbf{r}_0$ and $\mathbf{r} + \frac{1}{2}\mathbf{r}_0$. The result, after some simple algebra, is

$$\frac{\partial f_W}{\partial t} + \frac{\mathbf{p}}{m} \cdot \nabla_r f_W = -\frac{i}{\hbar} \int d\mathbf{r}_0 \psi^* \left[V \left(\mathbf{r} + \frac{\mathbf{r}_0}{2} \right) - V \left(\mathbf{r} - \frac{\mathbf{r}_0}{2} \right) \right] \psi e^{-i\mathbf{k}\cdot\mathbf{r}_0} \quad (7.47)$$

In the limit where V is assumed to be smooth, so that

$$V \left(\mathbf{r} + \frac{\mathbf{r}_0}{2} \right) \simeq V(\mathbf{r}) + \frac{\mathbf{r}_0}{2} \cdot \nabla V$$

(7.47) becomes

$$\frac{\partial f_W}{\partial t} + \frac{\mathbf{p}}{m} \cdot \nabla_r f_W - \nabla V \cdot \nabla_p f_W = 0 \quad (7.48)$$

identical with the Lorentz–Boltzmann equation (7.15) when the collision term $(\partial f/\partial t)_{\text{coll}}$ is zero. Equation (7.48) is known as the *Vlasov equation*.

This treatment can be generalized to the many-body problem, employing an A -particle Wigner distribution function [see Zachariassen (85)]

$$\begin{aligned} f_W^{(N)}(\mathbf{k}_1, \mathbf{r}_1, \mathbf{k}_2, \mathbf{r}_2, \dots, \mathbf{k}_A, \mathbf{r}_A, t) \\ = \left(\frac{1}{2\pi}\right)^{3A} \int d\mathbf{r}'_1 \cdots \int d\mathbf{r}'_A \exp(-i\sum \mathbf{k}_i \cdot \mathbf{r}'_i) \Psi^*(\mathbf{r}_1 - \frac{1}{2}\mathbf{r}'_1, \dots, \mathbf{r}_A - \frac{1}{2}\mathbf{r}'_A, t) \\ \cdot \Psi(\mathbf{r}_1 + \frac{1}{2}\mathbf{r}'_1, \dots, \mathbf{r}_A + \frac{1}{2}\mathbf{r}'_A, t) \end{aligned} \quad (7.49)$$

One can, in analogy with the procedure used to derive the BBGKY hierarchy, define reduced distribution functions $f_W^{(s)}$ by

$$f_W^{(s)} = (2\pi)^{3s} \int d\mathbf{r}_{s+1} \cdots \int d\mathbf{r}_A \int d\mathbf{k}_{s+1} \cdots \int d\mathbf{k}_A f_W^{(N)} \quad (7.50)$$

Applying the Schrödinger equation to (7.49), one finds a set of equations in which $f_W^{(s)}$ is coupled to $f_W^{(s+1)}$, the quantum analog of the BBGKY hierarchy. We shall not pursue this discussion further since as far as this author knows, no application of these quantum equations to heavy-ion reactions has been made.

B. Applications

Before it is possible to apply the Lorentz–Boltzmann equation to heavy-ion reactions it is necessary to take the Pauli principle into account. The necessary modification has been derived by Uehling and Uhlenbeck (33). Instead of (7.16), one obtains

$$\begin{aligned} \frac{\partial f_1}{\partial t} + \mathbf{v} \cdot \nabla_r f_1 - \nabla_r V \cdot \nabla_p f_1 \\ = \int d\mathbf{p}_1 d\Omega' |\mathbf{v}_1 - \mathbf{v}_2| \frac{d\sigma}{d\Omega} \{f'_1 f'_2 (1 - f_1)(1 - f_2) - f_1 f_2 (1 - f'_1)(1 - f'_2)\} \end{aligned} \quad (7.51)$$

The additional factors are intuitively obvious. Scattering out of \mathbf{p}'_1 and \mathbf{p}'_2 in \mathbf{p}_1 and \mathbf{p}_2 is not possible if the states \mathbf{p}_1 and \mathbf{p}_2 are occupied. Equation (7.51) is referred to as the Boltzmann–Uehling–Uhlenbeck equation (BUU).

Aichelin and Bertsch (85); Aichelin (86) [see also Kruse et al. (85) and Stöcker et al. (81)] have applied (7.51) to the study of heavy-ion reactions. [For additional references, see Aichelin (86).] Since the equation is classical, its use is limited to sufficiently high energies. At very high energies the intranuclear cascade model, discussed in Chapter IX, and to which (7.51) reduces, is appropriate. At low energies, where the Pauli blocking reduces the impact of

the collision term, one may use the time-dependent Hartree–Fock (TDHF) method, discussed in Section 8. Equation (7.51) applies when the collision term and/or the mean potential, V (which can be neglected at high energies), are significant. In their studies, Bertsch and Aichelin have investigated $^{12}\text{C} + ^{16}\text{O}$ at 25 MeV/A, $^{12}\text{C} + ^{12}\text{C}$ at 84 MeV/A, $^{16}\text{O} + ^{197}\text{Au}$ at 25 and 250 MeV/A, and $^{12}\text{C} + ^{197}\text{Au}$ at 84 MeV/A. The collisions with ^{197}Au are most important since one can study the progress toward equilibration, the possible presence of hot spots, and other local properties, such as density and local thermal equilibrium. One can also study the validity of the spectator model in which it is assumed that the reaction occurs only in the region where the projectile and target nuclei overlap.

Predictions can be made only for single-particle spectra and angular distribution. For the light nuclei, Coulomb effects are neglected, while for the heavy nuclear targets, Coulomb effects are neglected after the first nucleon–nucleon collision.

These authors find that the course of the reaction is determined by the relative importance of the mean field, the collision term, and the Pauli principle. At the

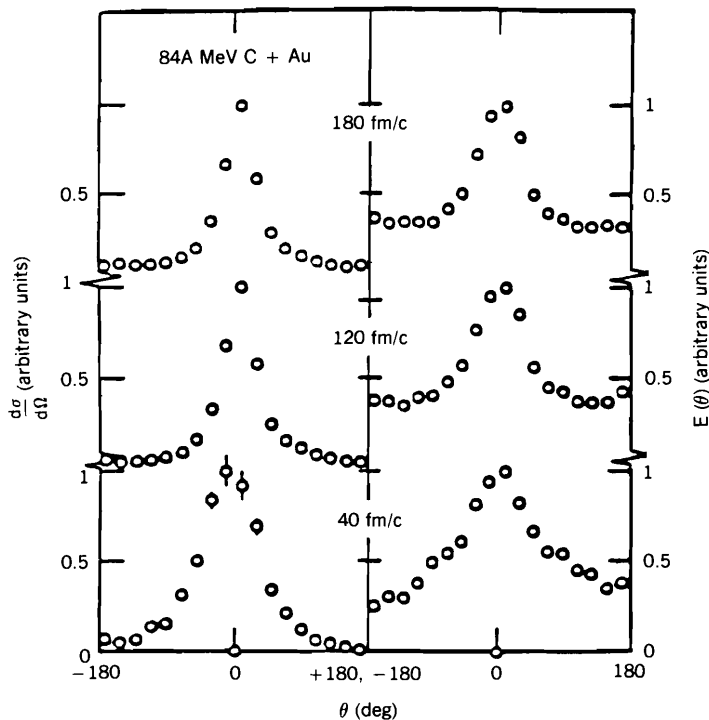


FIG. 7.1. Angular distribution and average kinetic of emitted protons as a function of time. Positive angles correspond to positive values of the x component of the momentum of the emitted particles. [From Aichelin (86).]

lower end of the energies considered, the mean field and the Pauli principle dominate. The nucleons of the incident projectile are more readily trapped by the mean field but have a longer mean free path. Fusion is the endpoint of the reaction. The single-particle spectrum is exponential but with a slope parameter increasing as a function of angle in agreement with the discussion in Section 6, which relies on a Fokker-Planck equation in the momentum space. At higher energies, 84 MeV/A, the multistep direct reaction as well the multistep compound reaction become significant. The reaction thus shows a substantial preequilibrium component which develops during the early stages of the reaction. The mean field does trap some particles, so that the final stages of the multistep compound leads to a final remnant compound nucleus which oscillates radially. The angular distribution consists of roughly two components. The preequilibrium reaction gives rise to a forward peaked anisotropic distribution, while the remnant compound nucleus will emit isotropically in the center of mass. At the highest energy considered, 250 MeV/A, the collision term dominates in the overlap region. However, these authors state that even at this energy a clear-cut separation between participant and spectator nucleons is not possible. The multistep direct reaction with its forward peaked angular

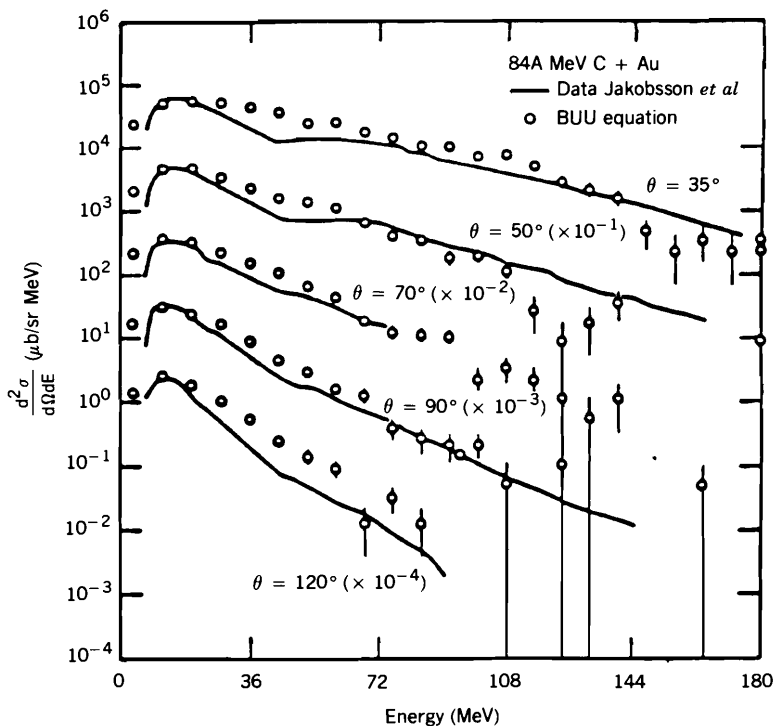


FIG. 7.2. Proton spectrum produced by the reaction $^{12}\text{C} + ^{197}\text{Au}$ at 84 MeV/A compared with the results of Jakobsson et al. (82). [from Aichelin (86).]

distribution is dominant, and even in the overlap region complete equilibrium is not achieved.

The predicted single-particle spectrum is compared with experiment (84 MeV/A) in Fig. 7.1. Substantial agreement (note that this is a semilog plot) is obtained. However, the slope parameter for the high-energy tails increases with angle, in agreement with the momentum space Fokker–Plank equation [see (6.31) et seq.] Correspondingly, the angular distribution is strongly anisotropic, indicating the dominant presence of multistep direct processes (see Fig. 7.2). A similar result prevails at 250 MeV/A. Equilibrium, which requires an isotropic distribution, is not attained. The author concludes that the hydrodynamic approach is not valid at 84 MeV/A, and this writer would add—probably not at 250 MeV/A.

8. TIME-DEPENDENT HARTREE–FOCK METHOD[‡]

The Lorentz–Boltzmann approach of Section 7 is not valid in the low-energy domain (energies $\simeq 10$ MeV/A). The Pauli principle and quantum effects must be treated carefully. Because of the Pauli blocking, the effect of collisions of a low-energy nucleon with the nucleons of the nucleus is strongly reduced, increasing the mean free path so that at 10 MeV it is on the order of the diameter of the nucleus. As many fewer nuclear states are involved, quantum effects become significant. However, it is just under this regime that the mean field approximation becomes valid. The nucleon is acted on by an average field generated by all the nucleons in the nucleus whose coordinates essentially disappear from the problem to be replaced by the parameters describing the mean field (e.g., the nuclear radius). The zeroth approximation to the mean field is the Hartree–Fock approximation. To improve upon it, one can use the time-dependent Hartree–Fock (TDHF), described in Section III.3 of deShalit and Feshbach (74). As shown there, for small deviations from the Hartree–Fock approximation, one obtains the RPA approximation [Thouless (61); Kerman and Koonin (76)]. However, in the case of heavy-ion collisions, we are concerned with relatively large deviations. The method to be used was first proposed by Dirac (30), and applied to large-amplitude dynamics and heavy-ion collisions by Kerman and Koonin (76) and Bonche, Koonin, and Negele (76) to a one-dimensional case.

We begin with a variation principle for the time-dependent many-body Schrödinger equation:

$$\delta S = 0 \tag{8.1}$$

[‡]Kerman and Koonin (76); Negele (82); Davies, Devi, Koonin, and Strayer (84); Pal (85).

where

$$S = \int dt \int d\mathbf{r}_1 \cdots d\mathbf{r}_n d\mathbf{r}'_1 \cdots d\mathbf{r}'_n \Psi^*(\mathbf{r}_1 \cdots \mathbf{r}_n, t) \cdot \left[i\hbar \frac{\partial}{\partial t} - H(\mathbf{r}_1 \cdots \mathbf{r}_n; \mathbf{r}'_1 \cdots \mathbf{r}'_n) \right] \Psi(\mathbf{r}'_1 \cdots \mathbf{r}'_n, t) \quad (8.2)$$

Varying Ψ^* yields the time-dependent Schrödinger equation for Ψ . The trial function to be used in TDHF is a time-dependent Slater determinant:

$$\psi_{SD} = \frac{1}{\sqrt{n!}} \begin{vmatrix} \psi_1(\mathbf{r}_1, t) & \psi_1(\mathbf{r}_2, t) & \cdots & \psi_1(\mathbf{r}_n, t) \\ \psi_2(\mathbf{r}_1, t) & \psi_2(\mathbf{r}_2, t) & \cdots & \psi_2(\mathbf{r}_n, t) \\ \vdots & \vdots & \ddots & \vdots \\ \psi_n(\mathbf{r}_1, t) & \psi_n(\mathbf{r}_2, t) & \cdots & \psi_n(\mathbf{r}_n, t) \end{vmatrix} \quad (8.3)$$

where the trial single-particle wave functions are orthonormal:

$$\langle \psi_\mu(\mathbf{r}, t) | \psi_\nu(\mathbf{r}, t) \rangle = \delta_{\mu\nu} \quad (8.4)$$

Inserting Ψ_{SD} for Ψ in (8.2) and varying with respect to ψ_ν^* yields the one-body equation for ψ_ν :

$$i\hbar \frac{\partial \psi_\nu}{\partial t} = T\psi_\nu + \sum_\mu \int d\mathbf{r}_2 d\mathbf{r}'_1 d\mathbf{r}'_2 \psi_\mu^*(\mathbf{r}_2, t) \tilde{v}(\mathbf{r}_1, \mathbf{r}_2; \mathbf{r}'_1, \mathbf{r}'_2) \psi_\mu(\mathbf{r}'_2, t) \psi_\nu(\mathbf{r}'_1, t) \\ \equiv (T + V)\psi_\nu \quad (8.5)$$

In this equation, T is the kinetic energy operator. We have assumed that the potential v in H is two-body operator:

$$v(\mathbf{r}_1 \cdots \mathbf{r}_n, \mathbf{r}'_1 \cdots \mathbf{r}'_n) = v(\mathbf{r}_i, \mathbf{r}_j; \mathbf{r}'_i, \mathbf{r}'_j) \delta(\mathbf{r}_1 - \mathbf{r}'_1) \cdots \delta(\mathbf{r}_{i-1} - \mathbf{r}'_{i-1}) \delta(\mathbf{r}_{i+1} - \mathbf{r}'_{i+1}) \cdots \\ \delta(\mathbf{r}_{j-1} - \mathbf{r}'_{j-1}) \delta(\mathbf{r}_{j+1} - \mathbf{r}'_{j+1}) \cdots \delta(\mathbf{r}_n - \mathbf{r}'_n).$$

The quantity \tilde{v} in (8.5) is then

$$\tilde{v}(\mathbf{r}_1, \mathbf{r}_2; \mathbf{r}'_1, \mathbf{r}'_2) \equiv v(\mathbf{r}_1, \mathbf{r}_2; \mathbf{r}'_1, \mathbf{r}'_2) - v(\mathbf{r}_1, \mathbf{r}_2; \mathbf{r}'_2, \mathbf{r}'_1) \quad (8.6)$$

Equation (8.5) yields a set of coupled nonlinear equations whose solutions give the time and spatial dependence of the single-particle wave function $\psi_\nu(\mathbf{r}, t)$. The time-independent Hartree-Fock equations are obtained by assuming that each particle wave function has an exponential dependence on time. Note that when v satisfies translational invariance, that is,

$$v(\mathbf{r}_1, \mathbf{r}_2; \mathbf{r}'_1, \mathbf{r}'_2) = \delta(\mathbf{r}_1 - \mathbf{r}'_1) \delta(\mathbf{r}_2 - \mathbf{r}'_2) v(\mathbf{r}_1 - \mathbf{r}_2)$$

then

$$\tilde{v} = [\delta(\mathbf{r}_1 - \mathbf{r}'_1)\delta(\mathbf{r}_2 - \mathbf{r}'_2) - \delta(\mathbf{r}_1 - \mathbf{r}'_2)\delta(\mathbf{r}_2 - \mathbf{r}'_1)]v(\mathbf{r}_1 - \mathbf{r}_2)$$

Equation (8.5) becomes

$$i\frac{\partial\psi_v}{\partial t} = T\psi_v + \sum_{\mu} \int d\mathbf{r}_2 [\psi_{\mu}^*(\mathbf{r}_2)\psi_{\mu}(\mathbf{r}_2)\psi_v(\mathbf{r}_1) - \psi_{\mu}^*(\mathbf{r}_2)\psi_{\mu}(\mathbf{r}_1)\psi_v(\mathbf{r}_2)]v(\mathbf{r}_1 - \mathbf{r}_2) \quad (8.7)$$

The first term in brackets is the direct or Hartree term, the second term is the exchange or Fock term. The direct term is local, while the exchange term is nonlocal.

The trial function, Ψ_{SD} , will not provide a complete description of the nuclear state no matter how accurately (8.5) is solved, as only the correlations induced by the Pauli exclusion principle are present. The correlations induced by the potential v are not. As a consequence, one can expect that the matrix elements of only single-body operators will be given accurately using Ψ_{SD} . It would not be correct to use Ψ_{SD} to evaluate matrix elements of two- (or more) body operators.

The TDHF equations (8.5) imply a number of conservation laws. One asserts that the orthonormal condition (8.4) holds at all times t . To prove this, consider

$$\frac{d}{dt} \int d\mathbf{r} \psi_v^*(\mathbf{r}, t)\psi_{\mu}(\mathbf{r}, t) = \int d\mathbf{r} \left(\frac{\partial}{\partial t} \psi_v^* \psi_{\mu} + \psi_v^* \frac{\partial \psi_{\mu}}{\partial t} \right)$$

Substituting from (8.5), one obtains

$$\frac{d}{dt} \int d\mathbf{r} \psi_v^*(\mathbf{r}, t)\psi_{\mu}(\mathbf{r}, t) = -\frac{i}{\hbar} \int d\mathbf{r} [\psi_v^*(T + V)\psi_{\mu} - \psi_v^*(T + V)\psi_{\mu}] = 0$$

The expectation value of any one-body operator that commutes with H is conserved [Koonin (79)]. To prove this, we calculate

$$\frac{d}{dt} \langle \psi_{SD} \hat{O} \psi_{SD} \rangle = \sum_{\nu} \int d\mathbf{r} d\mathbf{r}' \left[\frac{\partial \psi_{\nu}^*(\mathbf{r}, t)}{\partial t} \hat{O}(\mathbf{r}, \mathbf{r}') \psi_{\nu}(\mathbf{r}', t) + \psi_{\nu}^*(\mathbf{r}, t) \hat{O}(\mathbf{r}, \mathbf{r}') \frac{\partial \psi_{\nu}(\mathbf{r}', t)}{\partial t} \right]$$

Replacing the time derivatives by the right-hand side of (8.5) yields

$$\frac{d}{dt} \langle \Psi_{SD} \hat{O} \Psi_{SD} \rangle = \frac{i}{\hbar} \sum_{\nu} \int d\mathbf{r} d\mathbf{r}' [\psi_{\nu}^*(\mathbf{r}, t) (\hat{O} \mathcal{H} - \mathcal{H} \hat{O}) \psi_{\nu}(\mathbf{r}', t)]$$

where

$$\mathcal{H} \equiv T + V$$

The proof is completed by replacing V by its definition in (8.5). Quantities that are conserved include the expectation value of \mathcal{H} , the TDHF energy, the expectation value of the total momentum, and the total angular momentum.

The time-dependent Hartree-Fock equations can be reexpressed in a representation-independent form using the density matrix $\rho(\mathbf{r}, \mathbf{r}', t)$, where

$$\rho(\mathbf{r}_1 \mathbf{r}'; t) = n \int \Psi^*(\mathbf{r}, \mathbf{r}_2, \dots, t) \Psi(\mathbf{r}', \mathbf{r}_2, \dots, t) d\mathbf{r}_2 \dots \quad (8.8)$$

The expectation of a one-body operator $\sum_i \hat{O}(\mathbf{r}_i, \mathbf{r}_i)$ is

$$\langle \Psi^* \hat{O} \Psi \rangle = \int \hat{O}(\mathbf{r}', \mathbf{r}) \rho(\mathbf{r}, \mathbf{r}', t) d\mathbf{r} d\mathbf{r}' = \text{tr } \hat{O} \rho \quad (8.9)$$

where the trace is taken with respect to the spatial coordinates. We note another property of ρ using determinantal wave functions, (8.3), for Ψ . In that case

$$\rho(\mathbf{r}, \mathbf{r}'; t) = \sum_{\mu} \psi_{\mu}(\mathbf{r}, t) \psi_{\mu}^*(\mathbf{r}', t) \quad (8.10)$$

and

$$\int \rho(\mathbf{r}, \mathbf{r}'; t) \rho(\mathbf{r}', \mathbf{r}''; t) d\mathbf{r}' = \rho(\mathbf{r}, \mathbf{r}''; t) \quad (8.11)$$

Or in operator language,

$$\hat{\rho}^2 = \hat{\rho} \quad (8.12)$$

In terms of ρ , (8.7) becomes

$$\begin{aligned} i\hbar \frac{\partial \psi_v}{\partial t} &= T \psi_v + \int d\mathbf{r}_2 \rho(\mathbf{r}_2, \mathbf{r}_2; t) v(\mathbf{r}_1 - \mathbf{r}_2) \psi_v(\mathbf{r}_1, t) \\ &\quad - \int d\mathbf{r}_2 \rho(\mathbf{r}_1, \mathbf{r}_2; t) v(\mathbf{r}_1 - \mathbf{r}_2) \psi_v(\mathbf{r}_2) \end{aligned} \quad (8.13)$$

which we abbreviate as follows:

$$i\hbar \frac{\partial \psi_v}{\partial t} = \int h(\mathbf{r}_1, \mathbf{r}_2; t) \psi_v(\mathbf{r}_2) d\mathbf{r}_2 \quad (8.14)$$

It is now possible to derive the equation of motion for ρ using the representation (8.10). One obtains

$$i\hbar \frac{\partial \rho}{\partial t} = \int d\mathbf{r}_2 [h(\mathbf{r}, \mathbf{r}_2, t) \rho(\mathbf{r}_2, \mathbf{r}', t) - \rho(\mathbf{r}, \mathbf{r}_2, t) h(\mathbf{r}_2, \mathbf{r}', t)] \quad (8.15)$$

Equation (8.15) can be written

$$i\hbar \frac{\partial \rho}{\partial t} = [h, \rho] \quad (8.16)$$

The one-body Hamiltonian, h , depends on ρ , so that (8.15) is nonlinear, as is the equation for ψ_v .

Equations (8.12) and (8.16) are the starting points for Baranger and Vereroni's (78) formulation of the adiabatic limit to TDHF. These authors point out that

$$\rho = e^{i\chi} \rho_0 e^{-i\chi} \quad (8.17)$$

satisfies (8.12), where ρ_0 is time even and satisfies $\rho_0^2 = \rho_0$. When χ is sufficiently small, ρ may be expanded in a power series in terms of the odd and even components of ρ . The equations relating them is obtained from (8.16). By constraining ρ_0 to be time even, the odd-time dependence is given by χ .

We return to the TDHF single-particle equation (8.5). To complete the description of this equation, one needs to specify the interaction potential, \tilde{v} , and the initial conditions. Integration of these equations is a very large task, so that one seeks to minimize the labor involved subject to the condition that no essential physics be lost. In this case, one selects a \tilde{v} that leads to local mean field, V , in (8.15). Toward this end one starts with the Skyrme potential [see Eq. (VII.18.24) in deShalit and Feshbach (74)] which leads to (VII.18.29) in the same reference for the single-particle Hamiltonian $H(\mathbf{r})$. Most of the calculations do not keep the spin-orbit terms, while the terms in the gradient of the density are replaced by a Yukawa-type interaction. The exchange properties of the last are chosen so that the resulting potential is local. Finally, one notes that (VII.18.29) of deShalit and Feshbach (74) is correct only for a stationary system such as the ground state. For moving system, (VII.18.29) of the same reference is written in a Galilean invariant form. This means that terms like ρT , where T is the kinetic energy density $\sum |\nabla \psi_v|^2$, are replaced by $\rho T - J^2$ where,

$$\mathbf{J} = \sum_v \text{Im} [\psi_v^* \nabla \psi_v] \quad (8.18)$$

The resulting single-particle Hamiltonian is

$$\begin{aligned} H = \int H(\mathbf{r}) d(\mathbf{r}) = \int d(\mathbf{r}) \left\{ \frac{\hbar^2}{2m} (T_n + T_p) + \frac{1}{2} t_0 [(2 + x_0) \rho_n \rho_p + \frac{1}{2} (1 - x_0) (\rho_n^2 + \rho_p^2)] \right. \\ \left. + \frac{1}{4} (t_1 + t_2) [(\rho_n + \rho_p)(T_n + T_p) - (\mathbf{J}_n + \mathbf{J}_p)^2] \right. \\ \left. + \frac{1}{8} (t_2 - t_1) [\rho_n T_n - J_n^2 + \rho_p T_p - J_p^2] + \frac{1}{4} t_3 (\rho_n \rho_p^2 + \rho_p \rho_n^2) \right\} \\ + \frac{1}{2} v_L [E_y(\rho_n, \rho_n) + E_y(\rho_p, \rho_p)] + v_u E_y(\rho_n, \rho_p) + C(\rho_p, \rho_p) \quad (8.19) \end{aligned}$$

TABLE 8.1 Parameters of the Effective Hamiltonian Density [Eq. (8.19)]

	SK II	SK III	Local
$t_0(\text{MeV}\cdot\text{fm}^3)$	-104.49	-333.47	-497.726
x_0	4.01	1.743	0
$t_1(\text{MeV}\cdot\text{fm}^5)$	585.6	395.6	0
$t_2(\text{MeV}\cdot\text{fm}^5)$	-27.1	-95.0	0
$t_3(\text{MeV}\cdot\text{fm}^6)$	9331.0	14,000.0	17,270.0
$v_L(\text{MeV})$	-444.85	-355.79	-363.044
$v_u(\text{MeV})$	-868.63	-619.60	-363.044
$\mu(\text{fm}^{-1})$	2.175	2.175	2.175
m^*/m	0.58	0.76	1

Source: Negele (82).

The quantities E_y and C are defined as follows:

$$E_y(\rho_a, \rho_b) = \iint d\mathbf{r} d\mathbf{r}' \frac{e^{-\mu|\mathbf{r}-\mathbf{r}'|}}{|\mathbf{r}-\mathbf{r}'|} \rho_a(\mathbf{r})\rho_b(\mathbf{r}') \quad (8.20)$$

$$C(\rho_p, \rho_p) = \frac{1}{2}e^2 \iint d\mathbf{r} d\mathbf{r}' \frac{\rho_p(\mathbf{r})\rho_p(\mathbf{r}')}{|\mathbf{r}-\mathbf{r}'|}$$

The parameters of this Hamiltonian are to $t_0, t_1, t_2, t_3, v_L, v_u,$ and μ . The parameters [see discussion in deShalit and Feshbach (74, p. 626)] are fixed by the volume, surface, symmetry energies, and the value of the effective mass, m^* . The value of the parameters are listed in Table 8.1 for these variants of the Skyrme potential.

The Hamiltonian governing the evolution of the single-particle wave function will have the form [see (VII.18.33) in deShalit and Feshbach (74)]

$$-\nabla \cdot \frac{\hbar^2}{2m^*} \nabla + U(\mathbf{r}) + \frac{1}{2i} (\mathbf{V} \cdot \mathbf{I} + \mathbf{I} \cdot \mathbf{V})$$

where m^* , U , and \mathbf{I} depend on the densities and currents present in (8.19). A list of the calculations done with each of the forces above is given by Negele (82).

We turn next to the initial conditions obtained when the ions are far apart. Each ion is described by a Slater determinant. The single-particle wave functions are given by solutions of the Hartree-Fock equations boosted to the initial velocity of the ion. If the solutions of the Hartree-Fock equations are $\psi_v^0(\mathbf{r})$ with energy ε_v , the boosted initial wave function is

$$\psi_v^{(i)}(\mathbf{r}, t) = e^{-i\hbar(\varepsilon_v + E/A)t} e^{i(\mathbf{K}/A) \cdot \mathbf{r}} \psi_v^{(0)}(\mathbf{r} - \mathbf{v}t) \quad (8.21)$$

where E is the kinetic energy of the ion and $\hbar\mathbf{K}$ is its momentum. The density matrix and potential energy transform as follows:

$$\rho^{(i)}(\mathbf{r}, \mathbf{r}', t) = e^{i\mathbf{K}/A \cdot (\mathbf{r} - \mathbf{r}')} \rho^{(0)}(\mathbf{r} - \mathbf{v}t, \mathbf{r}' - \mathbf{v}t) \quad (8.22a)$$

and

$$V^{(i)}(\mathbf{r}, \mathbf{r}', t) = e^{i\mathbf{K}/A \cdot (\mathbf{r} - \mathbf{r}')} V^{(0)}(\mathbf{r} - \mathbf{v}t, \mathbf{r}' - \mathbf{v}t) \quad (8.22b)$$

The Slater determinant formed using $\psi_v^{(i)}$ cannot be factorized into a wave function, depending only on the center-of-mass coordinate and a wave function, depending only on coordinates relative to the center of mass, \mathbf{R} . The latter wave function will also depend on \mathbf{R} . However, it vanishes when \mathbf{R} is outside the ion. Therefore, one is dealing with a center-of-mass wave packet $2R$ in diameter, where R is the nuclear radius. The corresponding spread in the center-of-mass momentum is

$$\Delta p_{\text{cm}} = \frac{\hbar}{2R}$$

and the spread in energy is

$$\frac{\Delta E}{E} = \frac{\hbar}{R(2mAE)^{1/2}}$$

For an oxygen beam whose energy is $2 \text{ MeV}/A$, $\Delta E/E = 0.07$, suggesting that the results of the TDHF approximation for light projectiles has a limited validity.

A. Collision of Semi-infinite Slabs

The collision of two semi-infinite slabs of finite thickness permits great calculational simplifications. In addition, slab collisions permit a clear-cut study of the behavior of the longitudinal degrees of freedom. This is especially instructive because in the fully three-dimensional collisions the coupling between longitudinal and transverse motion proves to be weak.

The single-particle wave functions are of the form $f(x, y)\phi_n(z, t)\chi_{\tau\sigma}$, where χ is a spin-isospin wave function. When $f(x, y)$ is a plane wave, $\exp(i\mathbf{k}_\perp \cdot \mathbf{r})$, where $\hbar\mathbf{k}_\perp$ is the transverse momentum, the function, $\phi_n(z, t)$ satisfies, as indicated, a one-dimensional time-dependent Schrödinger equation. The interaction potential $v(\mathbf{r}, \mathbf{r}')$ is given by

$$v(\mathbf{r}, \mathbf{r}') = t_0 \delta(\mathbf{r} - \mathbf{r}') + \frac{1}{6} t_3 \delta(\mathbf{r} - \mathbf{r}') \rho(\mathbf{r}) + V_0 \frac{e^{-\mu|\mathbf{r} - \mathbf{r}'|}}{\mu|\mathbf{r} - \mathbf{r}'|} \left(\frac{16}{15} + \frac{4}{15} P_x \right) \quad (8.23)$$

where P_x is the space-exchange operator. The combination $(\frac{16}{15} + \frac{4}{15} P_x)$ is chosen

so that the resulting mean field, $V(z, t)$, is local and has no spin or isospin dependence. Substituting in (8.4) yields

$$V(z, t) = \frac{3}{4}t_0\rho(z, t) + \frac{3}{16}t_3\rho^2(z, t) + 2\pi \frac{V_0}{\mu^3} \int_{-\infty}^{\infty} dz' \rho(z', t) e^{-\mu|z-z'|} \quad (8.24)$$

and

$$i\hbar \frac{\partial \phi_n}{\partial t} = -\frac{\hbar^2}{2m} \frac{\partial^2 \phi_n}{\partial z^2} + V(z, t)\phi_n \quad (8.25)$$

Initially ($t = 0$, not boosted), ϕ_n is the self-consistent Hartree-Fock solution of

$$\epsilon_n \phi_n^{(0)} = -\frac{\hbar^2}{2m} \frac{d^2}{dz^2} \phi_n^{(0)} + V(z)\phi_n^{(0)} \quad (8.26)$$

To complete (8.25) and (8.26) an expression for $\rho(z, t)$ in terms of ϕ_n is needed.

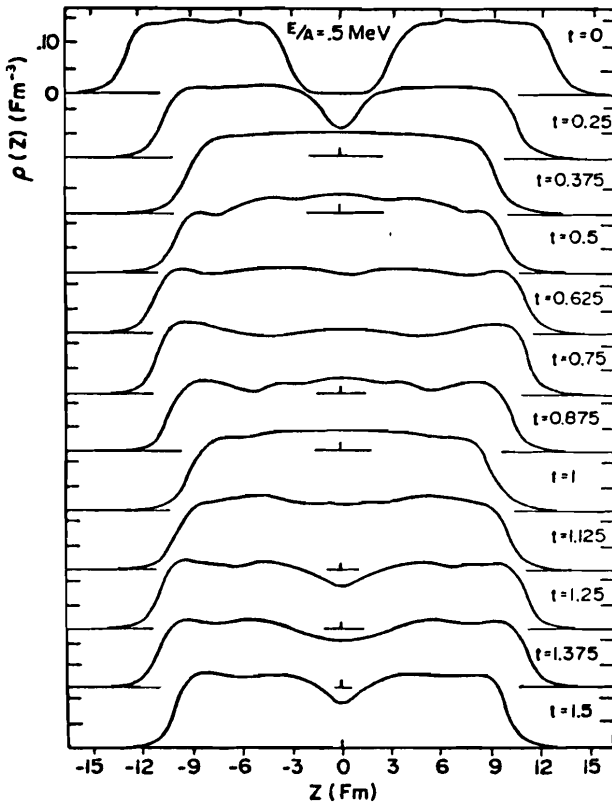


FIG. 8.1. Density distributions for $E/A = 0.5$ MeV [From Negele (78).]

We begin with (8.10). Initially [not boosted; see (8.22)],

$$\rho^{(0)}(z) = \sum |\psi_{\mu}^{(0)}(\mathbf{r}, t)|^2 = 4 \sum_n \int \frac{d\mathbf{k}_{\perp}}{(2\pi)^3} \rho(\mathbf{k}_{\perp}) |\phi_n^{(0)}(z)|^2$$

The integration on \mathbf{k}_{\perp} covers the range from ε_n to ε_F , the Fermi energy, with the result

$$\rho^{(0)}(z) = \sum_n A_n |\phi_n^{(0)}(z)|^2 \quad (8.27)$$

where

$$A_n = \frac{2m}{\pi\hbar^2} (\varepsilon_F - \varepsilon_n) \quad (8.28)$$

Since there is no coupling between the transverse and longitudinal modes, $\rho(z, t)$,

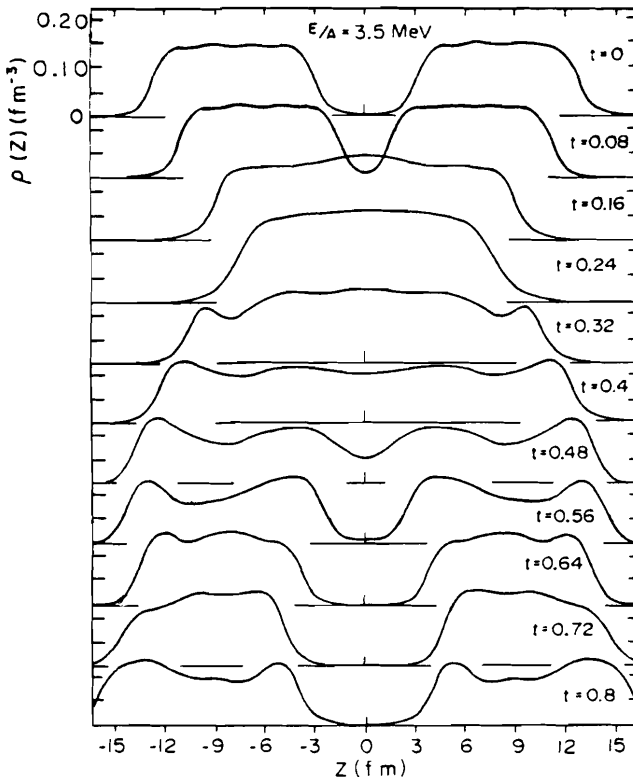


FIG. 8.2. Density profiles $\rho(z, t)$ at sequential times t , specified in units of 10^{-21} s, for a cm energy $E/A = 3.5$ MeV. [From Negele (82).]

as needed for the calculation of $V(z, t)$, (8.24), is

$$\rho(z, t) = \sum A_n |\phi_n(z, t)|^2 \quad (8.29)$$

The initial conditions are obtained by boosting the wave functions appropriately [see (8.21) et seq.]. The solutions are obtained by numerical integration of (8.25) using (8.29). In the calculations to be reported below, the constants used are taken from the "local" column in Table 8.1. These yield a nuclear matter density of 15.77 MeV per particle at $k_F = 1.29 \text{ fm}^{-1}$.

Figures 8.1, 8.2, and 8.3 give the density profiles as a function of time for the incident energies 0.5, 3.5 and 25 MeV/A. In the first (Fig. 8.1), fusion is indicated. In Fig. 8.2 the two slab pass through each other, but the final states of both systems are highly excited. In the high-energy case, fragmentation occurs. A detailed examination of these examples reveals two phenomena: (1) because the collision modifies the relative phases, the original coherence of the single-particle wave functions is destroyed; and (2) strong dissipation occurs. The second is related to the first since the destruction of the coherence characteristic of the ground state leads inevitably to excitation, so that some of the initial kinetic energy is converted into excitation energy. The large loss of kinetic energy is shown in Fig. 8.4. There are some energies, for example, near $E/A = 2 \text{ MeV}$, for which the energy loss is reduced. The loss of coherence occurs because the changing mean field affects each single-particle wave function differently, as can be seen from Fig. 8.5. Importantly, one sees that although two-body collisions are not included, the variety of phenomena, especially the large dissipation observed in heavy-ion collisions, is reproduced by the TDHF.

B. Collision of Realistic Systems

The integration of the time-dependent single-particle equations obtained from (8.19) by varying ψ_v^* is a formidable task. One must keep track of $(A_1 + A_2)$ complex numbers in a $(3 + 1)$ -dimensional space. Simplifications in addition to those already described are essential for a programmatic study of many cases. As we shall see, these involve restricting the functional dependence of the single-particle wave functions, effectively decreasing the number of degrees of freedom of the system. Such constraints will reduce the dissipation and increase the time required to establish equilibrium. With this caveat in mind we shall now proceed to describe two simplifications commonly used. [See Davies, Devi, Koonin, and Strayer (84) and Negele (82) for a more complete discussion of these and other methods.]

One procedure reduces the dimensionality to $2 + 1$ dimensions by assuming axial symmetry. In the "clutching" model [Koonin, Davies, et al. (77)], the single-particle wave functions are taken to be

$$\psi_\mu(\mathbf{r}) = \chi_\mu(r, z) e^{im_\mu \phi} \quad (8.30)$$

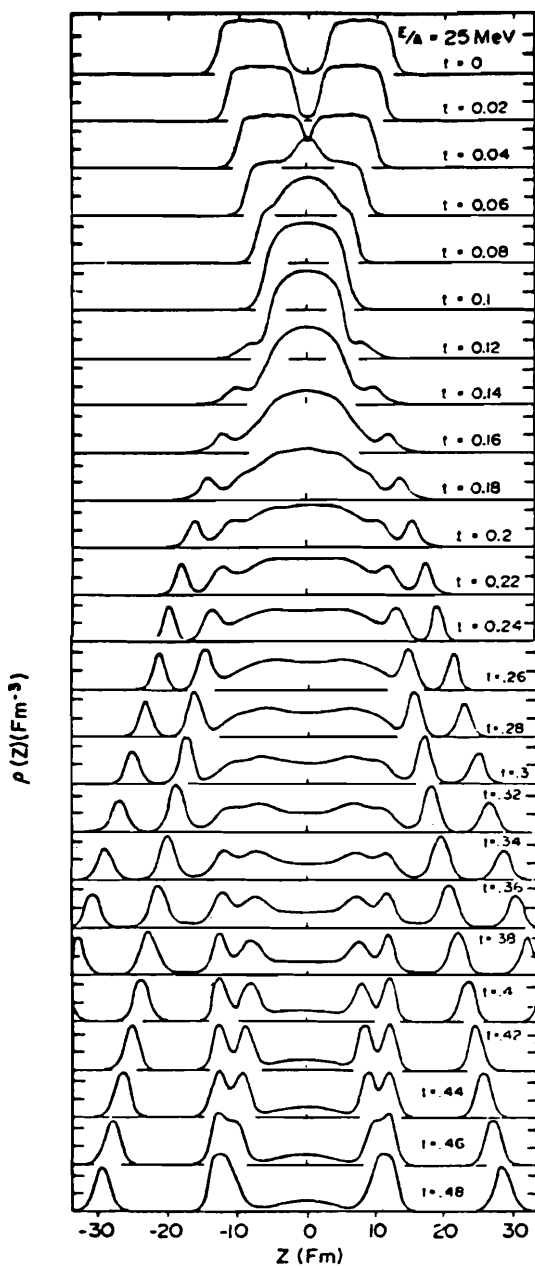


FIG. 8.3. Density profiles as a function of time for center-of-mass energy $E/A = 25 \text{ MeV}$. [From Negele (78).]

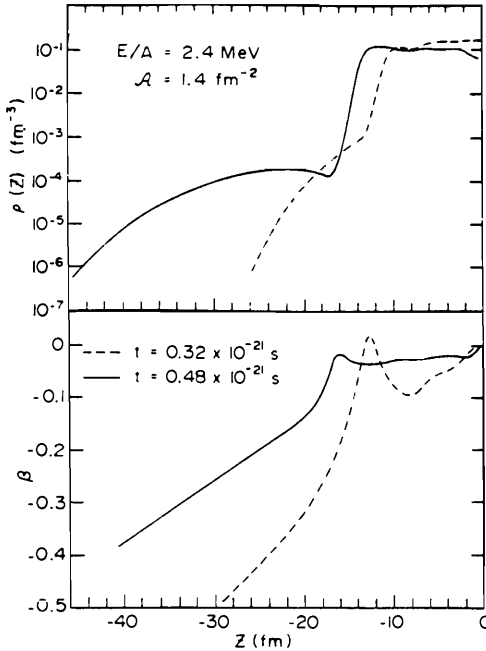


FIG. 8.4. Density profiles and velocity distributions for separating slabs showing particle emission. Only the left-hand plane is shown for this symmetric collision. The velocity is specified by $\beta = v/c$. [From Negele (82).]

In this equation cylindrical coordinates are used, the symmetry axis is along z , and $\hbar m_\mu$ is the angular momentum around the symmetry axis. The single-particle time-dependent equation for ψ_μ now reduces to an equation for χ_μ . The wave functions ψ_μ are regarded as intrinsic wave functions of a rotator as in the Bohr–Mottelson–Nilsson mode. One must add to the Hamiltonian of (8.1) the rotational energy in the form $L^2/2\mathcal{I}(\rho)$, where L is the initial angular momentum, a constant of the motion, and $\mathcal{I}(\rho)$ is the moment of inertia. The rotation is about an axis perpendicular to the reaction plane. The moment of inertia is taken to be that of two point masses a distance R apart when the colliding nuclei are not overlapping:

$$\mathcal{I}_{\text{point}} = m \frac{A_1 A_2}{A_1 + A_2} R^2$$

When the nuclei overlap (taken to be when the overlap density is one-half the saturation density), the rigid moment of inertia is used, that is,

$$\mathcal{I}_{\text{rigid}} = 2\pi \int \int dr dz (z^2 + r^2) \rho(r, z)$$

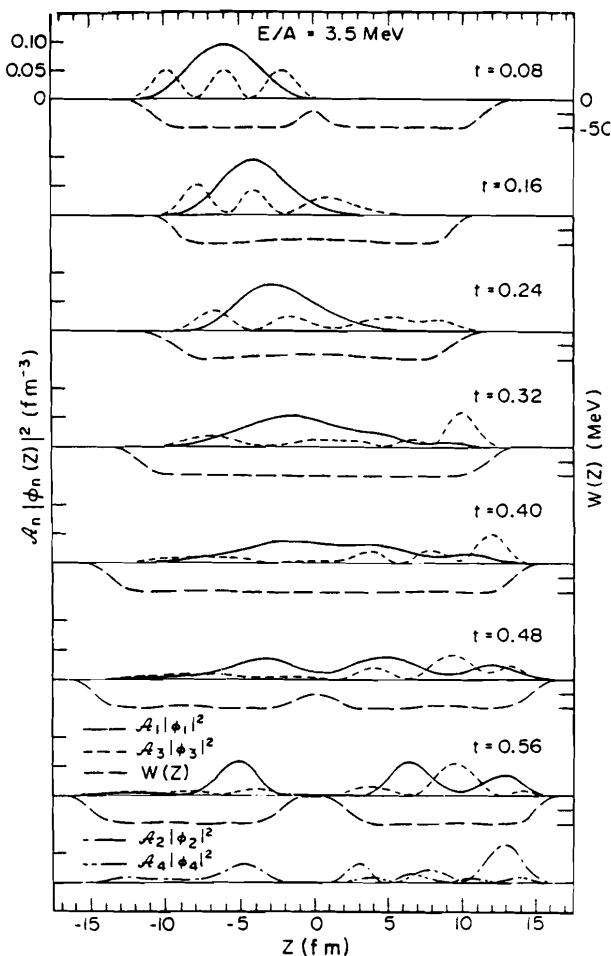


FIG. 8.5. Contributions of individual single-particle wave functions for the collision shown in Fig. 8.2. In the upper graphs, the mean field is denoted by the long-dashed line, with the scale shown to the right. The contributions to the density of the lowest orbital and third orbital originating in the left slab are indicated by the solid and short-dashed lines, respectively. The bottom graph displays the contributions of the second and fourth orbitals at the final time. [From Negele (82).]

In a second procedure referred to as the “2D frozen approximation” [Devi and Strayer (78), Koonin, Flanders, et al. (78)], it is assumed that ψ_μ can be written

$$\psi_\mu(\mathbf{r}, t) = \varphi_\mu(x, y, t)\chi_\mu(z) \quad (8.31)$$

This approximation is based on the presumption that most of the dynamical effects occur in the reaction plane, that is, that there is little change in the z

dependence of ψ_μ with time. This *ansatz* is borne out by the few three-dimensional calculations that have been performed. The function χ_μ is chosen at $t = 0$ to be a harmonic oscillator wave function whose scale is chosen so as to minimize the Hartree-Fock energy for the separated nuclei. This model has an important advantage over the clutching model in that it permits the excitation of nonaxially symmetric modes, thereby permitting more possibilities for energy dissipation and a more rapid approach to fusion and equilibration.

A further approximation, the "filling approximation", is made with respect to open-shell nuclei whose Hartree-Fock states would show a high degeneracy. For these cases the expression for ρ (at $t = 0$) given by (8.10) is replaced by

$$\rho^{(0)} = \sum_{\mu} n_{\mu} \psi_{\nu}(\mathbf{r}, 0) \psi_{\nu}^*(\mathbf{r}', 0) \quad (8.32)$$

where n_{μ} are the fractional occupation probabilities. This quantity is adjusted so that the resultant mean field is spherically symmetric; that is, $n_{\mu} = 1$ for filled shells and equal to $m/2(2l + 1)$ for a shell of orbital angular momentum l containing m particles. Moreover, these probabilities are assumed to be time dependent.

The TDHF theory provides a microscopic understanding of the macroscopic parameters described in Sections 1 to 5. Good qualitative understanding or agreement is obtained for the most part. There are discrepancies. For example, the experimental values of the widths of the charge and mass distributions are very much larger than the TDHF values. Cross sections cannot be obtained, as that would involve calculating the matrix elements of a many-body operator. The TDHF method is accurate for the matrix elements of one-body operators. In view of the approximation made, more precise methods for evaluating their validity and in estimating the theoretical error on the TDHF calculations are needed. At the present time, tests are made by comparing the results obtained using, for example, the models described above with each other and/or with three-dimensional calculations for various cases, colliding nuclei, energy, and angular momentum.

We consider fusion first. A good example is shown in Fig. 8.6. More generally, a fusion event is defined as "one in which the coalesced one-body density survives through at least one rotation or several oscillations of its rms radius" [Davies, Devi, Koonin, and Strayer (84)]. The fusion cross section is defined by the equation

$$\sigma_{\text{CF}} = \frac{\pi}{\kappa^2} \sum_{l_m}^{l_M} (2l + 1) = \frac{\pi}{\kappa^2} [(l_M + 1)^2 - (l_m + 1)^2] \quad (8.33)$$

Note that this equation differs from (2.5) in that it leaves open the possibility that the orbital angular momenta from $l = 0$ to $l = l_m - 1$ do not contribute to the fusion cross section. For a given reaction, the values of l_M and l_m are determined by interpolating TDHF calculations for various values of l .

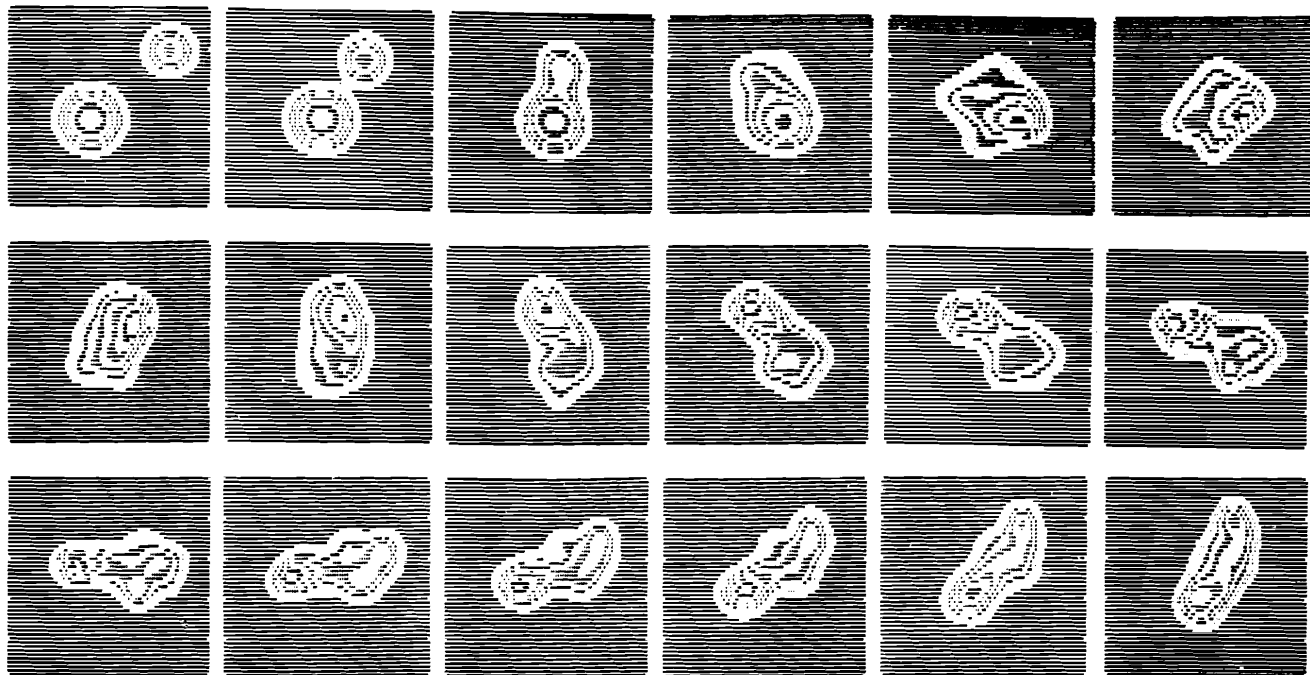


FIG. 8.6. Contour plots at sequential times of the density in the center-of-mass integrated over the normal to the reaction plane for $^{16}\text{O} + ^{40}\text{Ca}$ collision at a laboratory energy of 315 MeV. The initial angular momentum is $60 \hbar$. [From Negele (82).]

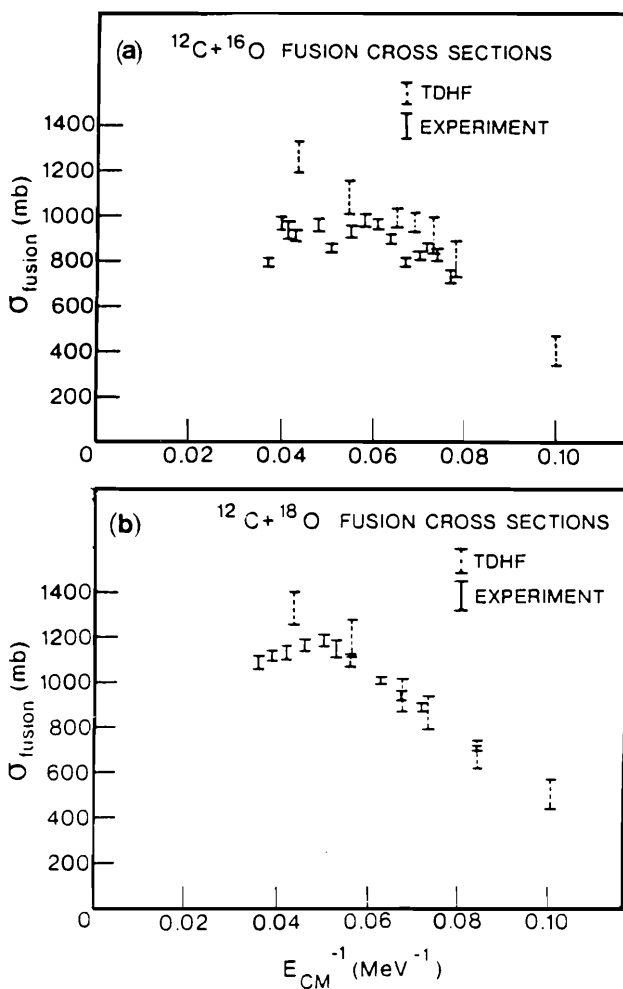


FIG. 8.7. Fusion excitation functions for (a) $^{12}\text{C} + ^{16}\text{O}$ and (b) $^{12}\text{C} + ^{18}\text{O}$ collisions are compared with the experimental data. [From Krieger and Davies (79).]

TABLE 8.2

System	$(l_M)_{\text{max}}$	
	TDHF	Liquid Drop
$^{16}\text{O} + ^{16}\text{O}$	31	32
$^{16}\text{O} + ^{27}\text{Al}$	45	43
$^{16}\text{O} + ^{24}\text{Mg}$	42	42
$^{16}\text{O} + ^{40}\text{Ca}$	62	58
$^{28}\text{Si} + ^{28}\text{Si}$	50	58
$^{40}\text{Ca} + ^{40}\text{Ca}$	≥ 60	67
$^{16}\text{O} + ^{93}\text{Nb}$	≥ 77	86

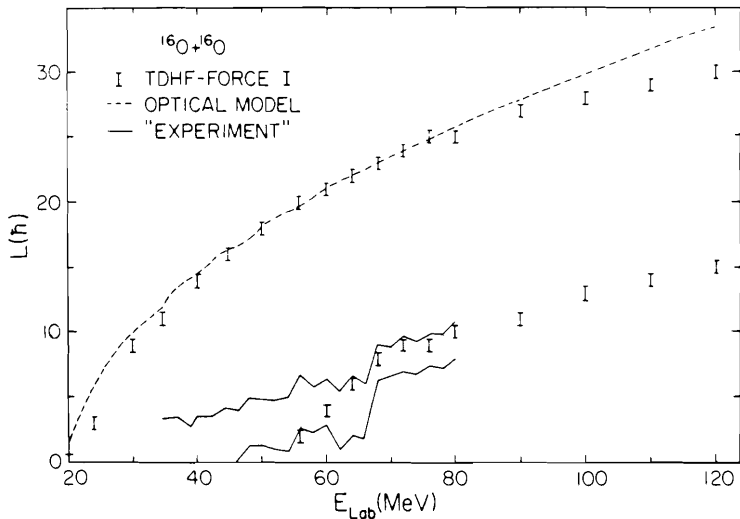


FIG. 8.8. Angular momentum limits to fusion for $^{16}\text{O} + ^{16}\text{O}$ collisions. Also shown in the upper angular momentum limit extracted from the optical model total reaction cross section and the "experimental" lower limit. [From Bonche et al. (78).]

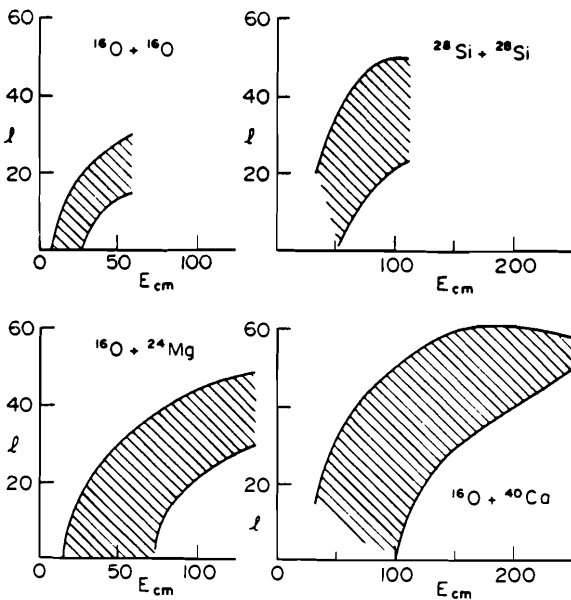


FIG. 8.9. Fusion regions, indicated by shaded areas, specifying the ranges of initial angular momentum l in units of \hbar and center-of-mass energy, E_{cm} , in MeV for which the TDHF initial value problem leads to a final state interpreted as a fused compound system. [From Negele (82).]

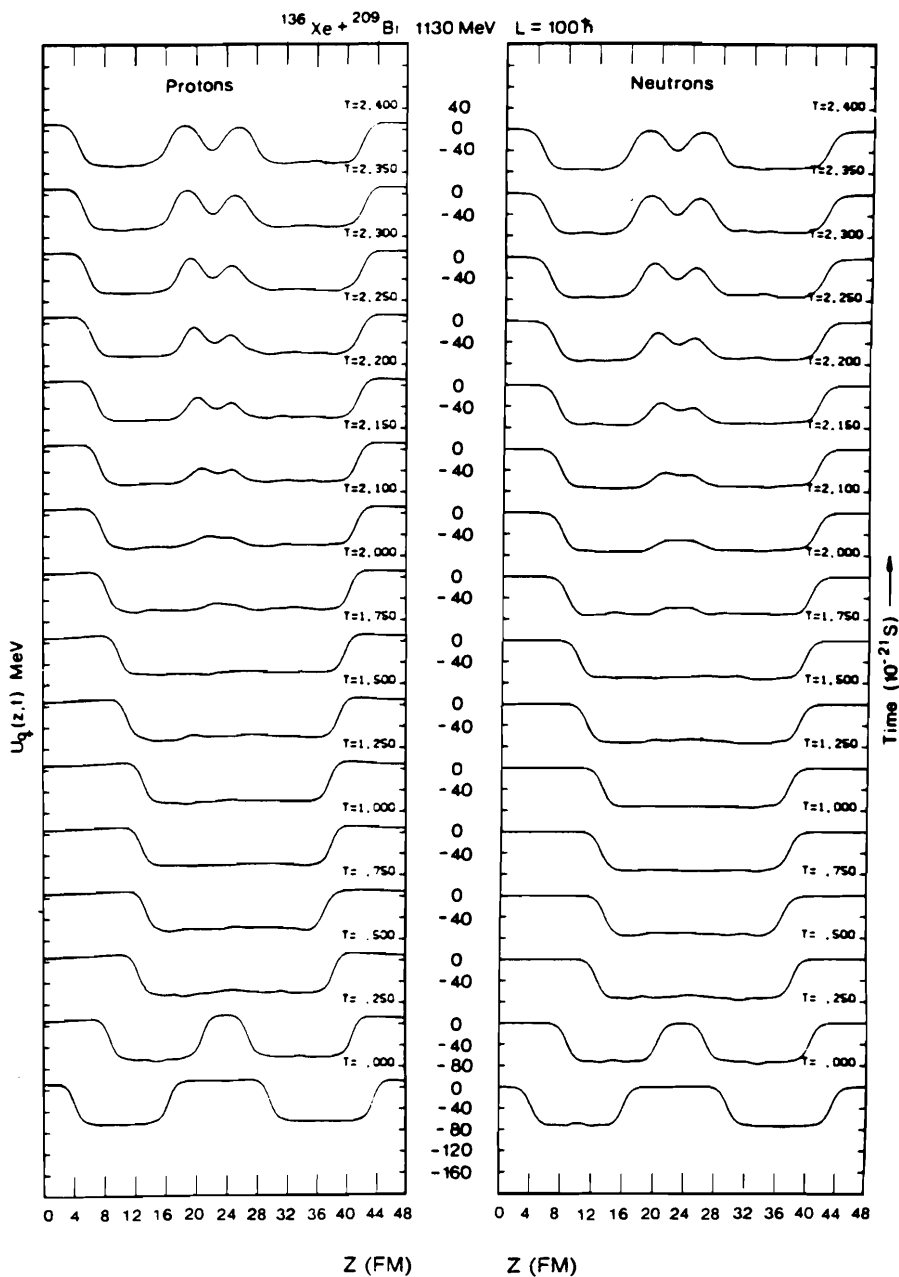


FIG. 8.10. Time evolution of the proton and neutron Hartree-Fock potentials along the symmetry axis for $^{136}\text{Xe} + ^{209}\text{Bi}$ at $E_{\text{lab}} = 1130$ MeV and $l = 100$. [From Dhar, Nelson, Davies, and Koonin (81).]

An example of the agreement of experiment with theory is illustrated in Fig. 8.7. One notes the linear dependence on $1/E$ in agreement with (2.7), permitting a determination of the macroscopic parameters R_B and V_B of that equation. This is shown in more detail in Fig. 8.8, where the value of l_M using (2.6) is plotted against the TDHF results. In Table 8.2 we compare the maximum value of l_M as a function of energy beyond which fusion does not occur (as discussed in Section 2, the compound nucleus cannot sustain higher values of l_M) with the values obtained from the liquid-drop model [Cohen, Plasil and Swiatecki (74)].

One of the surprising results obtained in TDHF calculations is the existence of a minimum value of l, l_m of (8.33) which is greater than zero. This is referred to as the *angular momentum window*. This is illustrated in Fig. 8.9.

We turn next to deep inelastic collisions. We restrict the discussion to heavy nuclei, for in those cases the collision is dominated by the deep inelastic process, as fusion is highly improbable. Consider the collision of ^{136}Xe with ^{209}Bi at a laboratory energy of 1130 MeV (about 8.3 MeV/A). The time evolution of the TDHF proton and neutron potentials along the symmetry axis for $l=100$ is shown in Fig. 8.10. We see the merging of the two potential wells to form a

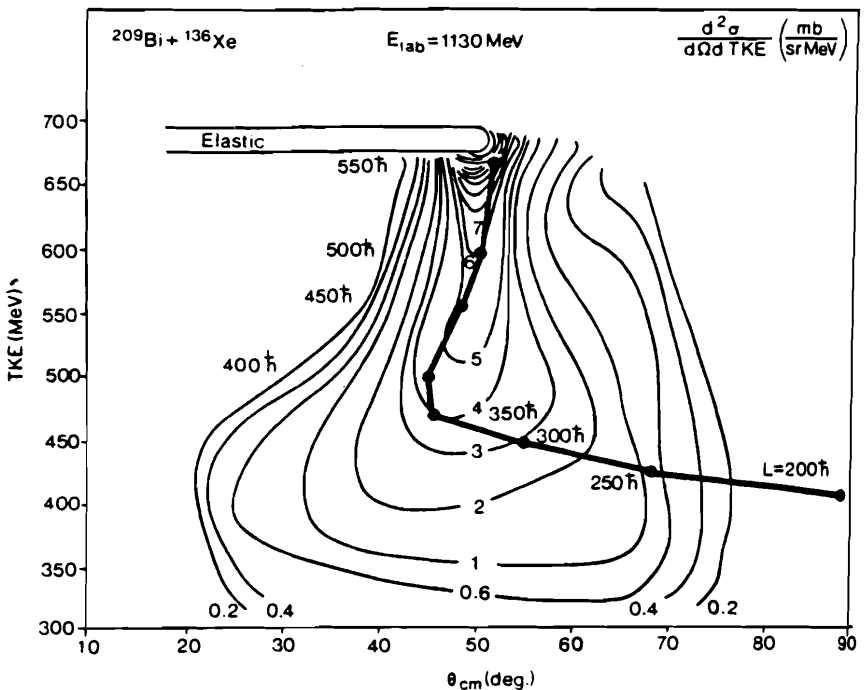


FIG. 8.11. Comparison of calculated points with the experimental Wilczyński plot for $^{136}\text{Xe} + ^{209}\text{Bi}$ at $E_{lab} = 1130 \text{ MeV}$. The calculated points for various initial orbital angular momenta are connected by a full line. [From Dhar, Nelson, Davies, and Koonin (81).]

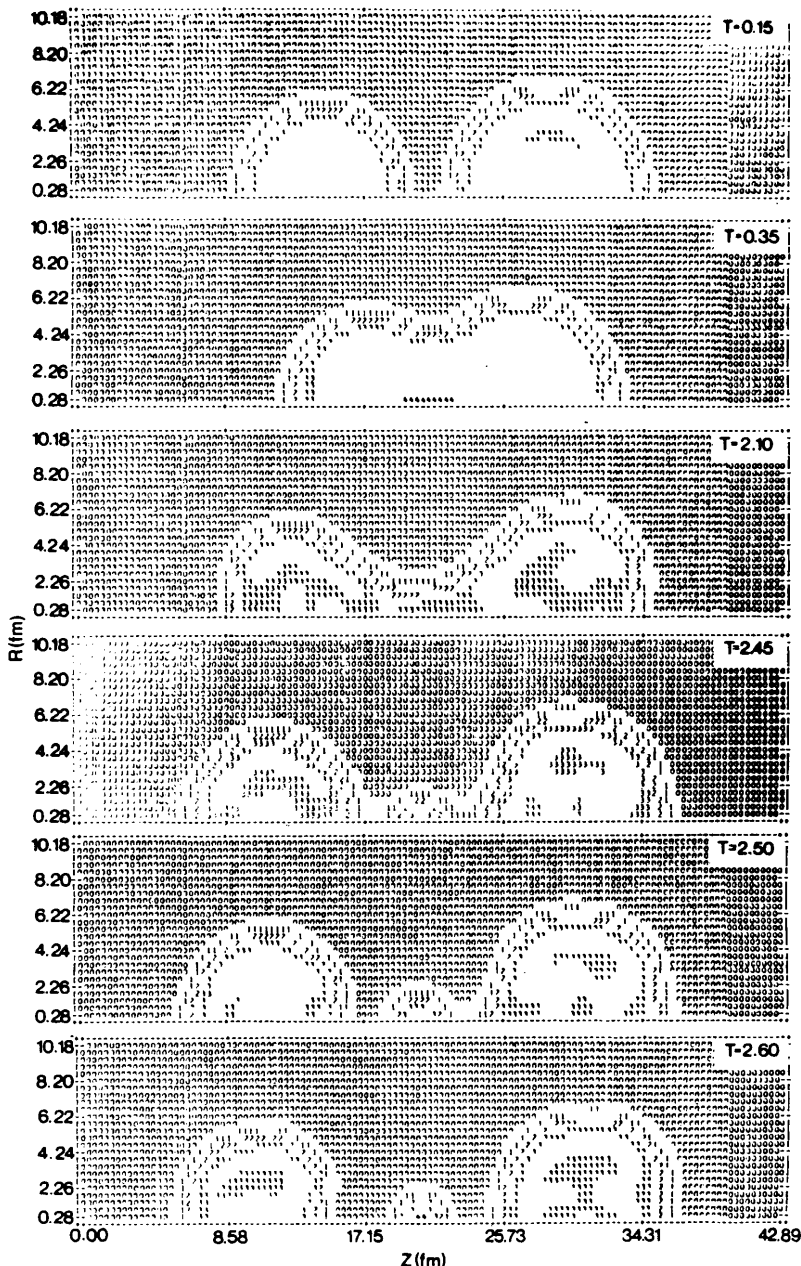


FIG. 8.12. Equidensity contours at various times during a $^{86}\text{Kr} + ^{139}\text{La}$ collision at $E_{\text{lab}} = 710$ MeV and $l = 100$. The symmetry axis lies along the line joining the mass centers of the projectile and target. All times are in units of 10^{-21} s. [From Davies, Sandhya Devi, and Strayer (79).]

common well and then the reformation of the original two wells plus an additional well. More about this later. A popular way of summarizing the experimental data is the Wilczyński plot, in which the cross section contours are plotted in the total kinetic energy, and θ_{cm} plane. Such a plot is shown in Fig. 8.11. The TDHF calculations are given by the connected points, which plot the total kinetic energy versus the scattering angle. Each impact parameter (indicated by l) in a TDHF calculation yields a point on this line. It is presumed that the line will follow the ridge of the cross section contours. We see the characteristic very rapid drop on kinetic energy followed by a slower rate of decrease. We also observe that the TDHF energy loss at “small” l is not as large as the experimental results require. This is a common failure of the TDHF calculation (and the charge and mass distribution mentioned above). However, apart from this problem, the TDHF results are in semiquantitative agreement with experiment. One feature should be noted—namely, that there is a large interchange of target and projectile nucleons. One may also use the calculations to compare with the macroscopic phenomenology of Nix and Sierk discussed in Section 2. These authors introduce the coordinates R , measuring the separation of the ions, and σ , the elongation.

The TDHF calculation predicts the early emission of neutrons in the process. This occurs because the projectile nucleon energy in the common well (see Fig. 8.10) exceeds the Fermi plus binding energy. A more unexpected phenomenon is the production of an α -particle at scission. This is illustrated in Fig. 8.12. Returning to Fig. 8.10, we note the formation of three wells at 2.4×10^{-21} s. The well in the center governs the evolution of the α -particle.

The TDHF method thus provides good insight into the dynamics of the low-energy heavy-ions collisions. Its major failure is that it does not provide a method for the calculation of cross sections.
